Optimal Control with MCTDH and CRAB

Masterarbeit

Christian Ziemann
Universität Hamburg
Fachbereich Physik

Erstgutachter: Prof. Dr. R. J. Dwayne Miller (MPI für Struktur und Dynamik der Materie)
Zweitgutachter: Prof. Dr. Peter Schmelcher (Institut für Laserphysik)

Abstract

The multi-configurational time-dependent Hartree method (MCTDH) has been established as a powerful tool for the simulation of multi-dimensional systems, especially in the realm of molecular physics. It has also been used for optimal control of molecular systems, mostly employing the well-known Rabitz and the Krotov optimization schemes. In this thesis, the MCTDH software is combined with the relatively new optimization method CRAB (chopped random basis). State selective excitation of different one-dimensional systems is performed with optimized laser pulses. The main objective was vibrational excitation of a Morse oscillator with a light field expanded in a finite Fourier basis for CRAB optimization. In this case CRAB performed at least as good as the established Krotov scheme, with target populations near 100% despite smaller computational effort.

Zusammenfassung

Das MCTDH-Verfahren hat sich als mächtiges Werkzeug zur Simulation mehrdimensionaler Systeme bewährt, insbesondere im Bereich der Molekülphysik. Es wurde auch bereits für gezielte Kontrolle molekularer Systeme eingesetzt, hauptsächlich unter Verwendung der bekannten Optimierungsschemata nach Krotov und Rabitz. In dieser Arbeit wird MCTDH mit dem vergleichsweise neuen Optimierungsverfahren CRAB kombiniert. Eigenzustände in verschiedenen eindimensionalen Systeme werden selektiv mit optimierten Laserpulsen angeregt. Hauptaugenmerk liegt auf einem Morseoszillator, dessen Vibrationszustände gezielt angeregt werden. Das dafür genutzte Feld wird in einer endlichen Fourierbasis dargestellt und mit Hilfe von CRAB optimiert. CRAB erweist sich für diese Anwendung als mindestens gleichwertig zu dem etablierten Krotov-Schema, indem die Zielzustände trotz geringem Rechenaufwand zu fast 100% besetzt werden.

Contents

1 Introduction

The past two decades have seen impressive progress in the field of quantum control theory. Its main goal may be summarized as the design of optimal external fields to guide a quantum system into a desired state. In the field of quantum chemistry, this usually means finding specifically shaped light pulses to steer a molecular system into a target state. The ultimate goal of this would be laser control of chemical reactions. This can be done by experimental methods, but also theoretical simulations have shown to be useful to understand the underlying dynamics [4].

These theoretical calculations require two main ingredients: The response of the system in question to an external field must be modelled accurately (i.e. its wavefunction must be propagated in time), which can then be used by an iterative algorithm to optimize said field.

Molecular systems are inherently difficult to simulate numerically due to the high number of degrees of freedom (DOFs). Even after employing simplifications such as the Born-Oppenheimer approximation, the scaling behaviour of multi-dimensional systems discourages exact calculations. A number of numerical methods exist, though, each offering a trade off between accuracy and numerical effort. In this work the Multi Configurational Time Dependent Hartree method (MCTDH) [19] will be used, which has been shown to simulate quantum systems of high dimensionality very efficiently and with good accuracy[3].

With such a tool for efficient wavefunction propagation at hand, it has to be embedded into an optimal control algorithm such as the well-probed Krotov scheme, which has already been implemented with MCTDH. This thesis will pursue a different scheme, namely the Chopped Random Basis (CRAB) method. CRAB [5] has only recently been proposed as a versatile tool for a wide range of optimal control problems.

Hence this work will attempt to perform optimal control with the CRAB algorithm, using MCTDH to calculate the system's behaviour in the external field. The systems under study are a one-dimensional Morse oscillator as a simple model for a generic diatomic molecule and the LiCs diatomic. As control targets, various vibrational states are selectively excited with laser pulses.

Chapter 2 supplies the necessary physical background for these studies. This mostly includes an introduction into the relevant parts of molecular physics, but also a primer on quantum control theory. Chapter 3 follows up with a detailed description of the calculational methods central to this work, i.e. MCTDH and CRAB. It also includes a description of the non-linear optimization algorithms which are used later. Chapter 4 then describes the performed calculations. While some of these are mere test runs and may be omitted by a reader familiar with MCTDH, this thesis

proceeds to increasingly relevant systems via the Morse oscillator to the LiCs molecule, where experimental potential data are used. The second half of chapter 4 includes optimal control runs with CRAB. Chapter 5 describes and discusses the results of these simulations, while section 6 gives a conclusive summary.

2 Physics of Molecules

This chapter will give a short overview of the molecular physics which are subject of this work. Exact analytical solutions are generally impossible for molecular systems, and even numerical approaches often run into difficulties due to the high dimensionality. Therefore it is common to employ some approximations, the most common being the Born-Oppenheimer approximation [8]. Section 2.1 describes this essential tool of molecular physics. It allows to describe electronic and nuclear motions seperately, giving rise to electronic and vib-rotational eigenstates. Section 2.2 analyzes these eigenstates for the important special case of diatomic molecules. Having understood undisturbed molecules sufficiently well, it is time to study the interaction of molecules with external fields in section 2.3. Section 2.4 then discusses techniques to optimize such fields for a specific purpose, which is known as Quantum Optimal Control Theory (QOCT). Structure and contents of this chapter follow the relevant parts of [8] and [11] closely.

2.1 Born-Oppenheimer approximation

As a non-relativistic[1] quantum system, a molecule obeys the Time-Dependent Schrödinger Equation (TDSE) [8]

$$i\hbar\frac{\partial}{\partial t}\Psi(t) = \hat{H}\Psi(t) \tag{2.1}$$

Here $\Psi(t)$ denotes the molecule's wavefunction and $\hat{H}$ is the Hamiltonian operator. Given $\hat{H}$ and an initial value $\Psi(t_0)$, the system's state is uniquely determined for all times. Assuming a molecule with $N_n \geq 2$ nuclei and a total of $N_e \geq 1$ electrons, the Hamiltonian can be specified and split into parts:

$$\begin{aligned}\hat{H} &= \hat{T}_n + \hat{T}_e + \hat{V}_{n-n} + \hat{V}_{e-e} + \hat{V}_{e-n} \\ &= -\hbar^2 \sum_{i=1}^{N_n} \frac{\nabla_i^2}{2M_i} - \hbar^2 \sum_{k=1}^{N_e} \frac{\nabla_k^2}{2m} \\ &+ \frac{e^2}{4\pi\varepsilon_0} \sum_{i<j}^{N_n} \frac{Z_i Z_j}{|\mathbf{R}_i - \mathbf{R}_j|} + \frac{e^2}{4\pi\varepsilon_0} \sum_{k<l}^{N_e} \frac{1}{|\mathbf{r}_k - \mathbf{r}_l|} - \frac{e^2}{4\pi\varepsilon_0} \sum_{i=1}^{N_n} \sum_{k=1}^{N_e} \frac{Z_i}{|\mathbf{R}_i - \mathbf{r}_k|}\end{aligned} \tag{2.2}$$

[1] Throughout this work, relativistic effects will be neglected, which is common in computational chemistry with light elements [12].

The five terms correspond to the nuclear and electronic kinetic energy, the nuclear-nuclear, electron-electron and nuclear-electron potential energy, respectively. M_i is the mass of the ith nucleus, m the electron mass. ∇_i is a gradient operator which only acts on the coordinates of particle i, which are denoted $\mathbf{R}_i$ for nuclei and $\mathbf{r}_i$ for electrons [8].

Before proceeding, the notation can be simplified by introducing *atomic units*. In atomic units (a.u.) $e = \hbar = m = \frac{1}{4\pi\varepsilon_0} = 1$, so most constants can be dropped from equation (2.2). The natural unit of length in a.u. is the *Bohr length* defined by $a_0 = \frac{4\pi\varepsilon_0}{me^2} \approx 0.053\,\mathrm{nm} = 0.53\ \text{Å}$ (the radius of ground state hydrogen in the Bohr model), while energies are now measured in multiples of a *Hartree*: $1\,\mathrm{Ha} = \frac{\hbar^2}{ma_0^2} \approx 27.2\,\mathrm{eV} \approx 2.1947 \cdot 10^5\,\mathrm{cm}^{-1}$ (twice the binding energy of a hydrogen atom) [11]. All quantities in this work are given in atomic units unless explicitly noted otherwise.

For a time-independent Hamiltonian such as (2.2), the TDSE can be solved by finding the system's eigenstates Ψ_n and expanding the wavefunction in this basis

$$\Psi(t) = \sum_n c_n e^{-iE_n/t}\Psi_n, \tag{2.3}$$

where the E_n are the energy eigenvalues and fulfil the time-independent Schrödinger equation

$$(\hat{H} - E_n)\Psi_n = 0. \tag{2.4}$$

There are no analytical solutions of (2.4) for even the simplest molecules [8], but a number of approximations may be made to simplify the problem. The *Born-Oppenheimer* (BO) approximation starts from the assumption that the electrons move much faster than the nuclei, so from an electron's point of view, the nuclear positions $\mathbf{R}$ are almost static. The electronic wavefunction adapts to any nuclear configuration adiabatically, making the nuclear motion negligible. Hence when calculating the electron distribution, one may consider $\mathbf{R}$ to be constant for any given time. In other words, the nuclear kinetic energy T_n is much smaller than the electronic energy $T_e + V_{e-e} + V_{e-n}$, allowing for a perturbational approach to (2.4). The Hamiltonian may be split into an unperturbed part $\hat{H}_0 = \hat{T}_e + \hat{V}$ and the perturbation $\hat{H}_1 = \hat{T}_n$. This leads to a *clamped nuclei* Schrödinger equation:

$$\hat{H}_0\phi^{el}(\mathbf{r};\mathbf{R}) = E_n^0(\mathbf{R})\phi_n^{el}(\mathbf{r};\mathbf{R}) \tag{2.5}$$

The semicolon[2] indicates that the electronic wavefunction $\phi_n^{el}(\mathbf{r};\mathbf{R})$ only takes the electron positions $\mathbf{r}$ as independent variable, whereas $\mathbf{R}$ is just a parameter [18]. Note that $\hat{H}_0$ only acts on $\mathbf{r}$, too. Now assume (2.5) has been solved (either numerically or, in very simple cases as in H_2^+, analytically) for an arbitrary fixed $\mathbf{R}$ such that the electronic eigenfunctions $\phi_n^{el}(\mathbf{r};\mathbf{R})$ are known. Without loss of generality, these eigenfunctions are orthonormal and can be used to expand the

[2] Some textbooks use the notation $\phi^{el}(\mathbf{R};\mathbf{r})$, $\phi^{el}(\mathbf{r}|\mathbf{R})$ or $\phi^{el}(\mathbf{r},\mathbf{R})$ instead.

full molecular wavefunction as

$$\Psi(\mathbf{r}, \mathbf{R}) = \sum_n \chi_n(\mathbf{R}) \phi_n^{el}(\mathbf{r}; \mathbf{R}) \tag{2.6}$$

It is worth remembering that Ψ is a function of both the electronic and the nuclear coordinates $\mathbf{r}$ and $\mathbf{R}$ (hence the comma), and the nuclear wavefunctions χ_n depend only on $\mathbf{R}$, of course. Inserting equation (2.6) into the molecular Schrödinger equation (2.4) eventually leads to two coupled systems of equations for $\phi(\mathbf{r}; \mathbf{R}$ and $\chi(\mathbf{R})$:

$$\hat{H}_0 \phi = E^0 \phi \tag{2.7}$$

$$\hat{H}_1 \chi_n + \sum_m (\hat{c}_{nm} \chi_m) = (E - E_n^0) \chi_n \tag{2.8}$$

with the coupling coefficients

$$\hat{c}_{nm} := \int \phi_n^* \hat{H}_1 \phi_m \mathrm{d}\mathbf{r} - \frac{1}{2} \sum_k \left(\int \phi_n^* \frac{1}{M_k} \frac{\partial}{\partial R_k} \phi_m \mathrm{d}\mathbf{r} \right) \frac{\partial}{\partial R_k} \tag{2.9}$$

Up to this point no approximations have been made. The BO approximation now states that all $\hat{c}_{nm} = 0$, completely uncoupling equation (2.7) from (2.8). In other words, the molecular wavefunction is assumed to factorize simply into

$$\Psi(\mathbf{r}, \mathbf{R}) = \chi(\mathbf{R}) \cdot \phi^{el}(\mathbf{r}; \mathbf{R}) \tag{2.10}$$

This approximation can be justified by the fact that the coupling coefficients are very small compared to the $\hat{H}_1 + E_n^0$ term in equation (2.8) [8].

Using the BO approximation, the problem of molecular dynamics can be solved in two steps: First solve the electronic Schrödinger equation (2.5) assuming clamped nuclei for any position $\mathbf{R}$. In practice, this can usually only be done for a finite number of points, requiring interpolation for intermediate values. This gives the electronic energy levels $E_n^0(\mathbf{R})$ which depend parametrically on the nuclear positions. These energies can then be inserted into the nuclear Schrödinger equation, acting as a potential energy there. Now the reduced version of equation (2.8), $(\hat{T}_n + E_n^0)\chi_n = E\chi_n$ can be solved for the nuclear wavefunctions, yielding the solutions $\chi_{n,i}(\mathbf{R})$. While n indexes the electronic energy levels, i counts the nuclear (i.e. vibrational and rotational) energy levels for a fixed electronic state.

Since $E_n^0(\mathbf{R})$ can be interpreted as a potential in the nuclear Schrödinger equation, it is usually called the *Potential Energy Surface* (PES) of state n and denoted by $U(\mathbf{R})$. It includes all potential terms from equation (2.2) and the averaged kinetic energy of the electrons. In the classical picture, the nuclei may be seen as masses moving on such a (typically multi-dimensional) PES.

A few words on the physical interpretation of the BO approximation: As the electrons move much faster than the nuclei, they adapt to any change of the nuclear position almost instanta-

neously. This serves to justify both the clamped nuclei approach when calculating the electronic wavefunction and the inclusion of the averaged electronic energy into the PES.

According to the *adiabatic theorem*, the electronic wavefunction remains in the corresponding eigenstate ϕ_n during such a gradual change of $\hat{H}_1$ without coupling to other eigenstates ϕ_m [11]. In other words, the molecule will always remain on the same PES.

However, the adiabatic theorem, and with it the BO approximation, breaks down at crossings of PESs. More on this in section 2.5.

2.2 Eigenstates of diatomic molecules

Having separated the electronic from the nuclear wavefunction, both problems can be solved independently. This section will at first turn towards the former, describing the electronic states of molecules. Then vibrational and rotational eigenstates are introduced. This also means climbing down the energy scale from visible and UV light (exciting electronic transitions) over IR light (typical vibrational energies) down to the microwave regime (for rotational energies) [18].

The discussion will be restricted to diatomic molecules for two reasons: On one hand, only diatomics are subject of the studies in chapter 4. On the other hand, the energy structure of diatomics allows for a rather systematic and instructive description building upon many concepts known from atomic physics.

Although there is always coupling between the electronic, vibrational and rotational modes of a molecule, most of these interactions are neglected in this work. Unless otherwise noted, a non-rotating molecule in the electronic ground state can be assumed. For the sake of completeness, the respective eigenstates will still be explained now.

Electronic states

Assuming a static frame of nuclear positions $\mathbf{R}$, the electronic equation (2.5) can be solved. Again, analytic solutions are generally not feasible (the H_2^+ ion being a notable exception), but further simplifications are possible. An important concept are *molecular orbitals* (MOs), which transfer the notion of electronic orbitals from atomic to molecular physics. Single electrons are assigned to specific states characterized by a set of quantum numbers, while the interaction with the other electrons is either ignored or accounted for by mean fields. The total electronic wavefunction then becomes a Slater determinant, i.e. an anti-symmetrized product of single-electron wavefunctions.

As in the atomic case, the eigenstates are conveniently classified by a set of quantum numbers. *Good* quantum numbers are eigenvalues of operators which commute with the molecular Hamiltonian [18]. For atoms, these include $\hat{L}^2$ (the total orbital angular momentum of the electrons squared) and $\hat{L}_z$ (the z component of the orbital angular momentum). When moving from atoms to molecules, radial symmetry is lost, so total angular momentum is no longer conserved

(in other words, $\hat{L}^2$ and $\hat{H}$ do not commute). The potential is axially symmetric, though, so $\hat{L}_z$ still commutes with $\hat{H}$.

Its eigenvalues M are integers[3], and molecular states are classified by the value $\Lambda = |M| \in 0, 1, 2, \ldots$. Capital Greek letters are used to denote different values, with $\Sigma, \Pi, \Delta, \Phi, \ldots$ signifying $\Lambda = 0, 1, 2, 3, \ldots$, respectively. States with non-zero Λ values are twofold degenerate, as $M = n$ and $M = -n$ correspond to the same energy.

The spin operators $\hat{S}_z$ and $\hat{S}^2$ still commute with the Hamiltonian, preserving S as a good quantum number.

Each pair (Λ, S) defines an electronic *term*, a set of degenerate electronic states. This degeneracy is expressed by adding the *multiplicity* $2S + 1$ as a superscript to the Greek symbol. For example ${}^1\Sigma$ denotes a *singlet* state with $\Lambda = S = 0$, while the *triplet* ${}^3\Sigma$ is degenerate due to $S = 1$ (which permits the orientations $S_z = 0, \pm 1$).

In molecules with point symmetry[4], an additional subscript *g* or *u* denotes whether the wavefunction is *gerade* or *ungerade*, i.e. whether it is invariant under inversion at the centre or changes its sign. And similarly, a Σ wavefunction may or may not change its sign upon reflection in a plane containing the molecular axis and is accordingly dressed with a plus or minus sign.

A full term symbol may thus be as simple as ${}^3\Delta$ for a molecule with $\Lambda = 2, S = 1$ or be somewhat complex like ${}^1\Sigma_g^+$ for $\Lambda = 0, S = 0$ with a wavefunction which does not change sign under inversion or reflection.

All terms can now be ordered by total energy. The ground term is denoted by the letter X, while higher-energy terms are ordered alphabetically as A,B,...

Here capital letters are used for terms with the same multiplicity, while terms with a different multiplicity usually receive small letters (a,b,...) [18].

Vibrational states

The focus of this work lies on vibrational states, as these are crucial for laser induced dissociation of molecules and the dynamics of many chemical reactions.

The solution of the electronic problem usually leads to the multi-dimensional PES $U(\mathbf{R})$ of a particular electronic state. In the diatomic case however, $U(R)$ only depends on one variable, the internuclear distance R. This allows to separate off the angular-dependent parts of the nuclear wavefunction $\chi(\mathbf{R}) = \psi(R)L(\theta, \varphi)$, reducing the problem to the one-dimensional Schrödinger equation. After switching to the centre-of-mass system and introducing the reduced mass $M_r = M_1 M_2/(M_1 + M_2)$, the nuclear wavefunction obeys [8]:

$$\left(-\frac{1}{2M_r}\frac{\partial^2}{\partial R^2} + U(R)\right)\psi(R) = E\psi(R) \tag{2.11}$$

[3]This holds in atomic units. In SI units, the eigenvalues are $M\hbar$.
[4]In the diatomic case, this includes only homonuclear molecules.

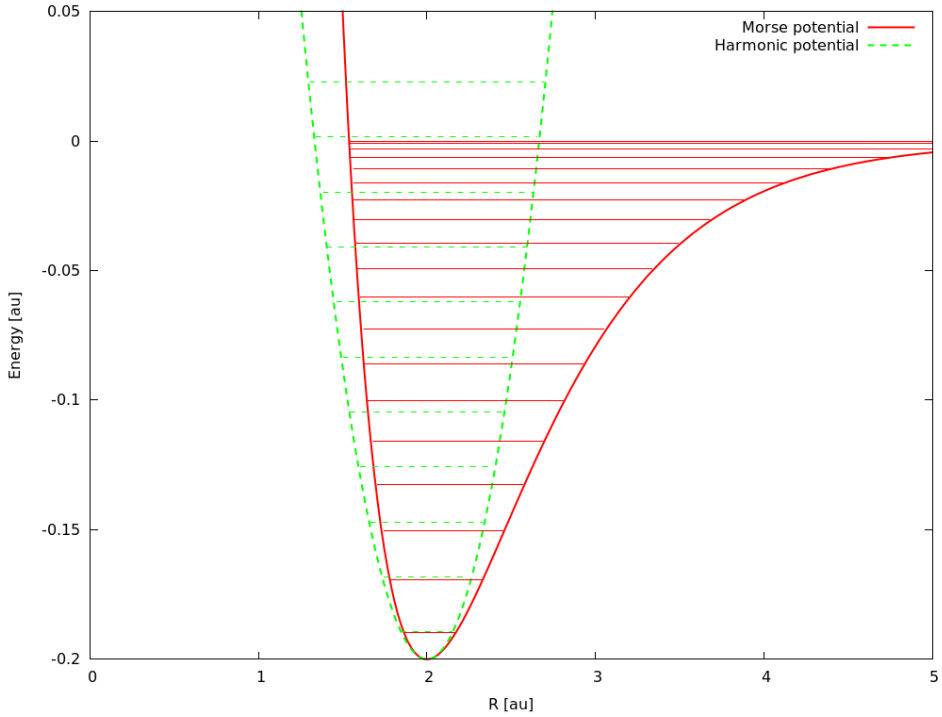

Figure 2.1: Comparison of a molecular potential and its quadratic approximation with respective energy levels. Red (solid) line: Morse potential with parameters $D = 0.2, \beta = 1.5, R_0 = 2.0$. Green (dashed) line: Harmonic approximation around R_0.

At least the electronic ground state provides a potential minimum at a distance R_0, so the existence of a stable ground state is guaranteed (otherwise no stable molecule can be formed). The equilibrium distance R_0 may range from $0.74\,\text{Å}$ for H_2 up to $52\,\text{Å}$ for the extremely unstable He_2 [7, 10]. Most diatomic molecules lie between one and a few Å in size. For small energies, the internuclear distance will oscillate around the equilibrium, resulting in a vibrating motion of the nuclei along the molecular axis.

Near the minimum, $U(R)$ can be expanded as a Taylor series:

$$U(R_0 + x) = U(R_0) + \frac{1}{2}U''(R_0) \cdot x^2 + \mathcal{O}(x^3) \tag{2.12}$$

In some molecules the $\mathcal{O}(x^3)$ term is negligible for the lowest energy states, so their spectrum resembles that of a harmonic oscillator. In particular, the lowest energy levels are almost equidistant. One example of an anharmonic potential is given by the Morse potential depicted in figure 2.1. It is defined by

$$U(R) = D \cdot \left(1 - e^{-\beta(R-R_0)}\right)^2 - D \tag{2.13}$$

and has been used to model the potential of diatomics for a long time [8]. D is the dissociation energy, R_0 is the equilibrium distance and β is the width parameter of the potential. Close to R_0, the quadratic approximation is quite accurate, and in the figure the first two energy levels

almost coincide with the harmonic energies. With increasing energy and displacement from equilibrium, the approximation breaks down. For large R, the Morse potential physical flattens and converges to zero[5]. The energetic distance between eigenstates decreases as dissociation is approached, but only a finite number of bound states is supported.

For small R, the Morse potential grows exponentially, effectively prohibiting the system from reaching $R = 0$. In physical molecules, the potential actually diverges at the origin, but for a qualitative description the Morse model is often sufficient. It has the great advantage of being analytically solvable. The eigenenergies are

$$E_n = -D + \omega\left(n + \frac{1}{2}\right) - \frac{\omega^2}{4D}\left(n + \frac{1}{2}\right) \tag{2.14}$$

where $\omega = \beta\sqrt{2D/M_r}$ is the frequency of the corresponding harmonic oscillator and the second term is the result of the anharmonicity of the potential. As in the harmonic oscillator, the vibrational quantum number n can take non-negative integer values, but here it has an upper limit [8].

Other, more realistic molecular potentials have a different anharmonicity term, but usually show comparable features: Convergence to zero for $R \to \infty$, increasing density of states near dissociation and divergent behaviour for $R \to 0$. Eigenfunctions resemble harmonic eigenfunctions for small n, but look more and more like plane waves (at least for large R, where the potential is almost zero) near dissociation.

As an example, the potential energy of the LiCs diatomic is shown in figure 2.2.

Rotational states

Apart from vibrations, molecules can perform *rotational* motions. A useful approximation is the *rigid rotor* model, i.e. the assumption of two masses with a fixed distance R rotating around the centre of mass. This is in agreement with the procedure of the last section, where the angular motion had been separated from the vibrational motion along the molecular axis.

The rigid rotor is a standard textbook exercise [8] with the energy levels

$$E_J = \frac{J(J+1)}{2M_r R^2} \tag{2.15}$$

where the rotational quantum number J can take the values $0, 1, 2, \ldots$. The eigenfunctions are the well-known *spherical harmonics* $Y_{JM}(\theta, \varphi)$. A diatomic molecule has axial symmetry, so only two possible axes of rotation exist, both perpendicular to the molecular axis.

In reality, the internuclear bond is not rigid, but widens under the influence of centrifugal force. As a result, the equilibrium distance increases with J, and with it the total energy (because

[5]The specific value is of course convention. It is common to assign negative energy values to bound states and define the zero of the energy scale to lie at $R = \infty$.

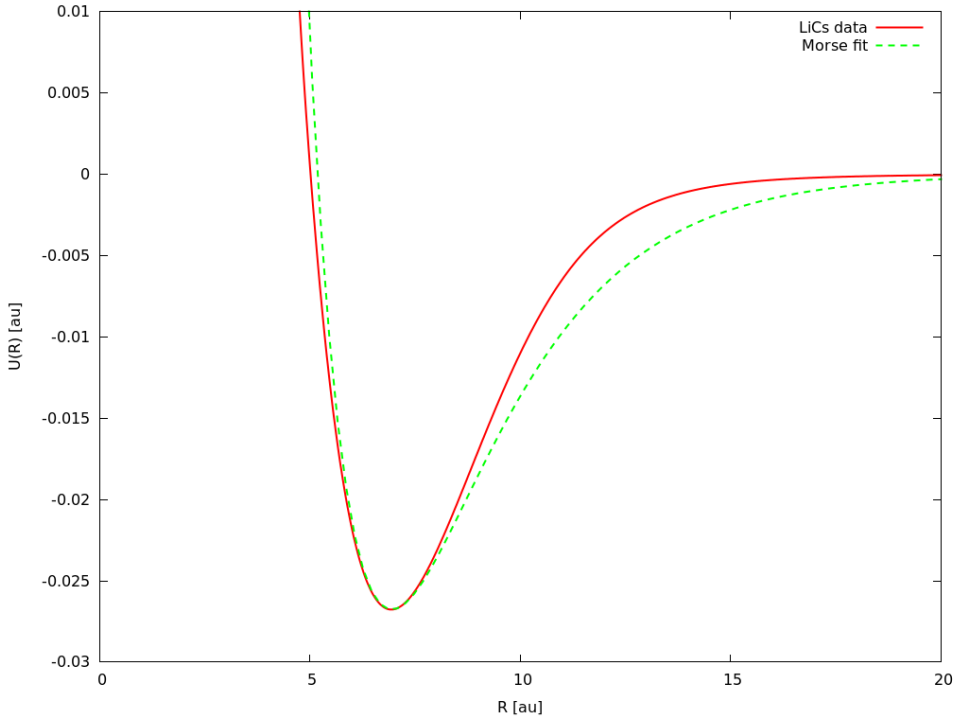

Figure 2.2: Comparison of LiCs potential energy curve (red, solid line) with fitted Morse potential (green, dashed line). Data from [24].

a larger nuclear distance amounts to an increase in potential energy). In terms of the angular momentum $|\mathbf{J}| = \sqrt{J(J+1)}$ and the non-rotating equilibrium distance R_0,

$$E_{\text{rot}} = \frac{|\mathbf{J}|^2}{2M_r R_0^2} - \frac{|\mathbf{J}|^4}{2kM_r^2 R_0^6} + \frac{|\mathbf{J}|^6}{2k^2 M_r^3 R_0^{10}} + \dots \tag{2.16}$$

Here $k = -\frac{\partial}{\partial R} U(R = R_0)$ is the spring constant of the potential energy curve. For a derivation and more detailed discussion, including the effects of the electron angular momentum (omitted here), see [8].

An important deviation from the rigid rotor is the coupling between rotational and vibrational degrees of freedom. As the vibrations are much faster (one or two orders of magnitude) than the rotations, many vibrations occur during one rotational period. The resulting change in R affects the rotational energy, so there is a constant transfer of energy between rotational and vibrational modes.

The rotational energy also gives correction terms to the potential energy $U(R)$, as it is proportional to $\frac{1}{R^2}$ for fixed J. Since these corrections are rather small, all rotational effects will be neglected in this thesis and a non-rotating diatomic will be assumed in the following chapters.

2.3 Molecules in electromagnetic fields

Until now, the Hamiltonian has been time-independent, and a molecule prepared in an eigenstate would always remain in that state. The total energy is conserved, too. In a non-static electromagnetic field, this is no longer the case. The interaction with the field is modelled by adding an explicitly time-dependent term to the Hamiltonian. This allows for transitions between states and changes in energy via the absorption or emission of photons. More importantly, the molecule can be *driven* into a desired state by an appropriately designed field. Lasers, providing a wide range of strong, coherent light fields in the visible to IR range, have become the most important tool in quantum control of molecules [11].

Some approximations and assumptions

There are different ways to state the interaction between light and matter. This work will stick to the semi-classical approach, which treats the molecule as a quantum object, but the light field classically[6]. Furthermore the *length gauge* is used, making the interaction term particularly simple[7]. Since the wavelength of such lasers is on the order of at least several hundred nanometres, the *dipole approximation* is justified. It states that the electric field can be assumed to depend solely on time, not on position. For small molecules extending over little more than a few Ångstrøm, this is pretty accurate [11]. In the dipole approximation, the electric field $\mathbf{E}$ of an idealized (i.e. perfectly monochromatic) laser can be written as

$$\mathbf{E}(t) = \mathbf{E}_0 \cdot \cos(\omega \cdot t + \Delta) \tag{2.17}$$

Here Δ is a (usually irrelevant) phase, and $\mathbf{E}_0 = E_0 \cdot \boldsymbol{\varepsilon}$ contains the amplitude E_0 and polarization vector $\boldsymbol{\varepsilon}$ of the field[8]. Assuming linear polarization, one can choose coordinates such that the x axis coincides with the polarization, projecting the last equation to one dimension.

Electric dipole moment

An electric field exerts no total force on a neutral molecule, but couples to it via its *dipole moment*. When $\hat{H}_0 = \hat{T}_n + U(R)$ is the unperturbed Hamiltonian of nuclear motion, the dynamics in the field $\mathbf{E}(t)$ are governed by the Hamiltonian [8]

$$\hat{H} = \hat{H}_0 - \boldsymbol{\mu} \cdot \mathbf{E}(t) \tag{2.18}$$

[6] A full quantum approach would require quantum electrodynamics and is not necessary at this point [18].

[7] There is no need to dive into gauge theory here, so let it suffice to say that Maxwell's equations are invariant under a field transformation $(\Phi, \mathbf{A}) \mapsto (\Phi - \dot{\chi}, \mathbf{A} + \nabla\chi)$ for any scalar function $\chi(\mathbf{r}, t)$.
χ can be chosen such that $\mathbf{A}$ vanishes and $\Phi = -\mathbf{r} \cdot \mathbf{E}$, removing any $\mathbf{A}$ terms from the TDSE [11].

[8] Apologies for using the same letter E for energies and electric fields. Care was taken to explicitly state which quantity is meant whenever the context is unclear.

Here $\boldsymbol{\mu}$ is the *transition dipole moment* of the molecule. Its matrix elements can be calculated by integrating the analogue of the classic dipole moment [11]

$$\boldsymbol{\mu}_{fi}(\mathbf{R}) = \left\langle \phi_f^{el} \left| \sum_{k=1}^{N_n+N_e} q_k \cdot \mathbf{r}_k \right| \phi_i^{el} \right\rangle_{el} \tag{2.19}$$

The sum runs over all charged particles (nuclei and electrons) in the molecule, with the charge q_k and position $\mathbf{r}_k$ (for a moment, the convention to use $\mathbf{r}$ exclusively for electrons is abandoned). Integration in the scalar product is performed over the electronic coordinates. ϕ_i^{el} and ϕ_f^{el} denote the initial and final state of a transition. The off-diagonal elements $f \neq i$ represent transitions between different electronic states, while the diagonal elements $f = i$ are responsible for vibrational transitions on a single PES; the indices are usually dropped in the latter case. $\boldsymbol{\mu}(\mathbf{R})$ then denotes the expectation value of the dipole operator, or the *permanent molecular dipole moment*[9].

In the special case of a non-rotating diatomic molecule, this reduces to a one-dimensional function of one variable, and the full Hamiltonian takes the form

$$\hat{H} = -\frac{1}{2M_r}\frac{\partial^2}{\partial R^2} + U(R) - \mu(R) \cdot E(t) \tag{2.20}$$

The electric dipole moment has the dimensions *charge · distance*. Since the SI unit C·m is way too large to be useful in chemistry, it is often measured in atomic units (with $1e \cdot a_0 = 8.48 \cdot 10^{-30}\, C \cdot m$) or Debye ($1D = 3.34 \cdot 10^{-30}\, C \cdot m = 0.393\, a.u.$). Typical values for diatomic molecules lie between 0 and 20 atomic units [8].

It is worth noting that a molecule has a non-zero permanent electric dipole moment if and only if the centre of charge of the nuclei differs from the centre of charge of the electrons [8]. Therefore molecules with inversion symmetry, such as CO_2 or H_2, have a vanishing dipole moment and cannot be vibrationally excited with lasers. In the diatomic case, this rules out all homonuclear molecules, so only heteronuclear molecules are accessible to IR spectroscopy.

The dipole moment $\mu(R)$ is usually a non-linear function of the position, although a linear approximation may be reasonable in some cases. A popular model is the *Mecke function* [11]

$$\mu(R) = \mu_0 \cdot R \cdot e^{-R/R^*} \tag{2.21}$$

with the parameter R^* typically of the same order of magnitude as the internuclear distance. An example of such a function is plotted in figure 2.3. Close to the equilibrium distance, the approximation

$$\mu(R) \approx -\mu' \cdot (R - R_0) + \mu(R_0) \tag{2.22}$$

[9] To be distinguished from *induced* or *temporary* dipole moments, which are important for Van der Waals interaction between unpolar molecules, but shall not be dealt with here.

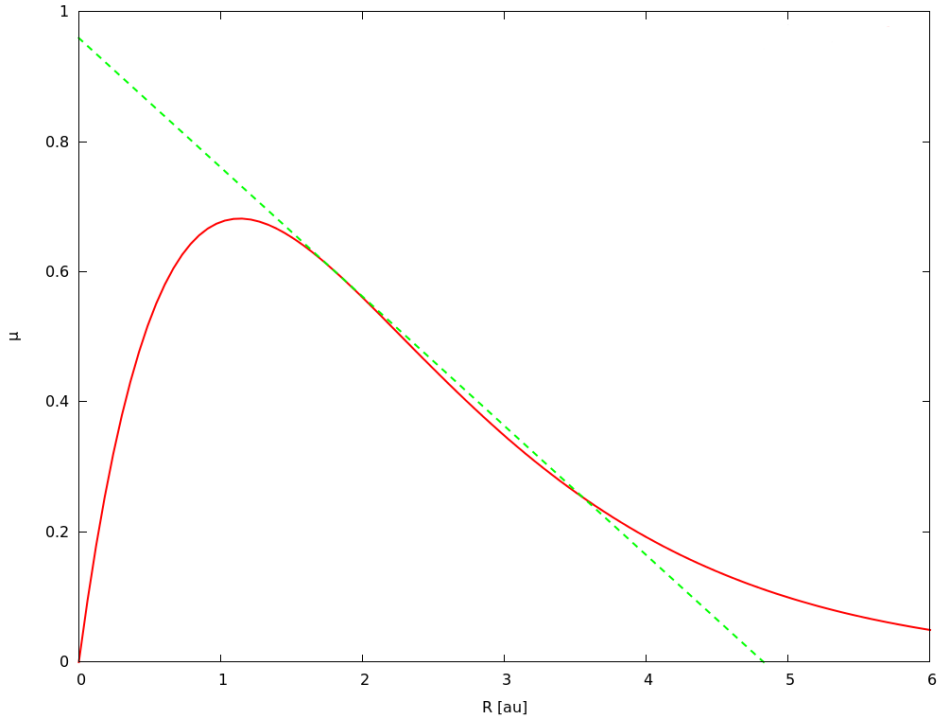

Figure 2.3: Mecke function with $R^* = 1.134$, $\mu_0 = 1.634$ and linear approximation at $R_0 = 1.821$. This models the OH stretching mode in water [15]. Figure after [11].

with the *dipole gradient* $\mu' = -\frac{\mathrm{d}\mu}{\mathrm{d}R}(R = R_0) = \mu_0 \cdot e^{-R_0/R^*} \cdot (R_0/R^* - 1)$ holds.

Rabi oscillations

As a simple example of light-matter interaction, consider an electron in a two-level system with a monochromatic electric field $E(t) = E_0 \cos(\omega t)$. The unperturbed eigenstates are $|g\rangle$ and $|e\rangle$ with the energies E_g and E_e. The Hamiltonian is

$$\hat{H} = E_g|g\rangle\langle g| + E_e|e\rangle\langle e| + \Omega \cdot \cos(\omega t) \tag{2.23}$$

where $\Omega = \mu_{12} \cdot E_0 = \langle e|\hat{r}|g\rangle \cdot E_0$ is called the *Rabi frequency*. The Schrödinger equation can be solved analytically with the linear combination ansatz $|\Psi(t)\rangle = c_g(t) \cdot |g\rangle + c_e(t) \cdot |e\rangle$, for a detailed calculation see e.g. [11].

In case of resonance, with i.e. $\omega = |E_e - E_g|$, the system oscillates between the two states with the Rabi frequency [11]. Starting with full population of $|g\rangle$ at $t = 0$, the time-dependent populations are

$$p_g(t) = |c_g(t)|^2 = \cos^2\left(\frac{\Omega t}{2}\right) \tag{2.24}$$

$$p_e(t) = |c_e(t)|^2 = \sin^2\left(\frac{\Omega t}{2}\right) \tag{2.25}$$

When the driving field is detuned by an amount $\Delta = |E_e - E_g| - \omega$, the oscillation is faster with the frequency $\Omega' = \sqrt{\Omega^2 + \Delta^2}$. However no complete population transfer is possible with a detuning, the maximum excited population is $\max(p_e(t)) = (\Omega/\Omega')^2$.

Population transfer is a common goal in optimal control, so it is worth taking a closer look at when it happens in a Rabi oscillator. Obviously $p_e = 1$ is true for $\Omega t = \pi, 3\pi, 5\pi, \ldots$

In control experiments, laser pulses are often used rather than constant amplitude fields (cw lasers). The electric field is therefore modified to $E(t) = E_0 \cdot f(t) \cdot \cos(\omega t)$ with an *envelope* function $f(t)$. Typical pulse shapes are Gaussian or $\sin^2$ functions. Now the *area theorem* can be shown to hold: It states that the population transfer only depends on the area under the envelope function, not on the form of $f(t)$. As a corollary, complete population transfer occurs (resonance assumed) whenever $\int_0^t f(\tau)\mathrm{d}\tau = \pi$. Such a pulse is accordingly called a π-pulse. Similarly, a $\frac{\pi}{2}$-pulse can be used to obtain a coherent superposition state $\frac{1}{\sqrt{2}}(|e\rangle + |g\rangle)$ [11].

At first glance these results seem not very useful, as molecules are never true two-level systems. But it turns out that many transitions can be effectively modelled this way if there are no neighbouring states with similar transition energies. In fact, even the resonant excitation from the ground state to the first vibrational state in a Morse oscillator can behave according to equation (2.23) because the off-resonant excitation to higher states is much weaker than the $|0\rangle \rightarrow |1\rangle$ transition. Since both states are rather localized around the equilibrium distance, even the linearised dipole moment of equation (2.22) can be used for good results.

2.4 Quantum Optimal Control

Now that the tools are available to calculate the evolution of a nuclear wavepacket under an external field, it is tempting to ask the inverse question: Given an initial and a target state, can a matching light pulse be found?

A more general statement of the problem reads: Given a fixed evolution time T, an initial state $\Psi(t = 0)$ and a Hermitian operator $\hat{O}$, what is the function $E(t)$ that extremizes the expectation value $|\langle\Psi(T)|\hat{O}|\Psi(T)\rangle|^2$ in the final state $\Psi(T) = e^{-i\hat{H}T}\Psi(0)$? In order to restrict the field to physically meaningful and experimentally feasible values, some type of penalty term is added to receive a *cost functional* which shall be minimized:

$$J[E] = 1 - |\langle\Psi(T)|\hat{O}|\Psi(T)\rangle|^2 + \alpha \cdot \int_0^T |E(t)|^2 \mathrm{d}t \tag{2.26}$$

The integral is proportional to the total pulse energy, multiplied by a suitable *penalty factor* α. It should be noted that other, more sophisticated penalty functions have been used which also punish high field gradients or undesirable pulse shapes [4, 5].

A common choice for $\hat{O}$ is the projection operator onto a specific target state, so the optimal control problem becomes a matter of minimizing the *infidelity* $I = 1 - |\langle\Psi(T)|\Psi_{\mathrm{Target}}\rangle|^2$ while keeping the field strength moderate [23].

Optimal control problems can be tackled both experimentally and theoretically. The experimental approach usually employs adaptive feedback control (AFC), which implements a closed loop design in the laboratory. The system under study is subjected to a shaped light pulse and its response is measured. From this result, a learning algorithm calculates a modified pulse, which is again fed into the pulse shaper. This process is repeated until – ideally – the control target is reached [4].

Although AFC is crucial for optimal control in practice and has produced great results, this thesis will exclusively deal with the complementary approach, optimal control *theory* (OCT). It undoubtedly has its disadvantages compared to AFC: The wavefunction has to be propagated with some effort and under many approximations, while the molecule in the laboratory solves its own Schrödinger equation in real time. Furthermore, the optimized pulses resulting from theoretical calculations are often hard to implement in reality.

Still OCT is justified: It can be much easier to set up a simulation with a model Hamiltonian than conducting an experiment, especially for systems which are too unstable, noisy or exist only under extreme conditions. The theoretically optimized pulse may not perform best in practice, but can usually give a good initial guess for AFC. Most importantly, calculations may give a better understanding of the key processes driving the system, allowing for a more directed search in the laboratory [4].

A number of optimal control algorithms exist to iteratively find an optimal pulse. As an illustrative example, consider the pump-dump scheme [16]. As a precursor to modern OCT methods, the pump-dump scheme (also known as Tannor-Rice scheme) is very simply structured, but it makes the connection of equation (2.26) to laser selective chemistry clearer than other, more abstract methods [11].

Assume a chemical reaction with two possible outcomes: A molecule $\mathrm{A_2B}$ can dissociate into $\mathrm{A_2} + \mathrm{B}$ or $\mathrm{A} + \mathrm{AB}$. Each channel corresponds to a valley in the ground state surface S_0 (see fig. 2.4) leading to dissociation. The excited electronic state PES S_1 has a roughly parabolic shape in this example. The molecule is then exposed to two consequent laser pulses. The *pump* pulse excites the system to the higher PES, lifting the nuclear wavefunction vertically (i.e. without change in the nuclear coordinates). The wavefunction is now generally not in a vibrational eigenstate of S_1, so it will propagate on the surface. After a while (typically tens of fs) the *dump* pulse de-excites the molecule back to the ground state. Depending on the delay between pump and dump pulse, the wavepacket will end up in a different valley of the ground state PES and continue to propagate along this route. Hence with an appropriately chosen delay, the yield of the desired dissociation channel can be enhanced.

This technique, pioneered by D.J. Tannor and S.A. Rice [16], can be considered to be the first practical optimal control scheme, although in its very basic version described above, it is performed with only one parameter. However, pulse shapes, phases and frequencies can also be optimized to further increase the selectivity of the reaction.

Despite its appeal, the pump-dump scheme is very limited. Depending on the pulse length

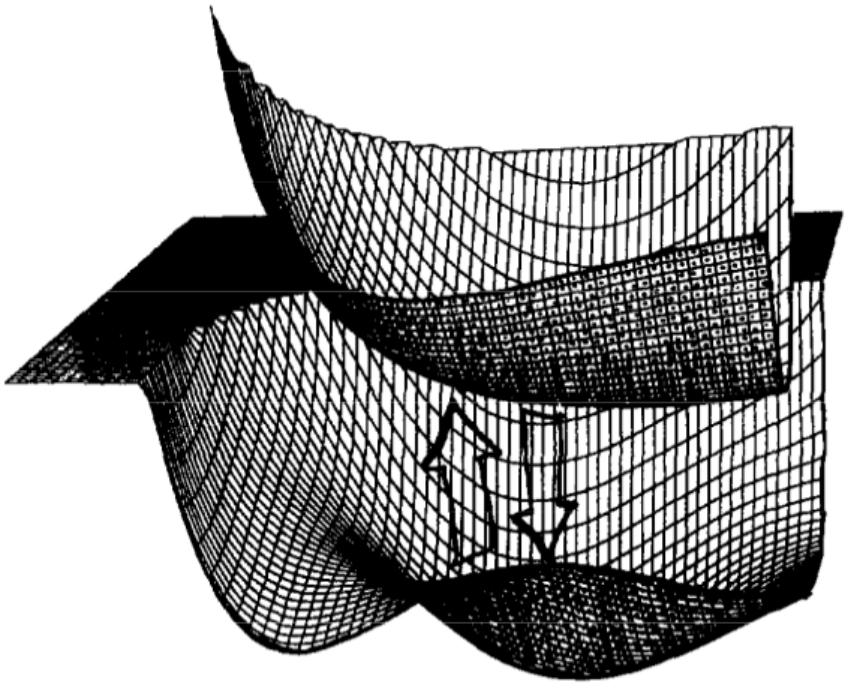

Figure 2.4: Ground and excited state PESs of an A_2B molecule. The arrows indicate possible pump and dump pulses (image from [16]).

and the shape of the excited potential surface, dispersion can become a serious problem. The wavepacket will then lose its (previously localized) shape, reducing the selectivity [16]. Furthermore, only a few specific systems exhibit the necessary structure of potential energy surfaces, while most molecules are not suitable for the pump-dump scheme at all. Therefore, a more generalized approach for OCT is needed, e.g. the *Krotov method*. It provides an iterative algorithm which produces successively better field guesses [11]. It is suitable (and has been used) for a wide range of quantum control problems; however only its application to quantum chemistry problems is of interest here. The mathematics is rather tedious and not very relevant at this point, so the reader may consult Krotov's comprehensive book on the subject[17] or the summary in [11] for details.

2.5 Non-adiabatic dynamics

Until now all coupling between electronic and nuclear motions has been neglected. This approach will be pursued for the rest of this thesis, but its limits and the occasional breakdown of the BO approximation shall be discussed here.

In the purely electronic Schrödinger equation (2.5), the nuclear kinetic energy $\hat{T}_n$ was neglected as it is generally much smaller than the residual Hamiltonian $\hat{H}_0 = \hat{V} + \hat{T}_e$ In an accurate description, it must be treated as a perturbation $\lambda \cdot W$. In perturbation theory, the total

Hamiltonian is written as

$$\hat{H} = \hat{H}_0 + \lambda W \tag{2.27}$$

where usually $\lambda = (m/M)^{\frac{1}{4}}$ is used as the perturbation parameter [8]. When neglecting the perturbation term, the unperturbed electronic eigenstates ϕ_n^{el} and eigenenergies $E_n^{(0)}$ are found. Since $\lambda \ll 1$, the actual energies can be found by means of a series expansion:

$$E_n = E_n^{(0)} + W_{nn} + \sum_{k \neq n} \frac{W_{nk} + W_{kn}}{E_n^{(0)} - E_k^{(0)}} + \mathcal{O}(\lambda^3) \tag{2.28}$$

The third order terms are often neglected, since even for hydrogen $(m/M)^{\frac{3}{4}} < 4 \cdot 10^{-3}$. The first and second order correction terms depend on the matrix elements of the perturbation operator, i.e. the nuclear kinetic energy:

$$W_{nk} = \langle \phi_n^{el} | \hat{T}_n | \phi_k^{el} \rangle = \int (\phi_n^{el})^* \hat{T}_n \phi_k^{el} \mathrm{d}^3\mathbf{r} \tag{2.29}$$

These matrix elements describe the coupling between electronic states due to nuclear motion [8]. As long as the energy separation $E_n^{(0)} - E_k^{(0)}$ between these states is large compared to W_{nk}, the coupling is weak and the expansion (2.28) holds. But when two electronic surfaces are close or even intersecting, the correction terms become large and the series diverges. This is when the BO approximation breaks down and the coupling becomes too strong to be treated perturbatively.

In this case, even small changes in nuclear motion can trigger transitions between electronic states. Effect such as radiationless decays occur, i.e. electronic transitions without emission of a photon – the surplus energy is transferred into vibrational or rotational modes. Methods exist to model molecular behaviour beyond the BO approximation, but they often go with greater computational effort [26].

The ground state surface is usually well separated from excited surfaces [8], so the BO approximation is universally adopted for the rest of this thesis.

3 Numerical Methods

The purpose of this chapter is to make the reader familiar with the computational tools used in this work. All propagation calculations in this work are performed with MCTDH (section 3.1), whereas CRAB (section 3.2) is being used for optimization of the external field. Since CRAB is a general approach, a specific optimization algorithm has to be chosen. The ones used here are the Nelder-Mead (or simplex) method and the Subplex method.

3.1 MCTDH

In this thesis the Multi-Configurational Time-Dependent Hartree method is the tool of choice to simulate the time evolution of molecular systems. It is best understood by comparison with two competing schemes for propagating wavepackets [20]. Therefore sections 3.1.1 and 3.1.2 will first introduce the numerically exact Full Configuration Interaction (Full-CI) and the approximate time-dependent Hartree (TDH) method, respectively. In structure and notation, this section closely follows the lecture notes [20] by MCTDH co-inventor HD Meyer, which should be consulted for further comments and proofs.

3.1.1 Full-CI

The Full-CI approach (dubbed the *standard method* in [3]) is arguably the most straightforward way of representing a multidimensional wavefunction. Consider a wavefunction $\Psi(Q_1, \ldots, Q_f, t)$ depending on the f coordinates Q_1 to Q_f and on time. It may represent the nuclear positions on an f-dimensional PES, but the considerations below are fully general. It is now intuitive to expand Ψ in a time-independent basis:

$$\Psi(Q_1, \ldots, Q_f, t) = \sum_{j_1=1}^{N_1} \ldots \sum_{j_f=1}^{N_f} C_{j_1 \ldots j_f}(t) \chi_{j_1}(Q_1) \ldots \chi_{j_f}(Q_f) \tag{3.1}$$

The functions $\chi_{j_\kappa}(Q_\kappa)$ can be any orthonormal basis, chosen according to the specific degree of freedom. For example, one might select Harmonic Oscillator (HO) eigenfunctions for a vibrational mode or Legendre functions for angular coordinates. N_κ then gives the basis size for this degree of freedom and must be chosen in a trade-off between the desired accuracy (the method is exact for $N \to \infty$) and computational effort.

In this representation, all time dependence lies in the coefficients $C_{j_1 \dots j_f}(t)$. Their equations of motion can be found either directly by inserting the ansatz into the TDSE or equivalently with a variational principle, i.e. by demanding $\langle \delta\Psi | \hat{H} - i\frac{\partial}{\partial t} | \Psi \rangle = 0$ [20]. One finds [3]

$$i\dot{C}_L = \sum_J \langle \chi_J | \hat{H} | \chi_L \rangle C_J \tag{3.2}$$

The multi-indices $J = (j_1, \dots, j_f)$ have the meaning $\chi_J = \chi_{j_1}(Q_1) \dots \chi_{j_f}(Q_f)$ (and similar for C_J), while χ_J is called a *configuration*.

The equation of motion (3.2) is a set of first order differential equations, which is formally simple, but hard to solve in many practical cases. It involves $N_1 N_2 \cdots N_f$ coupled equations, and each N_κ should at least be about 10 (usually more) for good accuracy.

This exponential scaling makes Full-CI calculations impossible for anything but small systems. Even massively parallel computing systems cannot handle more than six or seven degrees of freedom within reasonable time [20].

3.1.2 TDH

To circumvent the limitations of the Full-CI method, approximations have to be made. A very popular and successful simplification is the TDH approach [8]. The ansatz is [20]:

$$\Psi(Q_1, \dots, Q_f, t) = \prod_{i=1}^{f} a(t) \phi_i(Q_i, t)$$

Instead of a time-independent basis, TDH uses so-called *single particle functions* (SPFs) $\phi_i(Q_i, t)$ which are to be considered as wavefunctions of a single particle moving along coordinate Q_κ. The wavefunction Ψ is approximated as a single product of SPFs, a so-called *Hartree product*. This greatly reduces the computational effort required for propagation.

Note that this representation is not unique, since arbitrary factors can be shifted between the SPFs and the prefactor $a(t)$. In order to remove this redundancy, *constraint functions* have to be imposed. A general way to state the constraint functions g_κ is

$$g_\kappa(t) = i\langle \phi_\kappa | \dot{\phi}_\kappa \rangle \tag{3.3}$$

It is easy to show that all g_κ have to be real in order to preserve the norms $\|\phi_\kappa\|$, but otherwise they can be arbitrary functions of time [20]. These can be chosen in a way that simplifies the resulting equations of motion.

To state these equations, a little notation should be introduced. In analogy with the Full-CI

approach,

$$\Phi = \prod_{i=1}^{f} \phi_i(Q_i, t) \tag{3.4}$$

is called a *configuration*. The single-hole configurations $\Phi^{(\kappa)}$ are defined by

$$\Phi^{(\kappa)} = \frac{\Phi}{\phi_\kappa} = \prod_{i \neq \kappa} \phi_i(Q_i, t) \tag{3.5}$$

By separating all variables Q_κ, the TDH approach makes it necessary to account for particle interaction in an averaged way. Here the *mean field operators*

$$\mathcal{H}^{(\kappa)} = \langle \Phi^{(\kappa)} | \hat{H} | \Phi^{(\kappa)} \rangle \tag{3.6}$$

come in handy. Each of these operators acts only on the κth degree of freedom, as all other variables have been integrated over. When acting on the SPF ϕ_κ, it effectively approximates the influence of all other particles by their averaged density.

This allows to state the equations of motion in the TDH approach:

$$\begin{aligned} i\dot{a} &= \left(E - \sum_{i=1}^{f} g_i \right) a \\ i\dot{\phi}_\kappa &= (\mathcal{H}^{(\kappa)} - E + g_\kappa)\phi_\kappa \end{aligned} \tag{3.7}$$

where the suggestive abbreviation $E = \langle \Phi | \hat{H} | \Phi \rangle$ has been used. Note that all terms in equation (3.7), including E, can depend on time.

It is now obvious why TDH is much faster than Full-CI: Instead of $\sim N^f$, now only $N \cdot f$ equations[1] have to be solved [20].

Before doing so, the constraint functions must be specified. Apart from the simple and obvious choice $g_\kappa(t) \equiv 0$, an interesting result occurs for $g_\kappa(t) = E(t)/f$. The equation of motion for a then simplifies to $\dot{a} = 0$, resulting in

$$\begin{aligned} a(t) &= a(0) = \text{const.} \\ i\dot{\phi}_\kappa &= \left(\mathcal{H}^{(\kappa)} - \frac{f-1}{f} \cdot E \right) \phi_\kappa \end{aligned} \tag{3.8}$$

This can easily be solved for tens of degrees of freedom with current technology. The main computational effort stems from calculating the mean-fields $\mathcal{H}^{(\kappa)}$ at every time step, which by definition requires integrating over $f - 1$ dimensions. Fortunately, there are ways to reduce this

[1] The $f + 1$ equations of (3.7) can be reduced to f by suitable choice of g_κ, see the following paragraph for an example. For an actual calculation the SPFs still have to be expanded in a finite basis, here assumed to have equal size N for all coordinates.

work, e.g. by approximating the mean-fields as a sum of lower-dimensional integrals.

TDH's computational efficiency comes at the cost of systematic errors. The separation ansatz is exact if the Hamiltonian can be split into a sum $\hat{H} = \hat{H}_{\text{sep}} = \hat{h}^{(1)} + \ldots + \hat{h}^{(f)}$ where each $\hat{h}^{(\kappa)}$ is a one-particle operator, i.e. only acts on the κth degree of freedom. This is usually true for kinetic energy operators, but not for most potentials. Here the Hamiltonian contains a non-separable part $\hat{H} = \hat{H}_{\text{sep}} + \hat{V}$. The error between the exact propagation and the TDH result is proportional to the difference between the true and the averaged potential $(\hat{V} - \langle\hat{V}\rangle)$. Hence TDH is accurate when the potential changes only weakly over the width of the wavepacket. This condition is satisfied for well-localized wavefunctions in flat potentials. Notable errors are introduced when the wavefunction is widely spread or when the potential is very steep, resulting in large changes in $\hat{V} - \langle\hat{V}\rangle$. This is often the case for higher vibrational states or whenever strong repulsion occurs (e.g. when going to small R in a Morse potential) [20].

3.1.3 MCTDH

Although it has its merits, TDH is often too crude to give reliable results [8]. This is especially true in correlated systems which are characterized by strong non-separable contributions to the Hamiltonian [20, 3]. Full-CI computes all correlation effects correctly, but is too inefficient for larger systems. The Multi-Configuration Time-Dependent Hartree method (MCTDH) attempts to combine the advantages of both methods[19].

The wavefunction is expanded as a sum of Hartree products:

$$\Psi(Q_1, \ldots, Q_f, t) = \sum_{j_1=1}^{n_1} \ldots \sum_{j_f=1}^{n_f} A_{j_1 \ldots j_f}(t) \varphi_{j_1}^{(1)}(Q_1, t) \ldots \varphi_{j_f}^{(f)}(Q_f, t) \equiv \sum_J A_J(t) \Phi_J(\mathbf{Q}, t) \tag{3.9}$$

In the last expression the multi-indices introduced in section 3.1.1 as well as the configurations from equation (3.4) are used to shorten the multiple sums and products. This ansatz contains both Full-CI and TDH as limiting cases: If $n_1 = \ldots = n_f = 1$, the sum would reduce to only one configuration, yielding the TDH approach. If there were no time dependence on Φ_J, the expression would be equivalent to the Full-CI representation with $\forall\kappa : n_\kappa = N_\kappa$.

In practice it is useful to choose $1 < n_\kappa < N_\kappa$ to include more than one configuration, but still reduce the basis size compared to Full-CI. MCTDH can still give as accurate results with a smaller basis due to the time dependence of the basis functions $\varphi_{j_\kappa}^{(\kappa)}$. At each time step, they are recalculated to optimally represent the current wavepacket, while the fixed basis of Full-CI may become inefficient.

As an example, consider a Gaussian wavepacket moving freely in a zero potential. The initial wavefunction (in arbitrary units) reads

$$\Psi(\mathbf{x}, t = 0) = C \cdot e^{-\frac{1}{2}\mathbf{x}^2 + i\mathbf{p}\cdot\mathbf{x}} \tag{3.10}$$

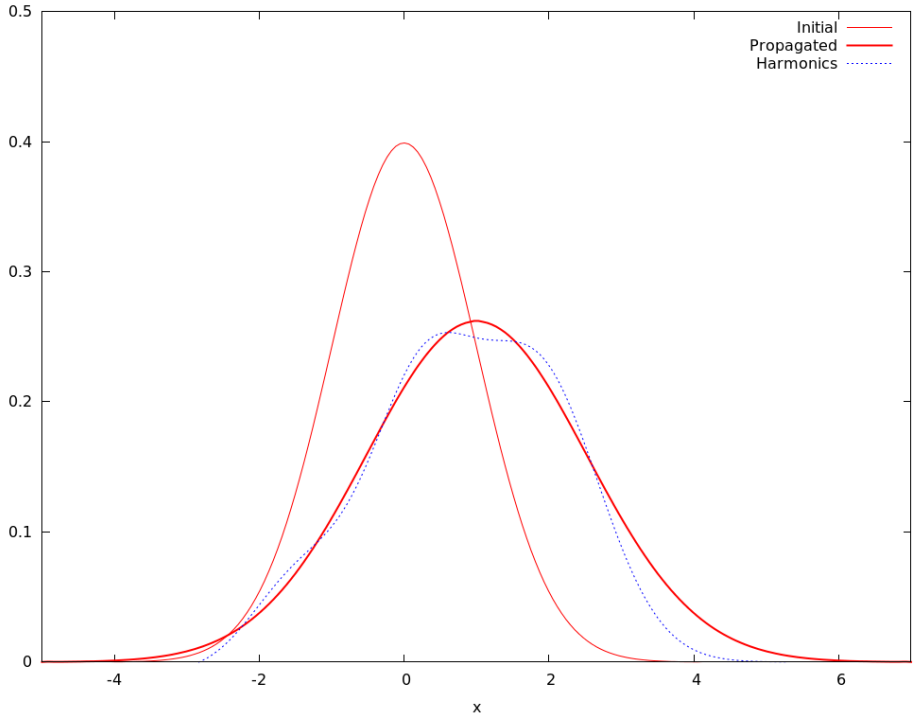

Figure 3.1: Spread of a Gaussian wavepacket. Thin red (solid) line: Initial wavefunction with momentum $p = 5$ and initial width $\Delta x_0 = 1$. Strong red (solid) line: Wavefunction (absolute value) at $t = 0.2$. Blue (dotted) line: Expansion in terms of HO functions (center and frequency according to initial wavefunction) to fifth order.

with the initial position at $\mathbf{x} = 0$, the momentum $\mathbf{p}$ and a normalization constant C. One would typically choose a HO basis to represent such a wavefunction. Since the harmonic ground state is a Gaussian, just one basis function (with a suitable width) is already sufficient for an exact description.

As Ψ evolves, it stays in Gaussian shape, but its width increases proportional to $\sqrt{1 + 4t^2}$ and it is centred around $\mathbf{p} \cdot t$ (see figure 3.1) [1]. Such moving and possibly dispersing wavepackets are characteristic of the dissociation of molecules [20]. Now the fixed basis of Full-CI quickly becomes impractical, while a time-dependent basis of shifted and rescaled HO eigenfunctions remains efficient. One advantage of MCTDH is to always use such an optimal basis set. This also applies to non-Gaussian wavepackets.

When compared to TDH, MCTDH performs better since it accounts for correlation effects. With a good choice of configurations, all important correlations are covered. Little to no memory is wasted on weakly or uncorrelated modes as in Full-CI, which by definition considers *all* configurations and possible correlations. The performance of MCTDH crucially depends on the choice configurations [3].

After this prelude, it is time to introduce some more notation before turning towards the equations of motion. Similar to TDH, there will be equations to propagate not only the coefficient

vector[2], but also the SPFs. Another common feature is the need for constraints because the representation (3.9) is not unique. Not only can time dependent factors be shifted between the A-vector and the configurations Φ_J, but also changes in the SPF basis are possible. Any linear map $U^{(\kappa)} : \mathbb{R}^{n_\kappa} \to \mathbb{R}^{n_\kappa}$ can be performed on the κth SPF basis to obtain the transformed SPFs

$$\tilde{\boldsymbol{\varphi}}^{(\kappa)} = U^{(\kappa)} \boldsymbol{\varphi}^{(\kappa)} \tag{3.11}$$

where $\boldsymbol{\varphi}^{(\kappa)}$ should be read as a vector $(\varphi_1^{(\kappa)}, \dots, \varphi_{n_\kappa}^{(\kappa)})$. When simultaneously $\mathbf{A}$ is subjected to the inverse transformation(s)

$$\tilde{\mathbf{A}}_J = \sum_L \mathbf{A}_L \left(U^{(1)}\right)^{-1} \cdots \left(U^{(f)}\right)^{-1} \tag{3.12}$$

the wavefunction Ψ remains invariant. Instead of the constraint functions of TDH, MCTDH requires constraint *operators* $\hat{g}^{(\kappa)}$. The simplest way to define them is

$$i\langle \varphi_l^{(\kappa)} | \dot{\varphi}_j^{(\kappa)} \rangle = \langle \varphi_l^{(\kappa)} | \hat{g}^{(\kappa)} | \varphi_j^{(\kappa)} \rangle \equiv g_{lj}^{(\kappa)} \tag{3.13}$$

for all $\kappa = 1, \dots, f$. Just as a real constraint function was chosen earlier to conserve the norm, hermitian constraint operators (i.e. $\boldsymbol{g}^{(\kappa)} = \boldsymbol{g}^{(\kappa)\dagger}$) ensure orthonormality of the $\varphi_l^{(\kappa)}$ (as long as this was given at $t = 0$).

A generalization of the previously used multi-indices is now introduced. As a reminder, a multi-index J is shorthand for $(j_1, \dots, j_f)$. Now let J^κ be a tuple of indices with the κth entry *omitted*, and let J_l^κ denote a multi-index with the κth entry *replaced* by l. In equations:

$$J^\kappa = (j_1, \dots, j_{\kappa-1}, j_{\kappa+1}, \dots, j_f) \tag{3.14}$$

$$J_l^\kappa = (j_1, \dots, j_{\kappa-1}, l, j_{\kappa+1}, \dots, j_f) \tag{3.15}$$

$$\tag{3.16}$$

In this notation, the single-hole configurations from section 3.1.2 are written as

$$\Phi_{J^\kappa} = \prod_{\nu \neq \kappa} \varphi_{j_\nu}^{(\nu)} = \frac{\Phi_J}{\varphi_{j_\kappa}^{(\kappa)}} \tag{3.17}$$

This also allows to define *single-hole functions*

$$\Psi_l^{(\kappa)} = \sum_{J^\kappa} A_{J_l^\kappa} \Phi_{J^\kappa} \tag{3.18}$$

$\Psi_l^{(\kappa)}$ is a function of $f - 1$ coordinates, with all SPFs which on Q_κ ruled out from Ψ. Thanks to

[2]Technically, $\mathbf{A} = A_{j_1 \dots j_f}$ is not a vector, but a rank f tensor. Still the term *A-vector* is used throughout the reference [3] and consequently here, too.

the completeness of the SPF bases, the identity $\Psi = \sum_{l=1}^{n_\kappa} \varphi_l^{(\kappa)} \Psi_l^{(\kappa)}$ holds.

Using the single-hole functions, the *mean field* operators

$$\langle H \rangle_{jl}^{(\kappa)} = \left\langle \Psi_j^{(\kappa)} \middle| \hat{H} \middle| \Psi_l^{(\kappa)} \right\rangle \tag{3.19}$$

and the *density matrix*

$$\rho_{kl}^{(\kappa)} = \left\langle \Psi_k^{(\kappa)} \middle| \Psi_l^{(\kappa)} \right\rangle = \sum_{J^\kappa} A_{J_k^\kappa}^* A_{J_l^\kappa} \tag{3.20}$$

can be defined. Again, the mean fields only act on the κth degree of freedom after everything else has been integrated over.

The same applies to the MCTDH density matrix, which should not be confused with the common definition of a density operator [20, 3]. The latter is $\hat{\rho} = |\Psi\rangle\langle\Psi|$ for a pure state and operates on all degrees of freedom. Only after tracing out all other degrees of freedom[3], the *reduced* density is found which coincides with the definition (3.20) above.

Remembering the end of section 3.1.2, the Hamiltonian can be split into a separable and a residual part $\hat{H} = \sum_{i=1}^{f} h^{(i)} + \hat{H}_R$, where the $h^{(\kappa)}$ are one-particle operators. Since the effect of the separable part is easy to evaluate, only the residual Hamiltonian needs to be approximated by mean fields:

$$\mathcal{H}^{(\kappa)} = \langle \hat{H}_R \rangle^{(\kappa)} \tag{3.21}$$

Finally, after introducing the *projector* onto the subspace of functions of the Q_κ coordinate

$$P^{(\kappa)} = \sum_{j=1}^{n_\kappa} |\varphi_j^{(\kappa)}\rangle\langle\varphi_j^{(\kappa)}| \tag{3.22}$$

all tools are set up to state the equations of motion. They are found with the Dirac-Frenkel variational principle, i.e. by taking the functional derivatives of Ψ with respect to the coefficients A_J, the SPFs $\boldsymbol{\varphi}^{(\kappa)}$ and time and then demanding

$$\left\langle \delta\Psi \middle| H - i\frac{\partial}{\partial t} \middle| \Psi \right\rangle = 0 \tag{3.23}$$

This leads to separate equations of motion for A_J and $\boldsymbol{\varphi}^{(\kappa)}$ which still depend on the chosen constraint operators. The full calculation can be found in [20], at this point just the results for

[3] The trace of a density matrix is $\sum_n \langle\phi_n|\hat{\rho}|\phi_n\rangle$ where the $|\phi_n\rangle$ form a complete orthonormal basis. In this case the SPFs of the desired degrees of freedom provide such a basis, and a trace is performed over all SPFs exact those for DOF κ.

$\hat{g}^{(\kappa)} = 0$ shall be stated. These are the full MCTDH equations of motion [20]

$$\begin{aligned} i\dot{A}_J &= \sum_L \langle \Phi_J | \hat{H} | \Phi_L \rangle A_L \\ i\dot{\varphi}_j^{(\kappa)} &= \left(1 - P^{(\kappa)}\right) \left[h^{(\kappa)} \varphi_j^{(\kappa)} + \sum_{k=1}^{n_\kappa} \sum_{l=1}^{n_\kappa} \left(\rho^{(\kappa)}\right)_{jk}^{-1} \mathcal{H}_{lk}^{(\kappa)} \varphi_l^{(\kappa)} \right] \end{aligned} \tag{3.24}$$

As soon as the separable and the residual (correlated) part of the Hamiltonian have been identified and the initial SPFs have been defined, these equations can be used to start calculations right away. Any numerical integrator such as Runge-Kutta can be used to solve the differential equations. Some refinements to the algorithm exist to further reduce CPU time and memory requirements, most notably *mode combination* (aggregating several physical coordinates into one logical coordinate $Q_\kappa = (q_1, \ldots, q_k)$ with only one SPF $\varphi(Q_\kappa)$) and *Constant Mean Fields* (saving time by updating the mean fields not at every time step). Although they can increase the performance of MCTDH dramatically, the interested reader is referred to the lecture notes [20] for a thorough description.

The limiting factor in calculations is often the memory consumption, so it is interesting to compare MCTDH with Full-CI here. The latter has to store a large coefficient vector C_J with N^f entries[4], and memory consumption is proportional to this number.

Plain MCTDH stores a number of variables proportional to $n^f + f \cdot n \cdot N$ where the first term is the number of entries in the A-vector and the second term accounts for the SPFs. Some extra space is required for the mean fields etc., but the overall scaling does not change. Since the number n of SPFs is usually much smaller than the grid size N, the exponential part grows much faster in Full-CI than in MCTDH, resulting in a gain of $(N/n)^f$ [20].

As a typical example, let $N = 32$ and $n = 7$. For four degrees of freedom, Full-CI requires about 48 MB of memory and MCTDH just 620 kB. The difference becomes even greater for more degrees of freedom. For $f = 9$, Full-CI would need about 1.5 PB which is absolutely impossible, while MCTDH still works with less than 8 GB. With mode combination, over thirty degrees of freedom have been handled [3].

In terms of CPU time, MCTDH can be shown to beat Full-CI by a similar factor of roughly $(N/n)^{f+1}$.

The Heidelberg MCTDH package

There are several implementations of the MCTDH scheme, but the most prominent one has been developed by scientists of the Universität Heidelberg [25, 3, 19]. After more than 15 years of development, the Heidelberg package now comprises a complete toolkit for multi-dimensional quantum dynamics including wavefunction propagation, diagonalization of Hamiltonians, many analysis tools and more. Originally intended for quantum chemistry, it has also been applied

[4] Again assuming that all degrees of freedom require the same basis size $N_1 = \ldots = N_f \equiv N$. Similarly, identical number of SPFs $n_\kappa \equiv n$ for all degrees of freedom is assumed in MCTDH.

to other problems where multi-dimensional wavefunctions appear, e.g. cold atoms or certain bosonic systems[5]. Even an optimal control tool named `optcntrl` was added by M. Schröder, implementing the Krotov and the Rabitz optimization schemes [23].

One advantage of the software is its ease of use. The Hamiltonian, initial wavefunction and all parameters are provided via plain text input files. However the Hamiltonian must be given as a sum of products of single-particle operators (i.e. a sum of separable parts) as in $\hat{H} = \sum_{k=1}^{s} \prod_{i=1}^{f} \hat{h}_k^{(i)}$ to work with the algorithm. This is usually not a restriction for kinetic energy operators, and many simple potentials can also be written in product form, e.g. $V(x, y) = v_1(x)v_2(y)$. Such a representation is often not given for a physical PES, but there is a solution: The Heidelberg package comes with POTFIT, a program to expand a given potential in sum-of-products form.

In this thesis the Heidelberg MCTDH package will be consistently used for all propagation calculations, specifically version 8.4.9. Therefore the name MCTDH is from now on used synonymously with this specific software. The program `optcntrl` is only used for comparison at some points, since the major part of optimization is performed with CRAB.

One important, final remark on the calculations: Since all systems treated in chapter 4 are one-dimensional, the calculations are *not* in fact performed with the MCTDH method, as the representation 3.9 is just not meaningful for $f = 1$. Still the Heidelberg package was used, hoping MCTDH will play out its strengths when turning towards higher-dimensional systems at a later point (but which are way beyond the scope of a Master's thesis). This thesis is thus a mere starting point for further research.

3.2 CRAB

Chopped Random Basis (CRAB) is a general-purpose algorithm for quantum optimal control. It was introduced by T. Caneva et al. [5] in 2011 and has been shown to be efficient for qubit manipulation, spin coupling and other systems. In this work CRAB will be used to optimize the pulse parameters for state selective excitation, while MCTDH computes the system's response to the pulse.

The basic concept of CRAB is summarized easily: The control field (i.e. the light pulse) is expanded in a finite set of randomized basis functions. The expansion coefficients are considered as variables of the cost function which must be minimized.

To be more specific, consider a system subject to the control field $\Gamma(t)$ for a fixed time T. For now one field shall be sufficient, though generalization to a tuple of fields $\vec{\Gamma}$ is straightforward. Just as before (equation (2.26)), a cost functional can be defined

$$J[\Gamma(t)] = 1 - |\langle \Psi(T) | \Psi_{\text{Target}} \rangle|^2 + \alpha \cdot \int_0^T |\Gamma(t)|^2 \mathrm{d}t \tag{3.25}$$

[5]The code was extended to include the correct symmetry relations, resulting in the software MCTDHB.

The first part measures the infidelity, while the last term minimizes the energy content of the field. Quite typical of control algorithms, CRAB works best when supplied with a good initial guess $\Gamma_{\text{guess}}(t)$ for the field. An iterative procedure is then used to optimize the corrected field

$$\Gamma(t) = \Gamma^0(t) \cdot g(t) \tag{3.26}$$

with the correction g expanded in an orthonormal basis:

$$g(t) = \sum_k c_k \chi_k(\Omega_k, t) \tag{3.27}$$

The χ_k may be any suitable set of functions which depend on parameters Ω_k, e.g. a Fourier basis or associated Laguerre polynomials[6].

As already mentioned, CRAB relies on truncating (chopping) the basis to a finite size N_c. Now the basis is *randomized* by substituting the parameters $\Omega_k \mapsto \tilde{\Omega}_k = \Omega_k \cdot (1 + r_k)$ with random numbers r_k. So the CRAB ansatz for g is

$$g(t) = \sum_{k=1}^{N_c} c_k \chi_k(\tilde{\Omega}_k, t) \tag{3.28}$$

The orthonormality of the basis is lost in the process, but the search space is enlarged. Therefore, the randomization may speed up the convergence of optimization without loss of accuracy. The authors of [5] report results of comparable quality in fewer iterations.

Applying the above to an electric field in a Fourier basis, one arrives at

$$E(t) = E_{\text{guess}}(t) \cdot \left(1 + \Lambda(t) \sum_{k=1}^{N_c} (a_n \sin(\omega_k t) + b_n \cos(\omega_k t) \right) \tag{3.29}$$

Here $\Lambda(t)$ is a function with $\Lambda(0) = \Lambda(T) = 0$, ensuring a smooth pulse shape. A common choice is $\sin^2(\pi t/T)$, which will also be used here. The frequencies ω_k can be harmonic frequencies $2\pi k/T$ or characteristic frequencies of the system at question, usually multiplied with a random factor $(1 + r_k) \in [0.5, 1.5]$. Often three to five frequencies are enough to give good results. The algorithm aims to optimize the $2N_c$ coefficients $\vec{a}$ and $\vec{b}$ until a minimum of J is found.

Now the optimization problem has been reduced to minimizing a function $f(\vec{a}, \vec{b}) = J[\Gamma(\vec{a}, \vec{b}; t)]$ with respect to the parameters $\vec{a}, \vec{b}$. The minimization of a multivariate function $f : \mathbb{R}^{2N_c} \to \mathbb{R}$ is a standard problem of applied mathematics, and a plethora of algorithms exist for the purpose of finding such a minimum. Many of them are so-called gradient methods, meaning they need the derivative of f either analytically or numerically. This is somewhat impractical for the problems in this thesis, since an analytical expression for the derivative is not known and ap-

[6]The associated Laguerre polynomials $L_k^\alpha(x)$ are the solutions of $0 = xy'' + (\alpha + 1 - x)y' + ky$, where α is any real parameter.

proximate methods show a poor performance. The following section will therefore present two non-gradient algorithms which are simple, robust and do not require any knowledge of derivatives [5].

3.3 Nelder-Mead and Subplex methods

The quantum control problem has now been wrapped into an minimization problem for the objective function[7] $f(\vec{c})$. This task will now be handed over to one of two specific algorithms. Both of them are *direct search* methods, i.e. they work by comparing function values at different points $c_k \in \mathbb{R}^n$ rather than evaluating gradients or functional derivatives. This makes this approach very versatile and insensitive to noisy objective functions.

Nelder-Mead

The Nelder-Mead simplex (NMS) method was developed by J. Nelder and R. Mead in 1965 [21] and is one of the most popular gradient-free search methods. It relies on a simplex moving through the n-dimensional search space and contracting when it has surrounded a minimum. Simplices generalize the concept of a triangle in 2D to higher dimensions [22]. An n-simplex is an n-dimensional convex polytope, i.e. it consists of a set of $n+1$ affinely independent[8] points $\vec{x}_i \in \mathbb{R}^n$ and all the points lying inside. The NMS algorithm proceeds as follows [22]:

1. Given a start value $\vec{a} \in \mathbb{R}^n$, construct the initial simplex with $\vec{x}_0 = \vec{a}$. The other vertices are usually found by moving a certain distance along the respective axis.

2. *Sort* the function values $f(\vec{x}_i)$ by size and find the vertices with the highest function value at $\vec{x}_h$ and the second highest at $\vec{x}_s$. The currently best vertex (i.e. the one with lowest f) is named $\vec{x}_l$.

3. Calculate the centroid $\vec{c}$ as the arithmetic mean of all vertices except $\vec{x}_h$ and the *reflection* $\vec{x}_r = 2\vec{x}_c - \vec{x}_h$ of $\vec{x}_h$ at the centroid. Now check ether $\vec{x}_r$ is an improvement over the previously worst vertex.

4. If $f(\vec{x}_r)$ is lower than $f(\vec{x}_s)$, replace $\vec{x}_h$ by the reflected vertex. If it is even the best vertex (i.e. $f(\vec{x}_r) < f(\vec{x}_l)$ is a new minimum), try to *expand* in this direction by setting a new vertex at $\vec{x}_r - \vec{c}$. Either way, return to step 2 with the new simplex.

5. If $f(\vec{x}_r)$ is greater than $f(\vec{x}_h)$, then the current simplex is likely to already contain the minimum. *Contract* it by setting a new vertex halfway between $\vec{x}_h$ and $\vec{c}$. If $f(\vec{x}_r)$ lies

[7] For simplicity, the two parameter vectors of the last paragraph have been combined into one vector $\vec{c} = (a_1, \ldots, a_{N_c}, b_1, \ldots, b_{N_c})$ of length $n = 2N_c$.

[8] That is, the connection vectors $\vec{x}_i - \vec{x}_j$ for $i \neq j$ form a linearly independent family. In simpler words, this condition makes sure that the polytope is really n-dimensional by excluding "triangles" consisting of just three points on a line.

between the highest and the second-highest function value, place the new vertex halfway between $\vec{x}_r$ and $\vec{c}$ instead.

6. If the new vertex from step 5 is better than both $\vec{x}_h$ and $\vec{x}_r$, contraction was successful. Replace $\vec{x}_h$ with the new point. Otherwise, *shrink* the entire simplex by moving *all* vertices halfway towards $\vec{x}_l$. Return to step 2.

This procedure can be slightly generalized by introducing scaling factors e.g. at the reflection or contraction steps. The above description corresponds to the most common settings. The algorithm usually halts when the objective function no longer changes significantly over the simplex points, but a termination condition based on simplex size can also be used (and will be below).

NMS has the advantages of being rather robust to noisy functions and performs well for small n ($\lesssim 5$). However, it quickly becomes inefficient for very large n and is badly suited for searches including constraints. Convergence may fail completely when the simplex collapses into a subspace [22].

As for most direct search methods, little theory exists describing the convergence properties of NMS. The popularity of NMS is founded on its success in practice.

Subplex

Dissatisfied with the poor performance of NMS for large n, T. Rowan developed an improved algorithm in his PhD thesis [22]. Subplex[9] is short for subspace-searching simplex. The algorithm breaks down the search space into low-dimensional subspaces which can then be searched by NMS. This trick can vastly speed up the calculation compared to NMS, but it risks neglecting subspaces with even lower minima. As another advantage, the memory requirements of Subplex are $\mathcal{O}(n)$ instead of the $\mathcal{O}(n^2)$ of NMS[10].

For each iteration, Subplex divides the search space based on the so-called vector of progress, that is the change in $\vec{x}_l$ during the last step. The subspaces are chosen such that the vector of progress lies approximately in the first subspace; here the minimum is suspected. Further subspaces are generated by other elements of the vector of progress, grouped together by their order of magnitude. All subspaces are then consecutively searched by NMS, which halts when the simplex size has been reduced by a predefined parameter[11]. Subplex uses the new minimum found by NMS to define the new vector of progress, update the subspaces and adapt the step sizes. Although somewhat heuristic, Subplex has shown to work well in practice and often even better than NMS [22, 13].

[9] The author preferred the capitalization SUBPLEX in his thesis. This is be abandoned here for readability.

[10] This is in fact not crucial for any of the applications in this thesis, where n never exceeds 10. The computational cost is dominated by the function calls (i.e. propagations with MCTDH), not by the search algorithm.

[11] $\frac{1}{10}$ was Rowan's standard setting. Smaller values increase speed even further, but makes missing a better minimum more likely. Higher values improve search quality while slowing Subplex down.

Rowan wrote his original code in Fortran. This thesis uses S.G. Johnson's implementation of Subplex in C contained in the NLopt optimization library [13]. NLopt provides an interface for simple integration with various programming languages; it also contains an implementation of NMS used here.

4 Calculations

This chapter describes the calculations performed with MCTDH[1], it is divided into three sections. Section 4.1 contains basic exercises with a Harmonic oscillator, mainly to test the functions and settings of MCTDH. A reader already familiar with the software may skip this part. In section 4.2 a more realistic system is investigated, the one-dimensional Morse oscillator. This serves as a simple, but qualitatively sufficient model of a diatomic molecule. The potential parameters are taken from a paper by M. V. Korolkov et al. [15] whose results shall be reproduced. Finally, section 4.3 investigates this thesis' central issue, the value of MCTDH for optimal control problems. Here, the built-in optimization tool `optcntrl` is compared to a Fourier-expanded pulse as in equation (3.29) either with or without a randomized basis (CRAB). The two systems under study are the Morse oscillator just described and the LiCs diatomic with an experimentally determined potential.

Before starting any calculations in MCTDH, a number of simulation parameters have to be set. The most important are listed below. MCTDH reads all these parameters from two (or more) text files. All physical properties of the system are written into the `operator` file. This includes the Hamiltonian and all physical constants, and possibly further operators which may be used. All computational parameters and settings are given via the `input` file, with the most important ones listed below.

- The *discrete variable representation* (DVR) has to be chosen. Whenever a real-valued function is represented on a finite-size computer, a DVR is required [3]. It can be represented in a position space basis by storing the function values at the grid points. Depending on the type of function, an expansion in a function basis is often more efficient. For example, the wavefunction of an oscillating system can be expanded in Harmonic oscillator eigenfunctions. Both the type and the size (i.e. the number of grid points or basis functions) of the DVR are decisive for the efficiency and accuracy of a calculation.

- The number of *SPFs* must be defined. In multi-dimensional systems, it is crucial to include the configurations with strong interactions and to skip those with negligible correlation. In the one-dimensional case here, this step is moot. There is only one variable and hence one SPF.

- The numerical *integrator* actually solves the MCTDH working equations (3.24). MCTDH offers a number of algorithms, including the Bulirsch-Stoer (BS) integrator and the Short

[1] The software package, not the algorithm.

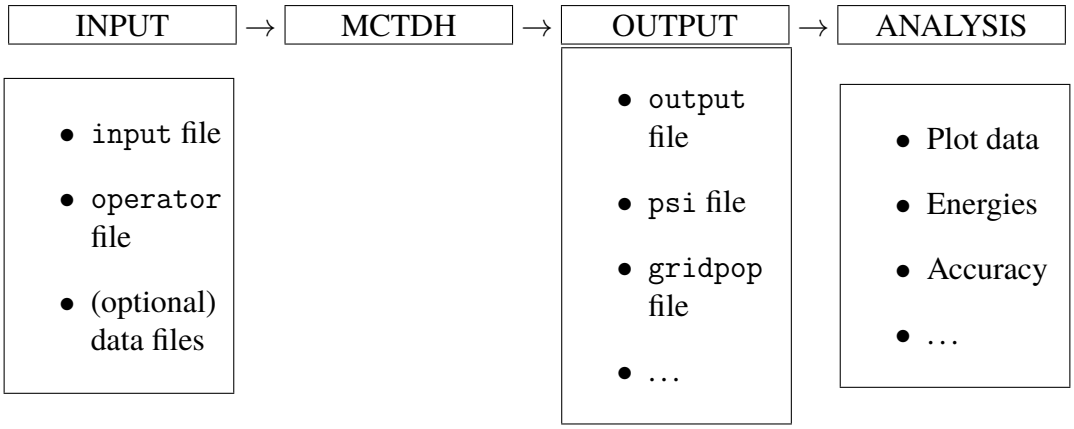

Figure 4.1: Workflow with MCTDH, from left to right: All parameters and settings are defined in the operator and input files. Additional data files can provide e.g. PES data or the initial wavefunction. During the calculation, the program writes the desired output files, which can then be plotted and analysed with included tools or external scripts. There are also tools to check the accuracy and efficiency of the calculation.

Iterated Lanczos (SIL) algorithm. Depending on the chosen method, some more parameters may be set. For most cases, the default settings (BS for propagating the SPFs, SIL for the A-vector) produce reliable results.

- The initial wavefunction has to be set. There are several ways to do this, such as defining it as the eigenfunction of a given operator, by using a number of predefined functions (e.g. HO eigenstates), reading a numerical file or using the result of a previous calculation.

- The input file also specifies to what extent MCTDH shall save the *output* of its calculations. For example, the full wavefunction is often interesting, but may become prohibitively large to store. In such cases, it may suffice to save just the grid populations or the autocorrelation file. In total, MCTDH can write up to ~ 20 different output files, and it would be wasteful to save everything indifferently.

While a well-written operator file can be reused many times for the same system, the input file is usually adapted slightly to the aim of the current calculation. The workflow of an MCTDH calculation is sketched in figure 4.1.

4.1 Harmonic Oscillator

The quantum harmonic oscillator (HO) in one dimension is defined by the Hamiltonian

$$\hat{H} = -\frac{1}{2m}\frac{\partial^2}{\partial x^2} + \frac{1}{2}m\omega^2 x^2 \tag{4.1}$$

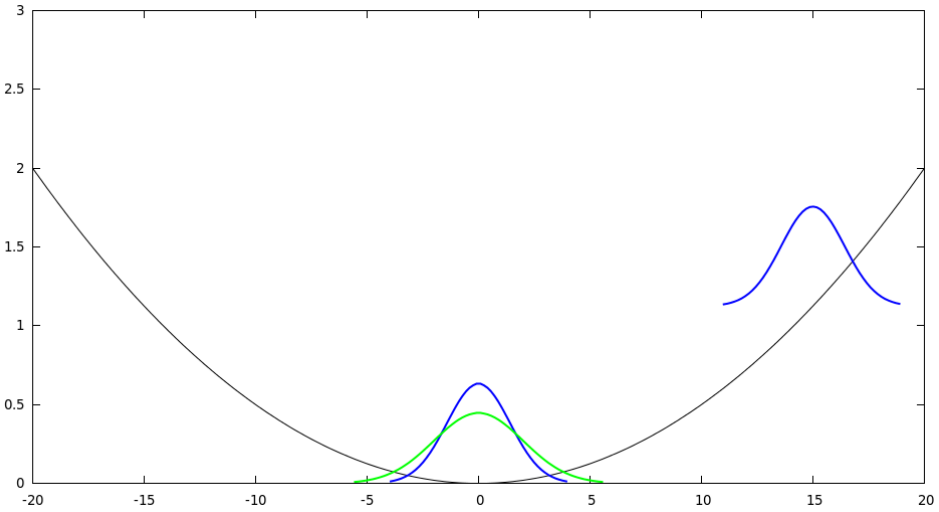

Figure 4.2: Typical initial wavefunctions for the HO calculations. Black (thin) curve: harmonic potential. Blue bell curves: Ground state (centralized) and coherent state (displaced). Green (wide) bell curve: Squeezed coherent state.

with the frequency ω and mass m. Its eigenenergies are the equidistant levels $E_n = \omega(n + \frac{1}{2})$, $n = 0, 1, \ldots$ and its eigenstates are the known functions

$$\psi_n(x) = N_n \cdot e^{-\frac{m\omega}{2}x^2} \cdot H_n(\sqrt{m\omega}x) \tag{4.2}$$

with a normalization constant N_n to ensure $\int |\psi_n(x)|^2 \mathrm{d}x = 1$ and the Hermite polynomials[2] $H_n(x)$ [8].

This system is extremely well-studied and allows for an analytical solution in many cases. Therefore it is ideal for testing purposes, since one usually knows what to expect.

4.1.1 Propagation

The main purpose of MCTDH is the propagation of wavefunctions. Different initial wavefunctions were chosen and propagated in the potential with $m = 1.0$ and $\omega = 0.015198$. This corresponds to an oscillator period of 10 fs and an energy of 0.4136 eV. As a DVR, HO eigenfunctions are used with a grid size of 24. The initial wavefunctions include (see also figure 4.2):

- HO eigenfunctions. These should stay in the respective eigenstate and show no evolution (except for an irrelevant phase).
- Displaced ground state wavefunction, also known as a *coherent state*. This is a Gaussian function with the same width as the ground state, but centre at some $x_0 \neq 0$. It should

[2]The Hermite polynomials are defined by $H_n(x) = (-1)^n \exp(x^2) \frac{\mathrm{d}^n}{\mathrm{d}x^n}(\exp(-x^2))$. The first few functions are $H_0(x) = 1, H_1(x) = 2x, H_2(x) = 4x^2 - 2, \ldots$

show a classic oscillatory motion around zero while keeping its shape. The same holds for coherent states with an initial momentum.

- Gaussian with an arbitrary width centred around zero. This is called a *squeezed coherent state*. It should show a breathing motion, i.e. a periodic change in width. Any Gaussian wavefunction can be seen as the ground state of a HO with a specific frequency. In this case, this frequency is $\Omega = 0.01976$, yielding a narrower curve than the ground state of the actual potential.

4.1.2 Relaxation

Relaxation is a technique for finding the ground state wavefunction of a given Hamiltonian by propagating the initial wavefunction in negative imaginary time. For large $t > 0$, the wavefunction $\Psi(\tau) \equiv \Psi(-it)$ converges to the ground state [20].

This calculation is performed with two-dimensional isotropic HO with $m = 1$ and $\omega_x = \omega_y = 8.0$, the initial wavefunction is picked somewhat arbitrarily as a two-dimensional Gaussian centred around $(x, y) = (0.6, -0.4)$ with width $(\Delta x, \Delta y) = (2.08, 1.18)$, although the relaxation should converge to the same result for any reasonable input. The result is judged by the final energy which should be $E_0 = \frac{1}{2}(\omega_x + \omega_y) = 8.0 = 217.69108\,\text{eV}$. When the accuracy is unsatisfactory, the primitive basis or integrator settings can be adjusted.

4.1.3 Coupling to a field

The Hamiltonian including field interaction reads

$$\hat{H} = -\frac{1}{2m}\frac{\partial^2}{\partial x^2} + \frac{1}{2}m\omega^2 x^2 - \mu_0 \cdot x \cdot E(t) \tag{4.3}$$

with the dipole moment set to $\mu_0 = 1.0$. The initial wavefunction (ground state or first and second excited states) is propagated with the field $E(t)$ chosen to be

- a resonant monochromatic field $E_0 \cdot \cos(\omega t)$ with ω being the oscillator frequency and the amplitude E_0 ranging up to 0.15.

- an off-resonant monochromatic field $E_0 \cdot \cos(\omega_L t)$ with $\omega_L \neq \omega$ and comparable amplitude.

- laser pulses $E_0 \cdot f(t)\cos(\omega_L t)$ with the envelope function $f(t) = \cosh^{-2}(\frac{t-\Delta}{b})$. Here $\Delta = 4\,\text{fs}$ sets the centre of the pulse; the width parameter b as well as the frequency ω_L are varied. Some examples are depicted in figure 4.3.

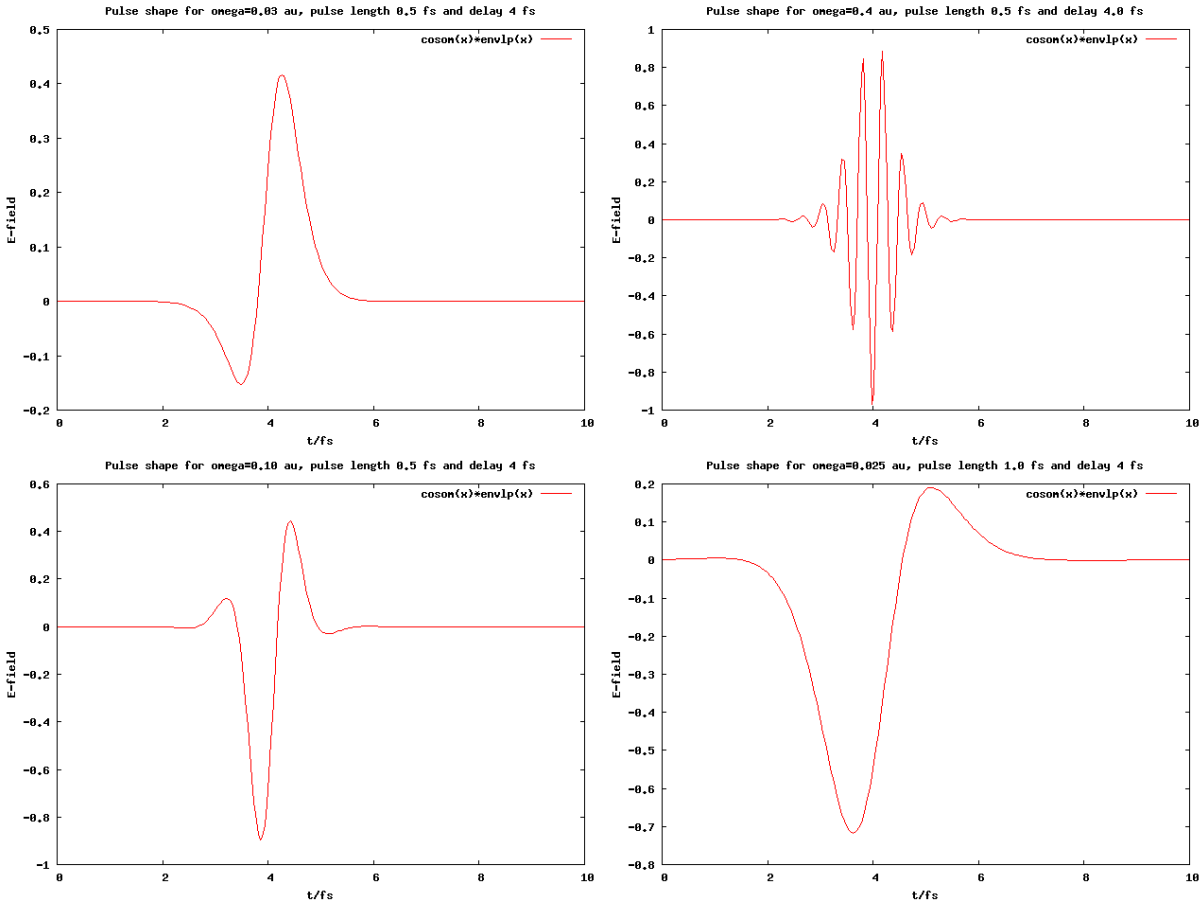

Figure 4.3: Four sample pulses used to excite the Harmonic oscillator.

4.2 Morse Oscillator

Not only is the Harmonic Oscillator unfit to model a diatomic molecule, it also shows limited dynamics. An interaction as in equation (4.3) can only excite the HO to coherent states [9], never to a single eigenstate $|n\rangle$. In order to study selective excitation, a non-harmonic system has to be chosen such as the one-dimensional Morse oscillator introduced in section 2.2. Here the parameters of the potential (2.13) are the depth $D = 0.1994$, equilibrium distance $r_0 = 1.821$ and the width parameter $\beta = 1.189$. These values are taken from [15], where this system is studied in detail. It models the OH bond in water, so the reduced mass is $m = (m_H m_O)/(m_H + m_O) = 1728.539$. The harmonic frequency (the frequency of the harmonic approximation near r_0) is $\omega = \beta\sqrt{2D/m} = 0.01806$.[3] There are exactly 22 vibrational eigenstates from $|0\rangle$ to $|21\rangle$.

The authors of [15] used three consecutive IR pulses to excite the bond from the ground state to $|15\rangle$, which is close to the dissociation threshold. The goal of this section is to reproduce their result, taking one step at a time. The first step is to set up a suitable DVR and check the accuracy of MCTDH. Then, population transfer between $|0\rangle$ and $|1\rangle$ via Rabi oscillations can be attempted. Having achieved that, the IR pulses from [15] can be modelled to excite the system first to $|5\rangle$, then to $|10\rangle$ and finally to $|15\rangle$.

4.2.1 Choice of DVR

Although the lower vibrational states can be expanded quite well in terms of HO eigenfunctions, such a DVR fails for the higher eigenstates. As was mentioned before, only the low eigenstates are sufficiently localized. States close to dissociation can have significant values far away from r_0 and have more resemblance to plane waves. Therefore a sine DVR is a better suited for the dissociative modes. MCTDH implements such a primitive basis with the basis functions

$$\chi_j(x) = \sqrt{\frac{2}{L}} \cdot \sin\left(\frac{x - x_0}{L}\pi j\right) \cdot \mathbf{1}_{[x_0, x_{N+1}]}(x), \quad j = 1, 2, \ldots \tag{4.4}$$

where $\mathbf{1}_{[x_0,x_{N+1}]}$ is the indicator function of the interval $[x_0, x_{N+1}]$ (i.e. it is one inside including the boundaries and zero outside). These are the eigenfunctions of a particle in a box with length $L = x_{N+1} - x_0$. By choosing the number N of basis functions, the user divides the interval into N equidistant grid points x_1 to x_N [20].

Based upon the results of the next section (4.2.2), a sine DVR with $x_1 = 0.7, x_N = 8.0, N = 96$ is chosen for most calculations. The grid boundaries can be explained when considering the value of the potential at these points: $V(0.7) = +7.05$ is high enough to prevent the wavefunction from penetrating any further to the left. Smaller x_1 turned out to lead to numerical problems, presumably because the energy range becomes too large for floating point accuracy. Similarly, even the highest bound state has negligible probability density beyond of $x = 8.0$,

[3] In more common units, $D = 5.43\,\text{eV}$, $r_0 = 0.96\,\text{Å}$, $\beta = 0.63\,\text{Å}^{-1}$, $m = 1.055\,\text{AMU}$ and $\hbar\omega = 0.491\,\text{eV} = 3963.7\,\text{cm}^{-1}$.

because $V(8.0) = -0.000049$ is still considerably larger than $E_{21} = -0.00377$. Higher x_N is again impractical since a very large basis size would be required to keep the spatial grid fine enough.

Fewer basis functions than 96 are usually enough, in fact N can be reduced to 64 without loss of accuracy for all but the very last excitation step (last paragraph of section 4.2.3). However 96 is used for all OCT simulations to be on the safe side and because the calculations are still reasonably fast.

4.2.2 Diagonalization

MCTDH includes a feature to diagonalize an arbitrary hermitian operator with the Lanczos algorithm [3]. This is applied to the Morse oscillator with the parameters specified above (4.2) to find the eigenenergies. Since these are known exactly by equation (2.14), this can serve as a benchmark for the DVR. Instead of a final propagation time, this type of calculation asks the user for the number of iterations, typically about 10^3 to 10^4 for small systems. In this case, 5000 steps are chosen, as higher numbers show no improvement in the results.

The diagonalization is performed for two types of primitive basis sets: A sine DVR with the end points 0.7 and 8.0, and a HO DVR centred around $r_0 = 1.821$ with the mass and frequency corresponding to the Morse potential. In both cases the grid size is varied until satisfactory agreement with the exact eigenvalues is achieved.

4.2.3 State selective excitation

Having found a reliable representation of the model system, coupling to a light field can be studied. Interaction with a time-dependent field $E(t)$ is added to the Hamiltonian, resulting in

$$\hat{H} = -\frac{1}{2m}\frac{\partial^2}{\partial r^2} + V(r) - \mu(r) \cdot E(r) \tag{4.5}$$

with the Morse potential $V(r)$. The dipole moment is non-trivial in this system, as it depends on the internuclear distance. It is modelled by the Mecke function introduced in equation (2.21) with the parameters $R^* = 0.6\,\text{Å} = 1.134$, $\mu_0 = 7.85\,\text{D/Å} = 1.634$ [15].

Population analysis

Before turning to population control, a few words on how the populations of the desired eigenstates are measured. Unfortunately MCTDH offers no tool to directly do this, so population analysis is performed with a self-written Python script. MCTDH does give (when asked) the primitive basis population, i.e. the contribution of every single basis function to the wavefunc-

tion. Given a fixed basis χ_j of size N, the basis population of each eigenstate ϕ_i was collected:

$$\phi_i = \sum_{j=1}^{N} u_{ij}\chi_j \tag{4.6}$$

Once the matrix $U = (u_{ij})$ is stored, the eigenstate population of any wavefunction Ψ can be found by means of a simple basis transformation. Again, Ψ is first expanded in the primitive basis and the coefficients are collected:

$$\Psi = \sum_{j=1}^{N} a_j\chi_j \tag{4.7}$$

$$\Psi = \sum_{i=0}^{21} b_i\phi_i \tag{4.8}$$

$$\text{with} \qquad b_i = \langle\phi_i|\Psi\rangle = \sum_{j=1}^{N} u_{ij}^* a_j \tag{4.9}$$

The squared coefficients $|b_i|^2$ give the population p_i of the eigenstate ϕ_i. Here it is assumed that exactly 22 bound states exist, but of course the above formula is fully generalizable. This calculation is exact and very fast, but it has the major drawback of working only for one specific combination of primitive basis and eigenstates. As soon as the Hamiltonian or the DVR change, U has to be recomputed. The script also becomes useless if Ψ has significant contributions from continuum states, when sums have to be replaced with integrals or, even worse, a combination of both.

Rabi oscillations

The excitation energy from the ground state to the first excited state is $E_1 - E_0 = 0.0172 = 3784.2\,\mathrm{cm}^{-1}$. Due to the anharmonicity of the system, the excitation to the next state already shows a considerable detuning with $E_2 - E_1 = 0.0164 = 3604.7\,\mathrm{cm}^{-1}$. This is large enough to make the $|1\rangle \to |2\rangle$ transition rate negligible when exciting the first state resonantly. As a result the Morse oscillator can effectively be treated as a two-level system for sufficiently long pulses and small amplitudes[4].

As the first few states are sufficiently localized ($\Delta r = 0.225$ in state $|1\rangle$), the Mecke function can be linearised as in equation (2.22), yielding a dipole gradient of $\mu' = 0.299$ and a transition matrix element $\mu_{01} = \mu'\langle 0|\hat{r}|1\rangle = 0.02544$[5].

[4] The approximation breaks down for very short ($\lesssim 100$ fs) pulses because those have a larger bandwidth. For high amplitudes ($E_0 \gtrsim 0.1 \approx 50$ MV/m) the field can no longer be treated perturbationally.

[5] There is actually no need to linearise the dipole operator since the integral $\mu_{01} = \langle 0|\hat{\mu}(r)|1\rangle$ can easily be evaluated numerically. The way given in the text is appealing because the matrix elements of the position operator are known analytically [6], e.g. $\beta\langle 0|\hat{r}|1\rangle = \frac{\sqrt{2(N-1)}}{2N-1}$ with $N = \frac{\sqrt{2mD}}{\beta} - \frac{1}{2}$.

This results in a Rabi frequency of $\Omega = \mu_{01} \cdot E_0$ and an oscillation period of

$$T_{\mathrm{Rabi}} = \frac{2\pi}{\Omega} = 5.9746\,\mathrm{fs} \cdot E_0^{-1}$$

with E_0 given in atomic units (e.g. $T \approx 1000\,\mathrm{fs}$ for $E_0 = 0.006 \approx 3\,\mathrm{MV/m}$).

The system is excited with monochromatic laser light of constant amplitude $E_0 = 3.07\,\mathrm{MV/m}$ and the resonant frequency $\omega_L = E_1 - E_0 = 3784.2\,\mathrm{cm}^{-1}$.

The oscillations under a slight detuning of the laser frequency $\omega_L = E_1 - E_0 \pm \Delta$ are examined, too. The maximum population of $|1\rangle$ should then be given by $\frac{\Omega^2}{\Omega^2+\Delta^2}$.

Subsequently, Gaussian pulses of varying length are used. Complete population transfer is attempted with $\pi-$pulses as well as 50% population by using a $\pi/2-$pulse. The field thus takes the form

$$E(t) = \frac{N \cdot E_0}{\sqrt{2\pi(\Delta t)^2}} e^{-\frac{1}{2}\left(\frac{t-t_p}{\Delta t}\right)^2} \cdot \cos(\omega_L t) \tag{4.10}$$

where typical values for the centre and width of the pulse are $\Delta t \sim 100\,\mathrm{fs}$ and $t_p \sim 4\Delta t$, respectively. The amplitude E_0 can be left unchanged (compared to the constant amplitude simulations) as long as the normalization constant N is chosen such that the area theorem is fulfilled, i.e. $\int \Omega(t)\mathrm{d}t = \pi \iff N = T_{\mathrm{Rabi}}/2$ for a π-pulse.

This simulation is repeated with a sequence of two Gaussian pulses, the second one having a laser frequency of $\omega_L = 3604.7\,\mathrm{cm}^{-1}$ to populate the second excited state. The respective amplitudes are $N_1 E_0 = 123.5$ (unchanged) and $N_2 E_0 = 0.699 N_1 E_0$ due to the higher transition dipole moment $\mu_{21} = \mu_{10}/0.699$.

$|0\rangle$ to $|5\rangle$ to $|10\rangle$ excitation

Once the most basic example of population transfer has been mastered, interest returns to the results in [15]. In this reference, the model system is excited from the ground state to the fifth excited state by multi-photon absorption in a monochromatic sinusoidal pulse. The electric field is given by

$$E(t) = E_1 \cdot \sin^2\left(\frac{\pi t}{T}\right) \cdot \cos(\omega_1 t) \tag{4.11}$$

with the amplitude $E_1 = 328.05\,\mathrm{MV/m}$, the laser frequency $\omega_1 = 3424.2\,\mathrm{cm}^{-1}$ and the pulse length $T = 1\,\mathrm{ps}$. This transfers the system into the $|5\rangle$ state.

After $1\,\mathrm{ps}$ another pulse with the same shape sets in to excite the bond further to the $|10\rangle$ state. Its parameters are $E_2 = 214.56\,\mathrm{MV/m}$, $\omega_2 = 2524.7\,\mathrm{cm}^{-1}$ and identical pulse length of $1\,\mathrm{ps}$. Note that longer wavelengths are required for high quantum numbers because the neighbouring states lie closer.

The authors of [15] report a selective excitation of close to 100% with these pulses. In this

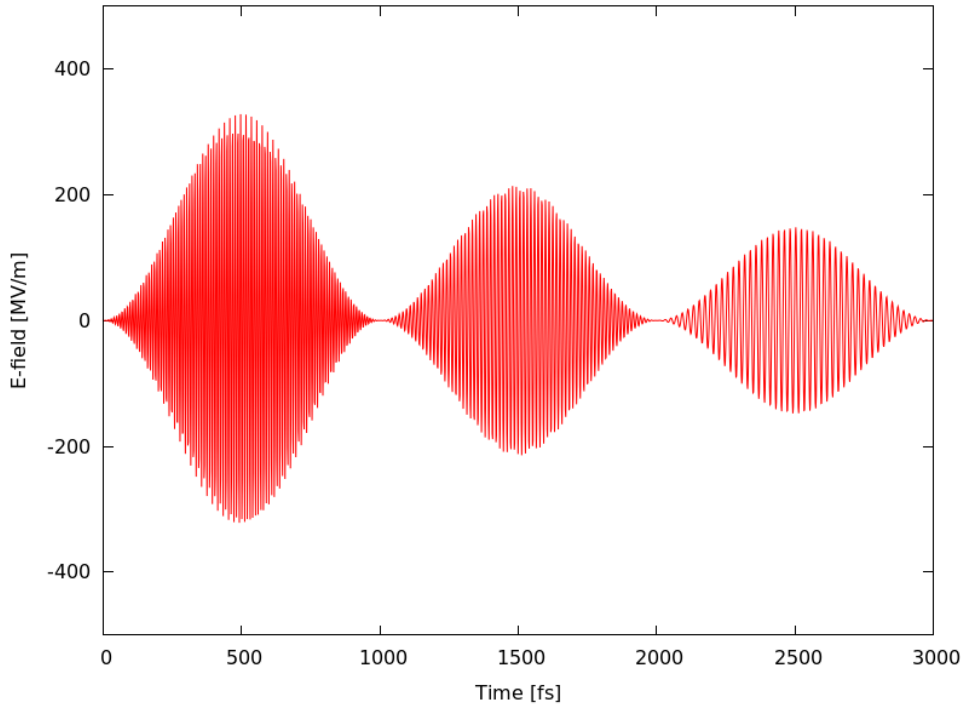

Figure 4.4: Laser pulses for excitation of the Morse oscillator to $|15\rangle$, adopted from [15]. The $\sin^2$ shape of the pulses is clearly visible.

thesis, their pulse parameters are used in an attempt to achieve the same.

$|10\rangle$ to $|15\rangle$ excitation

Another multi-photon absorption process can drive the system from $|10\rangle$ to the target state $|15\rangle$. A final 1 ps-pulse with the parameters $E_3 = 148.07\,\text{MV/m}$ and $\omega_3 = 1625.7\,\text{cm}^{-1}$ is used for this purpose. The full pulse train is depicted in figure 4.4.

Compared to the previous cases there is a number of differences: With an energy of $E_{15} = -0.482\,\text{eV}$ the target state lies close to the dissociation threshold and couples significantly to the continuum states. Therefore a complete occupation is not achieved in [15], but instead a dissociation probability of 6.9% is reported. However the *state selectivity*, defined as the ratio of population in $|15\rangle$ and the population of all bound states combined, is as high as 99.23%. Another important factor is the spatial spread of the wavefunction. It turns out that a measurable population of the grid border occurs, which must be handled with a CAP as described further below.

Finally, the authors of [15] reduced the length of the pulse train. For this purpose, the first and the second pulses were shortened to 500 fs each. In addition, the pulses were overlapped with the second pulse setting in at $t = 350\,\text{fs}$ and the third pulses at $t = 600\,\text{fs}$. The frequencies and amplitudes were adjusted to: $\omega_1 = 3425.8\,\text{cm}^{-1}$, $\omega_2 = 2425.7\,\text{cm}^{-1}$, $\omega_3 = 8148.6\,\text{cm}^{-1}$, $E_1 = 400.75\,\text{MV/m}$, $E_2 = 214.56\,\text{MV/m}$, $E_3 = 426.47\,\text{MV/m}$.

The resulting field is depicted in figure 4.5. Note that ω_1 and ω_2 are almost unchanged while

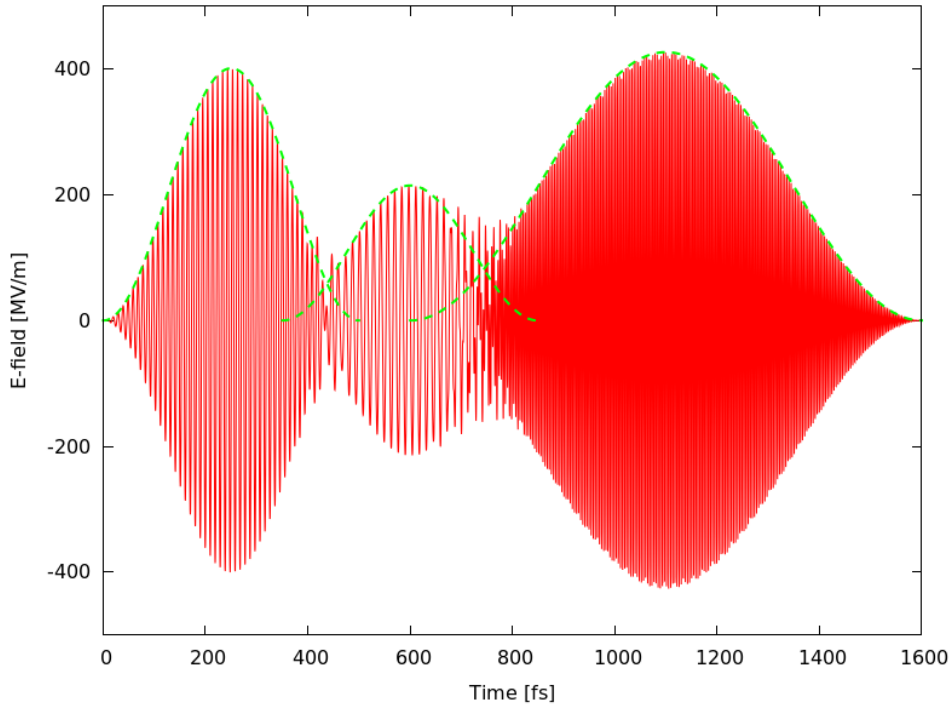

Figure 4.5: Shortened pulse train for excitation of the Morse oscillator to $|15\rangle$, again adopted from [15]. The individual pulse envelopes are indicated.

ω_3 is much higher than before. The motivation behind this is to accomplish the excitation from $|10\rangle$ to $|15\rangle$ with a single overtone transition instead of a 5-photon-absorption like before. This reduces the coupling to the continuum states and hence the dissociation probability to about 4.1%.

When the wavefunction hits the border of the grid, an non-physical reflection of the wavefunction at the last grid point occurs, dramatically affecting the accuracy of the calculations. This is a common problem when working with dissociative modes on a finite grid, and the technique of *Complex Absorbing Potentials* (CAPs) is an established workaround [20]. Near the border of the grid, a negative imaginary potential term

$$V_{\mathrm{CAP}}(r) = -i\eta \cdot (r - r_c)^2 \cdot \Theta(r - r_c) \tag{4.12}$$

is added to the Hamiltonian. Here $\Theta(r)$ is the Heaviside step function, so the potential is only non-zero to the right of a critical value r_c. The parameter η controls the strength of the potential, and other exponents than 2.0 may be used on the second factor.

This potential absorbs a wavefunction propagating beyond x_c. Now the norm is no longer conserved, but this is the lesser evil compared to a reflected wavepacket. After all, the dissociated part of the wavefunction is rather small[6] and only contributes to the continuum states, which shall not be studied here.

[6] Anticipating the next chapter, it turns out that the final norm for the calculations performed here is 97.9%, so a little over 2% of the population is lost.

The one-photon excitation is calculated first without a CAP, then with CAP using the parameters $\eta = 0.25$, $r_c = 6.0$. This strength parameter is quite typical according to the examples in the MCTDH handbook [25], and the value of r_c was chosen with the grid populations in view and to allow a moderately strong CAP at the grid end point ($V_{\mathrm{CAP}}(8.0) = -1.0 \cdot i$).

For each type of calculation, the total population of $|15\rangle$ and the state selectivity are computed and compared with the reference.

4.3 Optimal Control

Having reproduced previous results with known pulse parameters, attention turns to optimal control with CRAB. The Morse oscillator from section 4.2 remains the relevant system, but the control target is set in a slightly different manner.

4.3.1 One- and two-parameter control

As a preliminary proof of concept, optimization is performed with the amplitude E_0 as the only free parameter. The target is maximal population transfer from the ground state to $|1\rangle$ via resonant absorption. The field is given by the pulse

$$E(t) = E_0 \cdot \sin^2\left(\frac{\pi t}{T}\right) \cos(\omega_L t) \tag{4.13}$$

with the fixed frequency $\omega_L = 0.01724 = 3784.2\,\mathrm{cm}^{-1}$ and length $T = 1000\,\mathrm{fs}$. Since the energy content of the field is proportional to E_0^2, a simplified penalty function is chosen. The full cost functional reads

$$J = 1 - \langle|\Psi(T)|1\rangle|^2 + \alpha E_0^2 \tag{4.14}$$

with penalty factors chosen in the range from 0 to a 250. Now the functional is considered a function $J = f(E_0)$ of one variable. A minimum of f with respect to E_0 is searched for various starting values of E_0.

The same process is repeated for variable ω_L while keeping E_0 fixed. Eventually, an optimization for both parameters simultaneously is performed.

The Python library `scipy.optimize` [14] contains a number of different optimization algorithms, most of which are tested. This includes the Nelder-Mead (NMS) method described in section 3.3, but also the modified Powell's method, the conjugate gradient (CG) method and the Broydon-Fletcher-Goldfarb-Shanno (BFGS) algorithm[7]. The latter two require knowledge of the gradient of f, which they estimate numerically by comparing the function values at two very close points.

[7] For all subsequent calculations either NMS or Subplex are used, therefore no explanation of the other algorithms is deemed necessary here. For details see the SciPy documentation [14] and the references therein.

4.3.2 CRAB with ten parameters

Next a multivariate cost function is optimized using crab.

To avoid the complications near the dissociation threshold, $|5\rangle$ is declared the target state (starting from the ground state again), and the control time is set to $T = 1000\,\mathrm{fs}$. This is a very modest goal compared to the above results, but after all this is CRAB's first real benchmark in combination with MCTDH, and it seems sensible to give the algorithm a goal which is known to be doable.

The electric field is expanded in a Fourier basis as in equation (3.29) with $N_c = 5$, so a total of 10 parameters is optimized. The initial guess is given by a $\sin^2$ shaped pulse with $\omega^{\mathrm{guess}} = 0.0156 = 3424\,\mathrm{cm}^{-1}$, $E_0^{\mathrm{guess}} = 0.036 = 18.4\,\mathrm{MV/m}$. The photon energy is exactly $\frac{1}{5}(E_5 - E_0)$, so this frequency can lead to multi-photon excitation just as in section 4.2.3. The amplitude is lower here, so this pulse yields a target population of about 2%. As an envelope function, $\Lambda(t) = \sin^2\left(\frac{\pi t}{T}\right)$ is used. The penalty term is $\alpha \int_E (t)^2 \mathrm{d}t$ with $\alpha = 10^{-5}$. This small penalty factor helps avoid large field amplitudes while still making sure the cost functional is dominated by the target population.

The choice of the frequencies ω_k is paramount. A natural choice would be to use the transition energies $\omega_k^{\mathrm{eigen}} = E_k - E_{k-1}$. Another reasonable choice are the harmonic frequencies $\omega_k^{\mathrm{harm}} = \frac{2\pi}{T}k$. At the heart of CRAB lies the idea not to use the exact frequencies, but to randomize them by multiplication with a random factor:

$$\tilde{\omega}_k = \omega_k \cdot \left(\frac{1}{2} + r_k\right) \tag{4.15}$$

with r_k taken from a uniform random distribution on the the interval $[0, 1]$ [5]. To avoid skewed results by a particularly (un)fortunate choice of random numbers, this process is performed three times on the resonant and the harmonic frequencies. Finally, two sets of completely random frequencies are generated from a uniform distribution on $[0, 0.2]$ (since $E_0 \approx -0.2$). All the frequencies tested are summarized in table 4.1.

The results of section 5.3.2 will suggest that NMS is the most suitable algorithm within `scipy.optimize`. As this library does not contain an implementation of Subplex, the C library NLopt [13] is used. Amongst others, NLopt implements Subplex and also NMS, giving an opportunity to compare the two implementations of NMS. All three algorithms (NMS from scipy, NMS from NLopt and Subplex from NLopt) are tested with each set of frequencies. The calculations are limited to 200 function calls each, with each call (MCTDH run) taking about 3 seconds on a Linux server with about 3 GHz[8]

The penalty function is $\alpha \int_0^T E(t)^2 \mathrm{d}t$, but with a fairly small penalty factor of $\alpha = 10^{-5}$. The cost function is dominated by the target state population $p_5 = |\langle \Psi(t)|5\rangle|^2$, which is also the quantity of interest in the analysis.

[8] Most calculations were performed on DESY's PAL cluster. The PAL servers have 2.4 to 3.0 GHz CPUs; the latter was used in most cases.

Description	Abbr.	ω_1	ω_2	ω_3	ω_4	ω_5
Exact resonant frequencies	`eig`	0.017242	0.016425	0.015607	0.014789	0.013971
Randomized res. freq. 1	`eig-rn1`	0.015714	0.017487	0.021671	0.017012	0.019498
Randomized res. freq. 2	`eig-rn2`	0.025242	0.018605	0.021464	0.012774	0.020827
Randomized res. freq. 3	`eig-rn3`	0.025472	0.014188	0.021326	0.014171	0.085043
Exact harmonic frequencies	`harm`	0.000152	0.000304	0.000456	0.000608	0.000760
Randomized harm. freq. 1	`harm-rn1`	0.000104	0.000203	0.000454	0.000767	0.000563
Randomized harm. freq. 2	`harm-rn2`	0.000181	0.000430	0.000509	0.000736	0.000563
Randomized harm. freq. 3	`harm-rn3`	0.000089	0.000217	0.000294	0.000694	0.000543
Random frequencies 1	`rand1`	0.199047	0.083381	0.038444	0.002658	0.051437
Random frequencies 2	`rand2`	0.092450	0.186849	0.094596	0.168496	0.110986

Table 4.1: The frequencies used for ten-parameter control. The second column introduces a shorthand which will later be used.

4.3.3 Frequency optimization

Based on the advice of Dr. Antonio Negretti, the above algorithm is modified to also optimize the frequencies. To keep the number of parameters approximately constant, the basis size is reduced to $N_c = 3$, turning the cost functional into a function of nine variables $(a_k, b_k, \omega_k), i = 1, 2, 3$. The starting values for ω_k are the first thee harmonic frequencies from table 4.1, while the initial field guess is again a sinusoidal pulse which results in a target population of 2%.

The Subplex and the NMS method (both from NLopt) are compared. Hope is that modulation with the optimized frequencies yields better pulses than the fixed frequencies.

4.3.4 LiCs diatomic

The LiCs diatomic is an heteronuclear alkali molecule which has recently garnered interest both theoretically and experimentally, mostly in the field of low temperature physics [2, 24]. It is formed by non-elastic collisions in a mixture of ultracold (< 1 mK) Li and Cs vapour, but can also be synthesized in a heat pipe at temperatures of a few hundred °C for spectroscopic studies. This was done by P. Staanum et al. [24], who determined the ro-vibrational spectrum of the LiCs ground state. The potential energy curve shown in figure 4.6, together with the electric dipole moment $\mu(R)$ calculated by M. Aymar and O. Dulieu with *ab initio* methods [2]. Like similar alkali dimers LiCs has a large dipole moment.

The potential energy function has some resemblance to a Morse potential, as had already been illustrated in figure 2.2. The major difference lies in the long-range behaviour, where the LiCs potential approaches zero proportional to $-1/R^6$ (just like most diatomics [8]). The molecule's dissociation energy has been determined experimentally to be 0.728 eV, while theoretical predictions suggest 0.743 eV. The experimentally found potential supports 55 bound vibrational states for a non-rotating molecule [24].

This system is modelled on a sine DVR with basis size 96 with the inter-nuclear distance

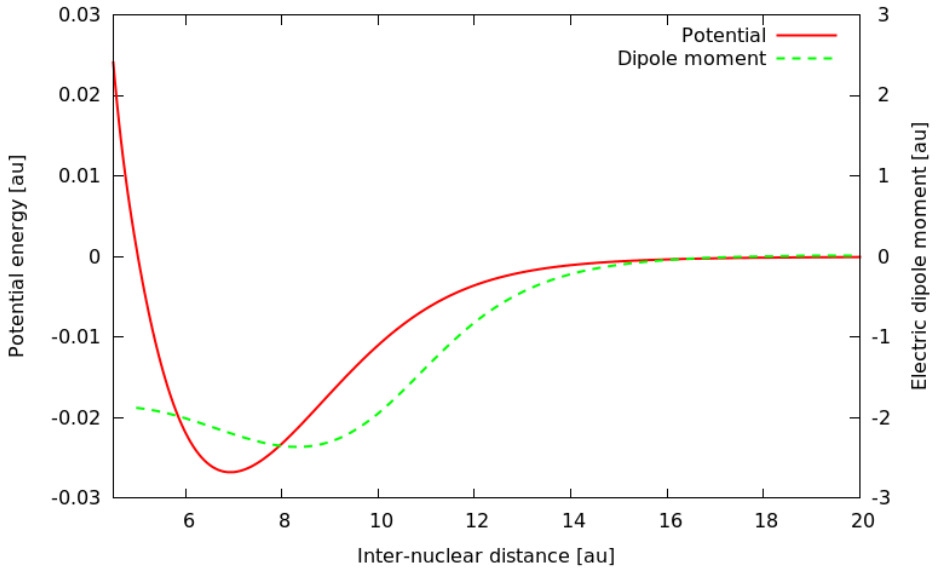

Figure 4.6: Potential energy surface and electric dipole moment of the LiCs diatomic. Data from [24, 2], kindly provided by Dr. Peter Schmelcher.

ranging from 5.0 to 20.0. At $x = 18.0$, a CAP with the strength parameter $\eta = 0.25$ sets in to avoid possible reflections of the wavepacket with the grid edge.

In order to probe state selective control with short pulses, the control time is set to $T = 250\,\mathrm{fs}$. The target state is $|1\rangle$ with an energy difference of $E_1 - E_0 = 22.7\,\mathrm{meV} = 183\,\mathrm{cm}^{-1}$. The excitation of the target state is attempted via resonant one-photon absorption, hence an initial pulse with $\omega_L = 183\,\mathrm{cm}^{-1}$ is used. The pulse envelope is again a $\sin^2$ function with an amplitude of $E_0 = 5 \cdot 10^{-4}$, yielding a target population of 37.5%.

For optimization of the guess field, the frequency optimization scheme is employed again, using the harmonic frequencies $\omega_k = \frac{2\pi}{T} k = 6.08 \cdot 10^{-4} \cdot k$ for $k = 1, 2, 3$.

The results are compared with ten-parameter CRAB. The fixed basis set uses the randomized harmonic frequencies $\omega_k = 0.68 \cdot 10^{-3}, 1.67 \cdot 10^{-3}, 1.73 \cdot 10^{-3}, 2.40 \cdot 10^{-3}, 4.47 \cdot 10^{-3}$.

In both cases the NMS and the Subplex (both from NLopt) method are used, again allowing a maximum of 200 function calls.

4.3.5 Krotov scheme

Results of the Morse and the LiCs system are compared with the field gained by MCTDH's optimal control tool `optcntrl` using the Krotov optimization scheme. It requires no frequency basis since it searches the entire space of numerically integrable functions. The physical input parameters as well as the initial guess pulse are identical, but the cost functional is given by

$$J = 1 - p_{\mathrm{target}} + \alpha \int_0^T \frac{E(t)^2}{\sin^2\left(\frac{\pi t}{T}\right)} \,\mathrm{d}t \tag{4.16}$$

The difference lies in the penalty term, where the $\sin^2$ ensures a smooth pulse. The penalty factor α is chosen to 0.01 for the Morse oscillator and 0.1 for the LiCs system (where overall smaller field amplitudes are used). The algorithm is executed for 10 iterations, which involves a total of 20 propagations (forward and backward in time) and takes about 30 minutes.

Given the larger search space and the computational cost of the Krotov scheme, it is expected to give the best result of all compared methods.

5 Results and Discussion

This chapter comprises the results of all calculations described in chapter 4 while following the same structure.

5.1 Harmonic Oscillator

5.1.1 Propagation

The wavefunction propagation worked as expected. The probability densities $|\Psi(x,t)|^2$ for different initial wavefunctions are displayed in figure 5.1. When the initial wavefunction was an eigenstate, no change over time was observed. The coherent states oscillated around zero with the harmonic frequency ω while the shape of the wavepacket did not change.

Every non-stationary state oscillates with this frequency. This can be shown analytically by representing the initial wavefunction in terms of the HO basis and propagating the expansion explicitly:

$$\Psi(0) = \sum_{n=0}^{\infty} c_n \phi_n \tag{5.1}$$

$$\Psi(t) = \sum_{n=0}^{\infty} c_n e^{-iE_n t} \phi_n = e^{-\frac{i\omega t}{2}} \sum_{n=0}^{\infty} c_n e^{-i \cdot n\omega t} \phi_n \tag{5.2}$$

using the known harmonic energies $E_n = \omega(n + \frac{1}{2})$. Apart from the irrelevant total phase $e^{-\frac{i\omega t}{2}}$, the wavefunction is periodic with the frequency ω.

Finally, the squeezed coherent state increased and decreased in width periodically, this time with the frequency 2ω. Al tough it looks Gaussian upon first glance, the wavefunction can be shown to vary in a more sophisticated manner. The coefficients c_n from equation (5.1) can be derived explicitly by calculating the scalar product of the initial Gaussian (which corresponds to the ground state of a HO with the same mass, but frequency Ω). Working in units where

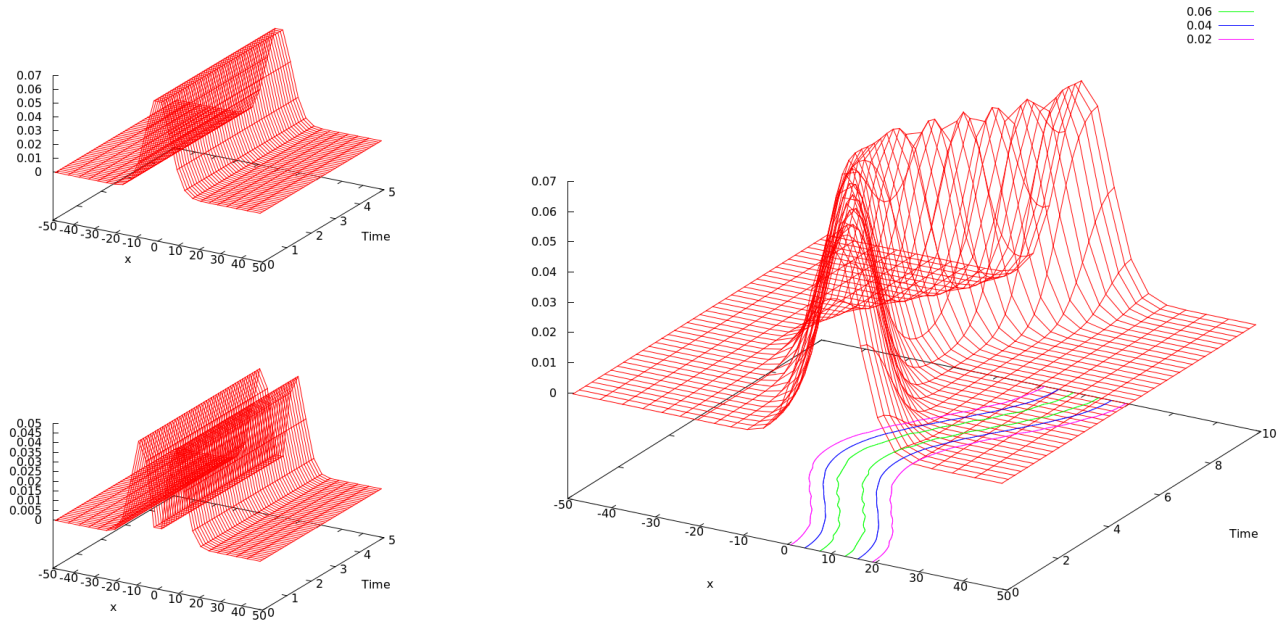

Figure 5.1: Probability densities in the HO. Top left: Ground state. Bottom left: First excited eigenstate. Right: Coherent state, initially centred around $x = 10$. All times in fs.

$m\omega = 1$, one finds:

$$c_n = \langle \Psi(x, t = 0) \mid \phi_n(x) \rangle \tag{5.3}$$

$$= \int_{-\infty}^{\infty} \left[\left(\frac{\Omega}{\pi} \right)^{\frac{1}{4}} e^{-\frac{\Omega}{2}x^2} \right] \cdot \left[\frac{1}{\sqrt{2^n n!}} \left(\frac{1}{\pi} \right)^{\frac{1}{4}} e^{-\frac{1}{2}x^2} H_n(x) \right] \mathrm{d}x \tag{5.4}$$

$$= \frac{1}{\sqrt{2^n n!}} \frac{\Omega^{\frac{1}{4}}}{\sqrt{\pi}} \int_{-\infty}^{\infty} e^{-\frac{1}{2}(\Omega+1)x^2} H_n(x) \, \mathrm{d}x \tag{5.5}$$

The first two Hermite polynomials are $H_0(x) = 1$ and $H_1(x) = 2x$. Therefore c_1 vanishes by symmetry (integral of an odd function), while c_0 reduces to the standard result

$$c_0 = \frac{\Omega^{\frac{1}{4}}}{\sqrt{\pi}} \int_{-\infty}^{\infty} e^{-\frac{1}{2}(\Omega+1)x^2} = \frac{\Omega^{\frac{1}{4}}}{\sqrt{\pi}} \cdot \sqrt{\frac{2\pi}{\Omega+1}} = \Omega^{\frac{1}{4}} \sqrt{\frac{2}{\Omega+1}} \tag{5.6}$$

It is interesting to take a look at the special case $\Omega = 1$. Since $H_0 = 1$, equation (5.5) can be

interpreted as the scalar product of H_0 with H_n with the weighting function e^{-x^2}:

$$\Omega = 1 \Rightarrow c_n = \frac{1}{\sqrt{2^n n! \pi}} \int_{-\infty}^{\infty} e^{-x^2} H_n(x)\,\mathrm{d}x \tag{5.7}$$

$$= \frac{1}{\sqrt{2^n n! \pi}} \int_{-\infty}^{\infty} H_0(x) e^{-x^2} H_n(x)\,\mathrm{d}x \tag{5.8}$$

$$= \frac{1}{\sqrt{2^n n! \pi}} \langle H_0 | H_n \rangle \tag{5.9}$$

$$= \delta_{0n} \tag{5.10}$$

With respect to this scalar product the Hermite polynomials are orthogonal. Thus when the initial wavefunction has the correct width, it just coincides with the ground state.

For arbitrary Ω, a recursive relation for c_n can be found via integration by parts while exploiting the fact that the Hermite polynomials satisfy $H_n = 2xH_{n-1} - 2(n-1)H_{n-2}$. The calculation is straightforward, but the exact values of c_n are not very important (c_{n+2} turns out to be simply proportionial to c_n). A look at the integral immediately reveals that $c_1 = c_3 = \ldots = 0$, as all odd-numbered Hermitian polynomials are, in fact, odd functions. Hence only the even-indexed coefficients $c_0, c_2, \ldots$ contribute to $\Psi(t)$, adding terms which are periodic in $2\omega, 4\omega, \ldots$. This explains why the period of the observed oscillation is 5 fs rather than 10 fs. In figure 5.2 the evolution of the density is plotted. For better spatial resolution, a grid size of 48 (instead of 12 a usual) was used to produce these figures.

5.1.2 Relaxation

It turned out that a modest number of basis functions is sufficient, but the default integrator settings need some adjustment for accurate relaxation of a wavefunction. Interestingly, bad settings result in a final energy *below* the ground state energy E_0. The algorithm converges rapidly (within less than one imaginary fs) to the correct energy scale, but then slowly falls further in energy.

The default integrator for the SPFs is Bulirsch-Stoer (BS) with an accuracy of 10^{-6}. It deviates from the exact result $E = 217.691071\,\mathrm{eV}$ by about $0.365\,\mathrm{eV}$, which is too large an error for quantum chemical calculations. By setting the integrator accuracy up to 10^{-8}, the result could be improved to acceptable accuracy, but it was still worse than other integrators.

Better results were obtained with the Adams-Bashforth-Moulton (ABM) integrator and the Runge-Kutta (RK) integrators (order 5 and order 8 were available and showed comparable performance). Both gave much better results than BS at an accuracy of 10^{-6} and were exact in all nine significant digits when using an integrator accuracy of 10^{-8}.

A larger primitive basis did not improve the result, and even 12 basis functions proved sufficient for exactness. No significant difference was observed between the VMF and the default CMF (variable/constant mean field) integration scheme. Some of the tested configurations are

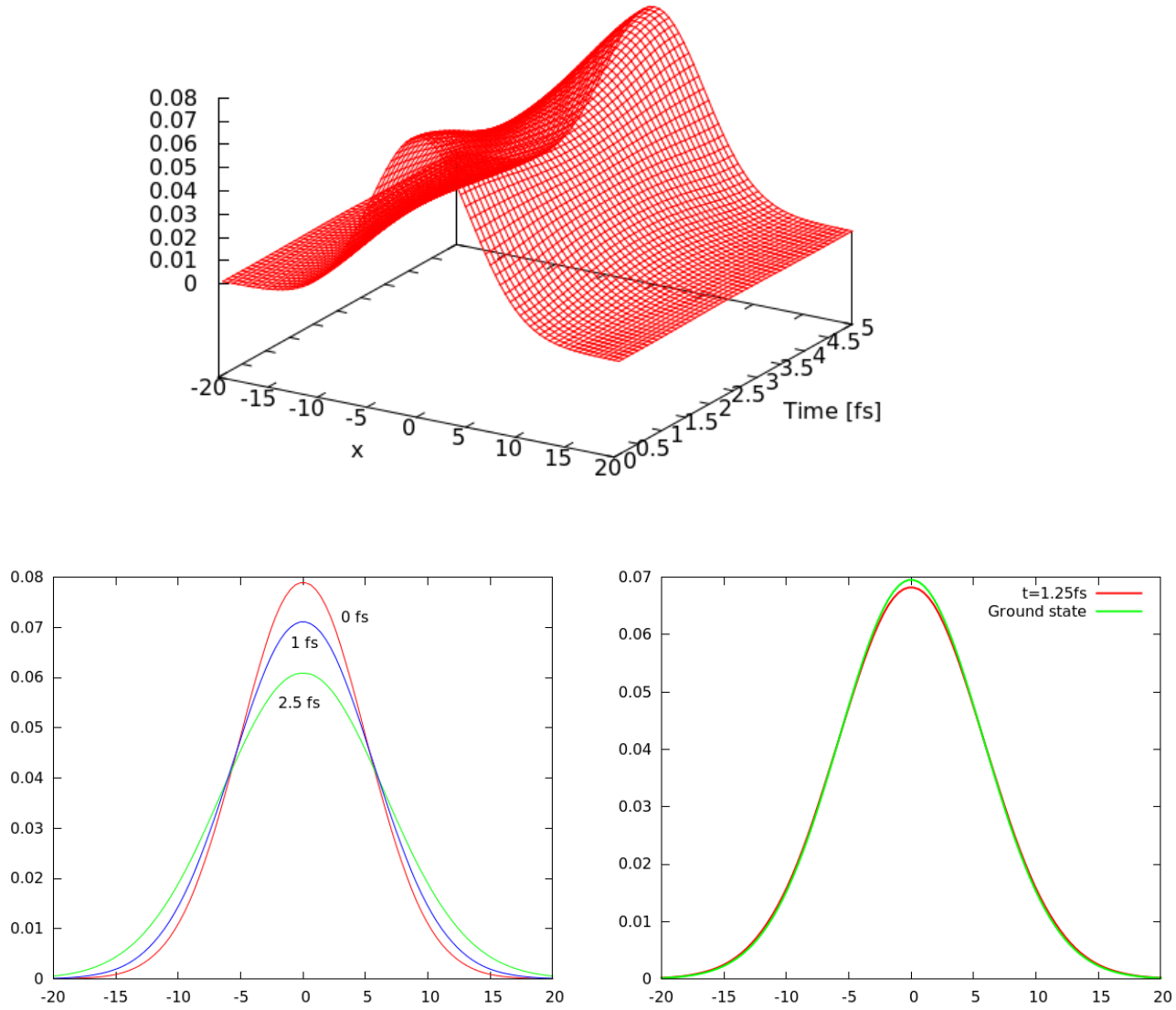

Figure 5.2: Density of a squeezed coherent state, evolving in time. Bottom left: Densities at different times. The 4 fs density coincides with the 1 fs density, same for 0 fs and 5 fs. Bottom right: Density at $t = 1.25\,fs$, compared with the ground state density. Note that $|\Psi(x)|^2$ is smaller than the Gaussian at the centre, but higher at the flanks. Top: 3d view of the density.

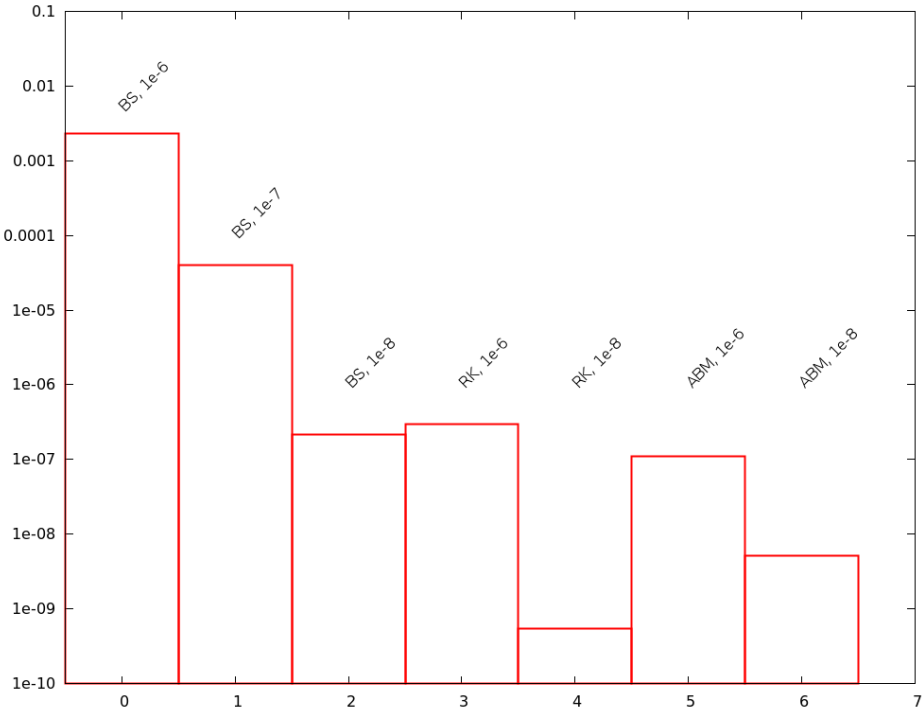

Figure 5.3: Accuracy of the relaxation with different integrators, using the CMF scheme. The bars represent the relative error of the calculation $|1-E_{\text{computed}}/E_{\text{exact}}|$. The number after the integrator name (see text for abbreviations) is the integrator accuracy.

compared in figure 5.3.

5.1.3 Coupling to a field

An interaction such as (4.3) effectively shifts the zero of the potential to

$$x_0 = \mu_0 \frac{1}{2} E(t) \tag{5.11}$$

without changing the harmonic features of the oscillator. This system has been solved explicitly in the framework of *Floquet theory* [9]. The fundamental solutions of the TDSE are the so-called Floquet modes

$$\Psi_n(x,t) = \varphi_n(x - \xi(t)) e^{i\phi(t)} \tag{5.12}$$

where φ_n are the eigenfunctions of the unperturbed HO, the coordinate shift $\xi(t)$ obeys the equation of motion

$$\ddot{\xi}(t) + \omega^2 \xi(t) = \mu_0 E(t)/m \tag{5.13}$$

and the phase $\phi(t)$ is a functional depending on time and on $\xi(t)$ (see the literature [9] for the explicit form). As a result, this type of interaction just creates a coherent state, but is incapable

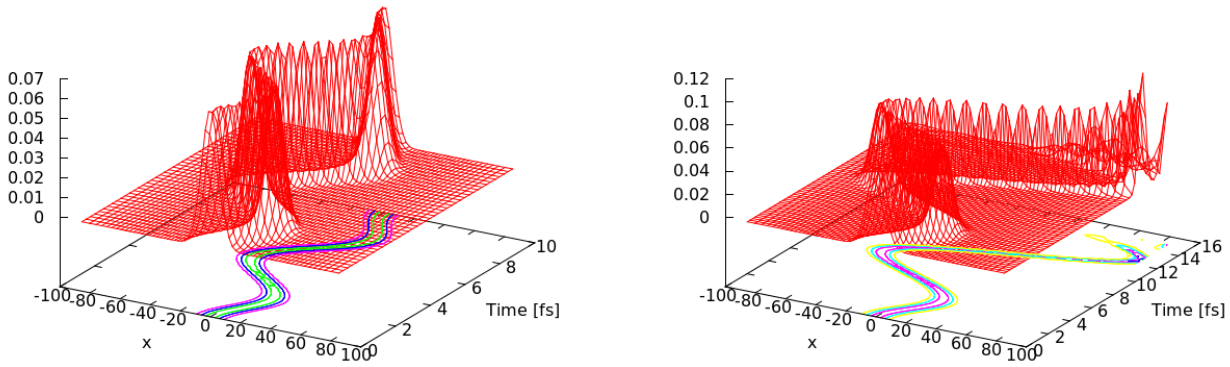

Figure 5.4: Wavepacket in a monochromatic field, off-resonant with $\omega_L = 2\omega$ (left) and resonant $\omega_L = \omega$ (right). The artefacts after 12 fs in the resonant case stem from reflection of the wavepacket at the grid borders.

of selectively exciting specific eigenstates. This can be checked by inspecting the occupation numbers n given in the output file of MCTDH: At any time $\Delta n = \sqrt{\langle n \rangle}$ holds, just as is known for coherent states.

A monochromatic field $E(t) = E_0 \cos(\omega_L t)$ leads to a classical forced oscillation. Solving the equation of motion for $\xi(t)$ yields [9]

$$\xi(t) = \frac{\mu_0 E_0}{m} \frac{1}{\omega_L^2 - \omega^2} \cos(\omega_L t) \tag{5.14}$$

The amplitude shows the typical Lorentzian dependency on the frequency, including divergence for the resonant case $\omega_L \to \omega$. Both the off-resonant and the resonant behaviour could be reproduced[1] with MCTDH as can be seen in figure 5.4. Finite-length pulses excite the pulse to a coherent state. After the pulse ends, the system oscillates just as in section 5.1.1. One representative example is depicted in figure 5.5.

5.2 Morse Oscillator

5.2.1 Choice of DVR

As mentioned before (section 4.2), eventually a primitive basis of 96 sine functions was chosen spanning a grid from $x_0 = 0.7$ to $x_{97} = 8.0$. This is justified by the results of the following paragraph. Until this insight was gained, a HO DVR with $N = 64$ had been used for propagation. This should not affect the accuracy of those calculations, although the calculation time was unnecessarily long.

[1] In case of resonance the wavefunction soon hit the borders of the grid, which is interpreted as a rise to infinity.

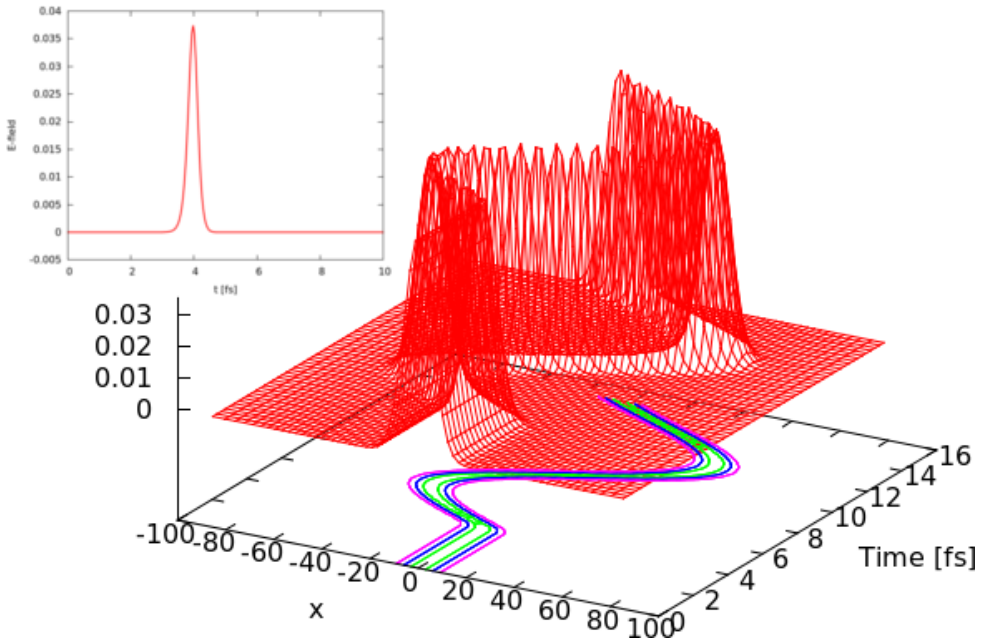

Figure 5.5: Light pulse (top left) exciting the wavepacket in the HO potential. All pulses depicted in figure 4.3 resulted in a qualitatively similar behaviour.

5.2.2 Diagonalization

All 22 eigenenergies of the Morse oscillator could be calculated with MCTDH with a primitive basis of size 128. The calculations in the HO basis accurately returned the first 10 to 15 energies, but failed dramatically for the higher states. The sine DVR from $x = 0.7$ to 8.0 gave a much better overall performance, as can be seen in figure 5.6. Only the last bound state was determined incorrectly when MCTDH insisted that $E_{21} > 0$.

This could be improved by stretching the grid to an upper limit of $x = 12.0$ while keeping the number of basis function at 128. With this DVR all eigenenergies including E_{21} were found to great accuracy, see table 5.1 for the results.

It is concluded that a sine DVR is the best choice for possibly dissociative modes. Since no simulations directly involve states higher than $|15\rangle$, the smaller grid (upper limit 8.0) was chosen to achieve higher spatial resolution at moderate internuclear distance.

5.2.3 State selective excitation

The coupling to a light field described in section 4.2.3 gave the expected results. The first paragraph of this section presents the Rabi oscillations, while the following paragraphs describe the path to selective excitation of the $|15\rangle$ state.

Rabi Oscillations

In a monochromatic light field $E_0 \cos(\omega_L t)$, the Morse oscillator performed Rabi oscillations with the predicted amplitude and Rabi frequency Ω. Figure 5.7 shows the evolution the popula-

n	E_n [eV]	MCTDH error
0	-5.18301	$+1.06 \cdot 10^{-12}$
1	-4.71383	$+3.77 \cdot 10^{-12}$
2	-4.26690	$+5.05 \cdot 10^{-12}$
3	-3.84222	$+1.23 \cdot 10^{-11}$
4	-3.43981	$+1.01 \cdot 10^{-10}$
5	-3.05964	$+3.56 \cdot 10^{-10}$
6	-2.70174	$-5.00 \cdot 10^{-10}$
7	-2.36608	$-7.99 \cdot 10^{-9}$
8	-2.05269	$-2.51 \cdot 10^{-8}$
9	-1.76154	$-1.53 \cdot 10^{-8}$
10	-1.49266	$+1.47 \cdot 10^{-7}$
11	-1.24603	$+6.28 \cdot 10^{-7}$
12	-1.02165	$+1.39 \cdot 10^{-6}$
13	-0.81953	$+1.87 \cdot 10^{-6}$
14	-0.63967	$+8.37 \cdot 10^{-7}$
15	-0.48206	$-3.25 \cdot 10^{-6}$
16	-0.34671	$-1.17 \cdot 10^{-5}$
17	-0.23361	$-2.56 \cdot 10^{-5}$
18	-0.14276	$-4.64 \cdot 10^{-5}$
19	-0.07418	$-7.90 \cdot 10^{-5}$
20	-0.02784	$-1.44 \cdot 10^{-4}$
21	-0.00377	$-7.39 \cdot 10^{-3}$

Table 5.1: Eigenenergies of the Morse oscillator as determined from equation (2.14). The last column gives the relative error of the diagonalization with MCTDH when using the 128-point sine DVR ranging from 0.7 to 12.0.

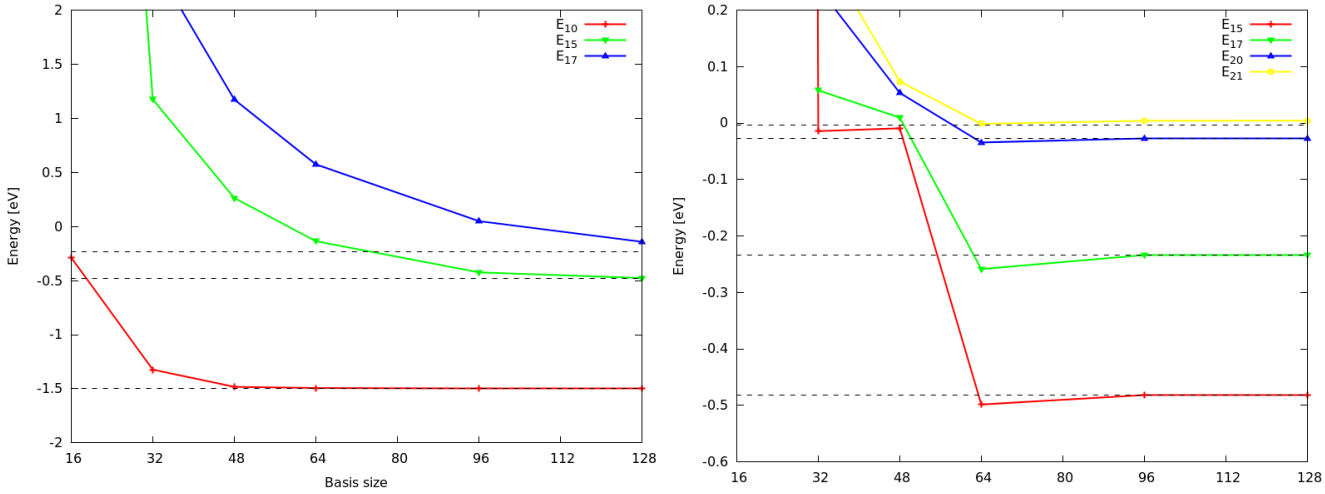

Figure 5.6: Selected eigenenergies found by diagonalization of the Morse Hamiltonian as a function of basis size. Left: HO DVR. Right: Sine DVR. The dashed lines represent the exact energies.

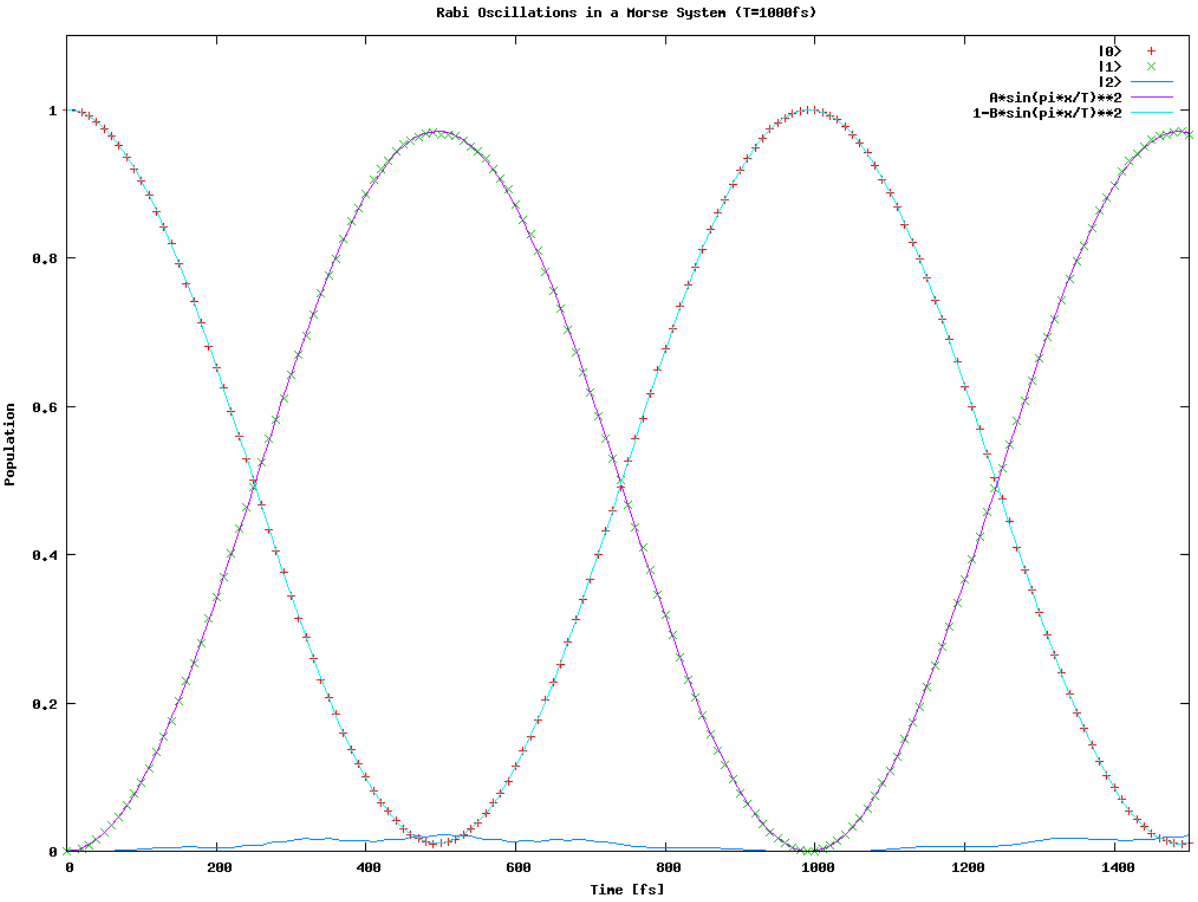

Figure 5.7: Rabi oscillations of the Morse system in a monochromatic field with $\omega_L = 3784.2\,\mathrm{cm}^{-1}$ and $E_0 = 5.9746 \cdot 10^{-3} = 3.07\,\mathrm{MV/m}$. According to (4.2.3) this corresponds to a Rabi period of 1 ps. The points are the time-dependent populations p_0 and p_1 along with the fitted $\cos^2(\Omega t)$ resp. $\sin^2(\Omega t)$ functions. The curve at the bottom illustrates the quality of the two-state approximation, as the population p_2 reaches 0.02 at most. A closer look reveals that the Rabi period of this oscillation is not exactly 1 ps, but rather 992 fs. It turns out that the exact resonance frequency is slightly higher, see the text and figure 5.9.

tions $p_n = |\langle\Psi(t)|n\rangle|^2$ for one and a half Rabi cycles in the resonant case. An off-resonant field with the frequency $\omega_L = \omega + \Delta$ led to the expected decline in population transfer and increased Rabi frequency Ω' as given by

$$\begin{aligned} \Omega' &= \sqrt{\Omega^2 + \Delta^2} \\ \max(p_1) &= \frac{\Omega^2}{\Omega^2 + \Delta^2} \end{aligned} \tag{5.15}$$

One example of a detuned Rabi oscillation is depicted in figure 5.8 while figure 5.9 shows data collected from a number of such simulations with different detuning. Equations (5.15) are shown to hold, and the fits show the resonant frequency to lie at $3787.4\,\mathrm{cm}^{-1}$. This is about one percent larger than what would be expected from the difference of eigenenergies $E_1 - E_0 = 3784.2\,\mathrm{cm}^{-1}$.

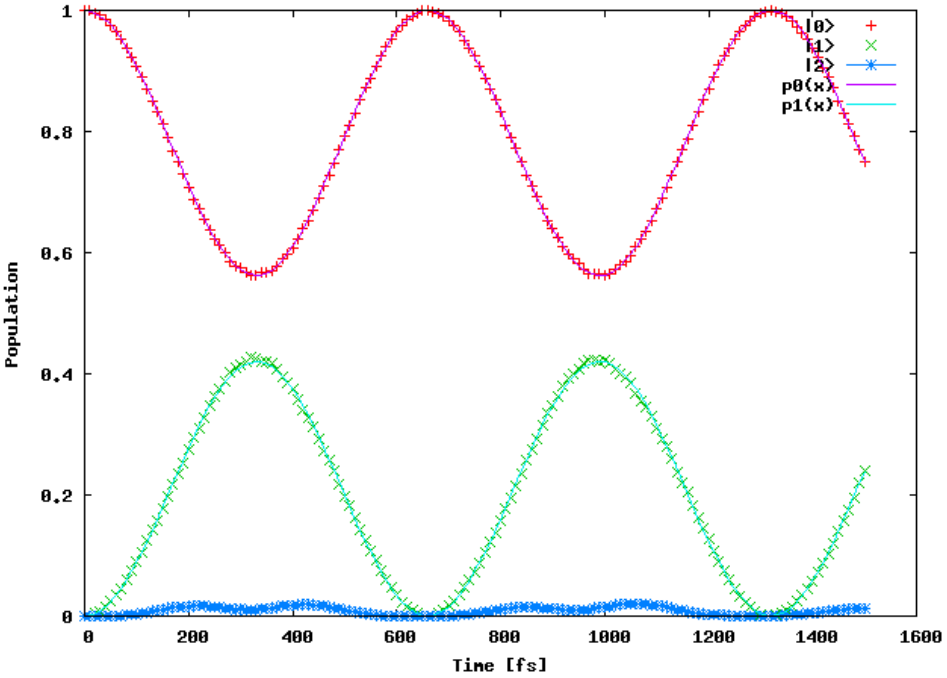

Figure 5.8: Rabi oscillations in a detuned laser field with the frequency $\omega_L = 0.991\omega$.

After checking the accuracy in the input parameters, the most likely explanation appears to be a systematic error such as coupling to the $|2\rangle$ state.

Population transfer was also performed successfully with Gaussian pulses with the frequency $\omega_L = 3784.2\,\mathrm{cm}^{-1}$. Figure 5.10 illustrates the transfer of the system into state $|1\rangle$ and the coherent superposition $\frac{|0\rangle+|1\rangle}{\sqrt{2}}$ with a π-pulse and a $\pi/2$-pulse, respectively. After successful excitation with one π-pulse, a sequence of two Gaussian pulses was used to excite the system into $|2\rangle$ via $|1\rangle$. The first pulse again had a frequency of $\omega_{10} = 3784.2\,\mathrm{cm}^{-1}$, while the second pulse was tuned to excite the next transition at $\omega_{21} = 3604.7\,\mathrm{cm}^{-1}$. The population over time is plotted in figure 5.11.

Finally, there were also cases of failed selective excitation. One example of a failed population transfer to $|1\rangle$ is depicted in figure 5.12. In this case, an attempt was made to complete the population transfer in just 50 fs, i.e. just a few optical cycles.

The derivation of the Rabi oscillations relies on the *Rotating Wave Approximation* (RWA) which states that the coefficients $c_n = \langle\Psi(t)|n\rangle$ change on a much longer timescale than the external field [11]. This is no longer the case here, so the RWA breaks down. Also, a pulse[2] with a width of 25 fs in the time domain has a spectral width of over $200\,\mathrm{cm}^{-1}$. With the excitation energy ω_{21} lying closer to ω_{10} than this, significant excitation from $|1\rangle$ to $|2\rangle$ occurred.

[2]To be clear, a constant amplitude field was used. But on this time scale the difference between such a field and a light pulse blurs.

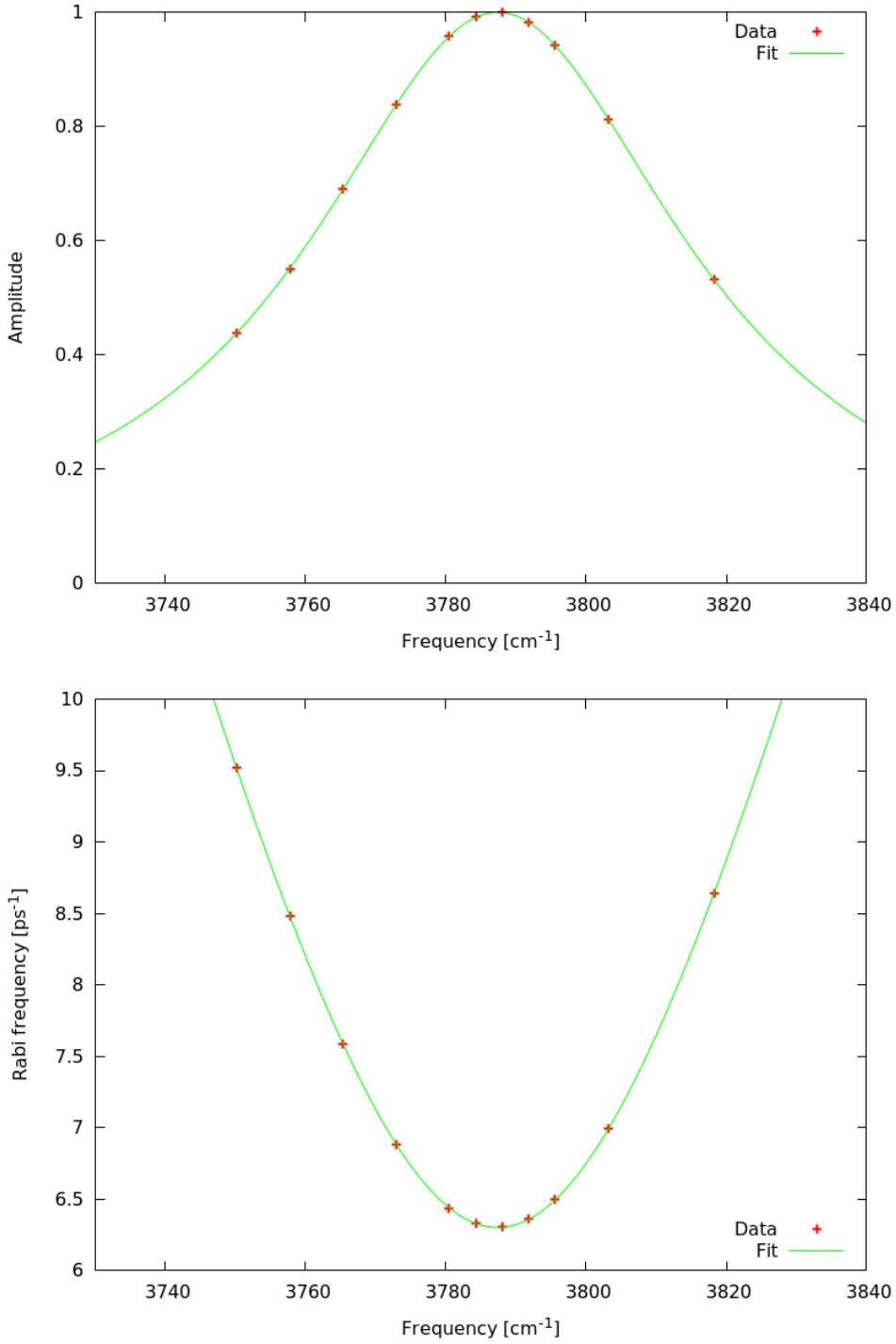

Figure 5.9: Detuned Rabi oscillations. Amplitude (top) and Rabi frequency (bottom) as a function of the laser frequency, along with fits of the form (5.15). The extrema lie at a resonant frequency of $3787.4\,\mathrm{cm}^{-1}$.

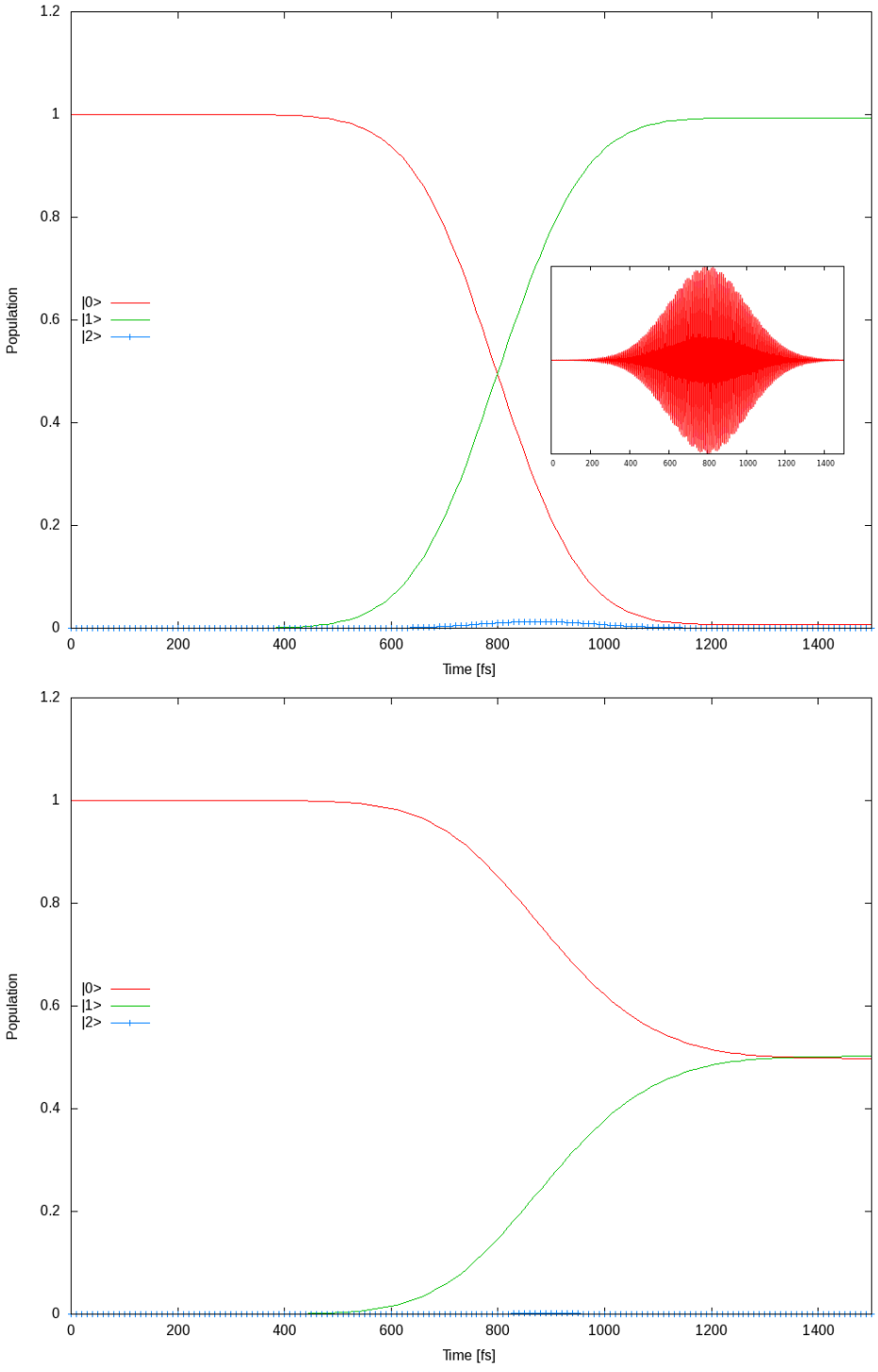

Figure 5.10: Top: A π-pulse with the parameters $E_0 = 5.9746 \cdot 10^{-3}$ and the normalization constant (see equation (4.10)) $N = T/2 = 2.07 \cdot 10^4$ excites the system into state $|1\rangle$. The pulse is centered around $t = 800$ fs with a width of 200 fs (see inset). The target population reached a final value of $p_1 = 99.3\%$. Bottom: $\pi/2$-pulse with the same parameters as above except for the amplitude, which was halved.

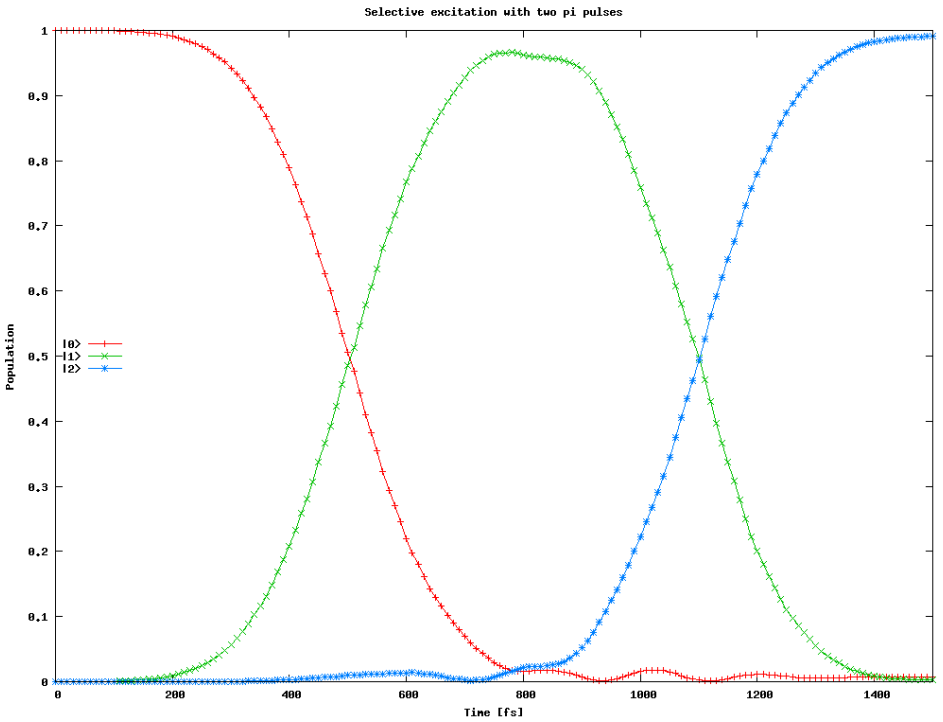

Figure 5.11: Two Gaussian pulses centered around 0.5 ps and 1.1 ps with a width of 0.2 ps each excite the system into $|2\rangle$. The final population was $p_2 = 99.1\%$.

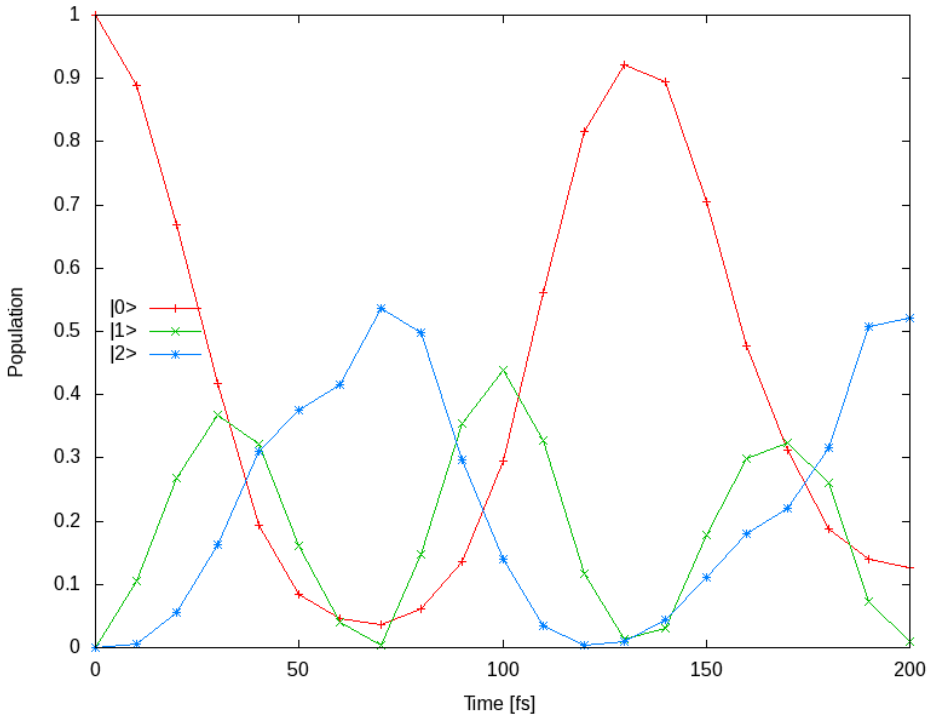

Figure 5.12: Failed population transfer due to a very short, intense pulse.

$|0\rangle$ to $|15\rangle$ to $|10\rangle$ excitation

The pulse parameters described in [15] and reprinted in section 4.2.3 were used to successfully transfer the system to $|5\rangle$ and then to $|10\rangle$ via multi-photon absorption with two $\sin^2$-shaped pulses of 1 ps length. The target populations reached a value of $p_5 = 99.996\%$ after 1 ps and $p_{10} = 99.986\%$ after 2 ps. Unfortunately these values cannot be compared with the original paper, which is as unspecific as "close to 100%" at this point.

Notably, the excitation to $|10\rangle$ was the point when the HO DVR failed. While the harmonic oscillator with size $N = 64$ basis was good enough to model the system up to $|5\rangle$, an accurate simulation of the next step required a more suitable DVR. After changing to a sine DVR of the same basis size, the results matched those reported in [15]. See figure 5.13 for a comparison. In addition the CPU time required for the calculations decreased by a factor of 5 to 10.

$|10\rangle$ to $|15\rangle$ excitation

The new grid ranged from $x = 0.7$ to 6.0, which was apparently sufficient for an accurate calculation up to state $|10\rangle$. However, this DVR failed as well when further excitation to $|15\rangle$ was simulated. Hence it was extended to $x = 8.0$ and a basis size of $N = 96$. The difference is clearly visible in figure 5.14. Here "Well" denotes the cumulative population of all bound states, i.e. $p_{\text{Well}} = \sum_{n=0}^{21} p_n$. Hence the dissociation probability is $D = 1 - p_{\text{Well}}$, which amounts to 4.15% when using the larger grid. The target population amounted to $p_{15} = 94.8\%$, so the *state-selectivity* defined as $S = p_{15}/p_{\text{Well}}$ is 98.5%. This last value is only in approximate agreement with [15], where a value of $S = 99.2\%$ was reported. The target population and dissociation probability are even less accurate, as the reference values are $p_{15} = 92.4$ and $D = 6.9\%$. The simulations performed in this thesis seem to drastically underestimate the dissociation probability. This point will be addressed further below.

However the results were in qualitative agreement with results of the reference which are shown in figure 5.15 (top). Therefore no modifications to the input were when turning to the last excitation scheme presented in [15]. Here the final excitation step was simulated as a one-photon process by setting the frequency of the final pulse to the overtone $\omega_3 = 8148.6\,\text{cm}^{-1}$. At the same time the pulse train was compressed to a total length of 1600 fs as described in section 4.2.3.

The result of the calculation can be seen in figure 5.16 (top) and should be contrasted with the known result shown in figure 5.15 (bottom). Here the failure to predict the dissociation probability was even more evident. The authors of [15] reported a dissociation probability of $D = 4.14\%$, a target state population of $p_{15} = 94.54\%$ and a state selectivity of $S = 98.62\%$. The results obtained here were $D = 0.24\%$, $p_{15} = 98.45\%$ and $S = 98.69\%$, respectively. Although the state selectivity happened to agree with the literature, the other values are considerably off.

Checking the population of the last few grid points revealed that part of the wavefunction had indeed propagated all the way to $x = 8.0$ where it was reflected at the edge of the grid. In such a case a CAP as described in section 4.2.3 is called for. The simulations were repeated with

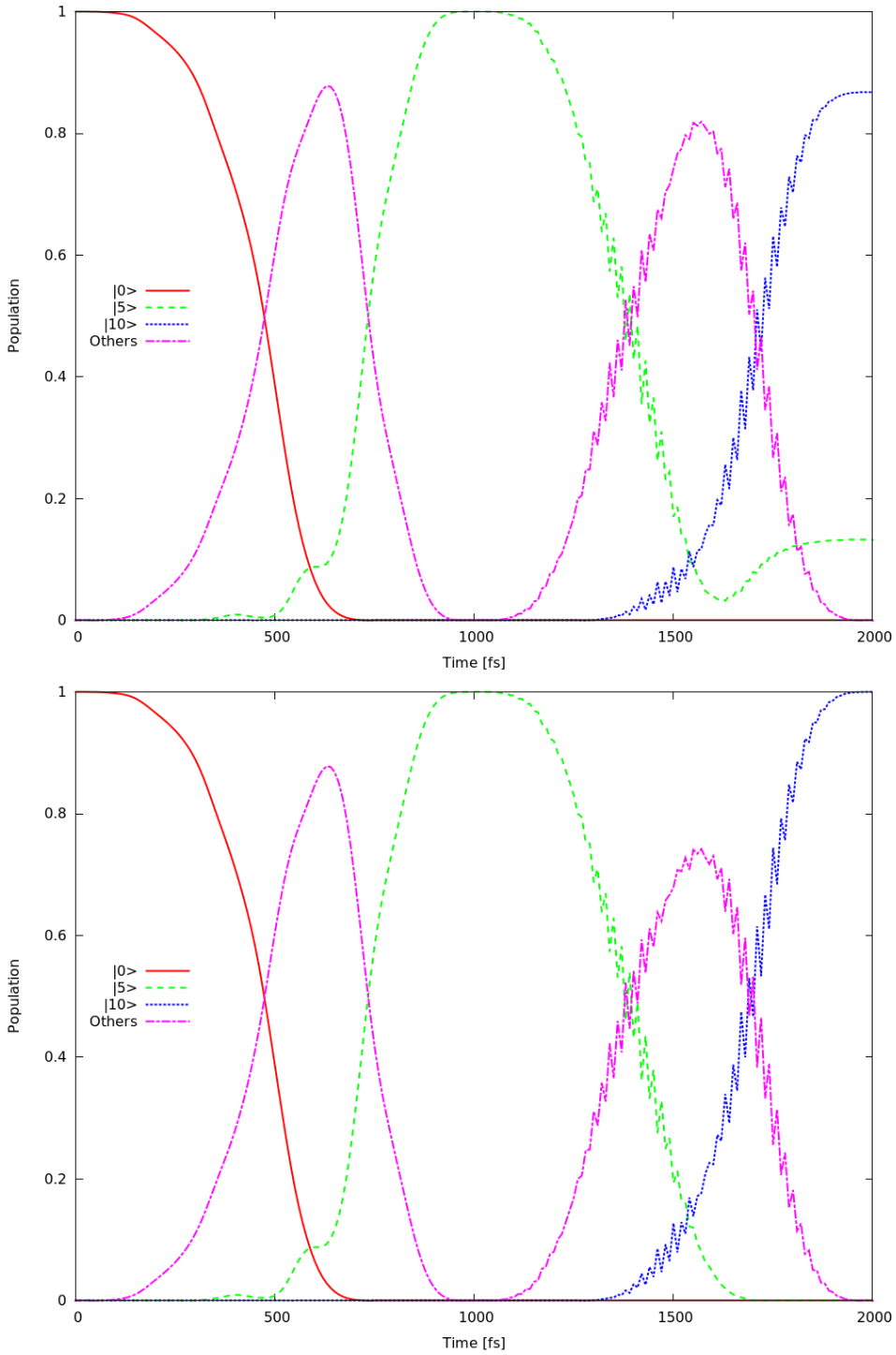

Figure 5.13: Excitation of the Morse oscillator to the target state $|10\rangle$ with two monochromatic pulses. The plots show the populations of the most important states over time and only differ in the DVR used. Top: HO DVR of size $N = 64$. Bottom: Sine DVR of the same size.

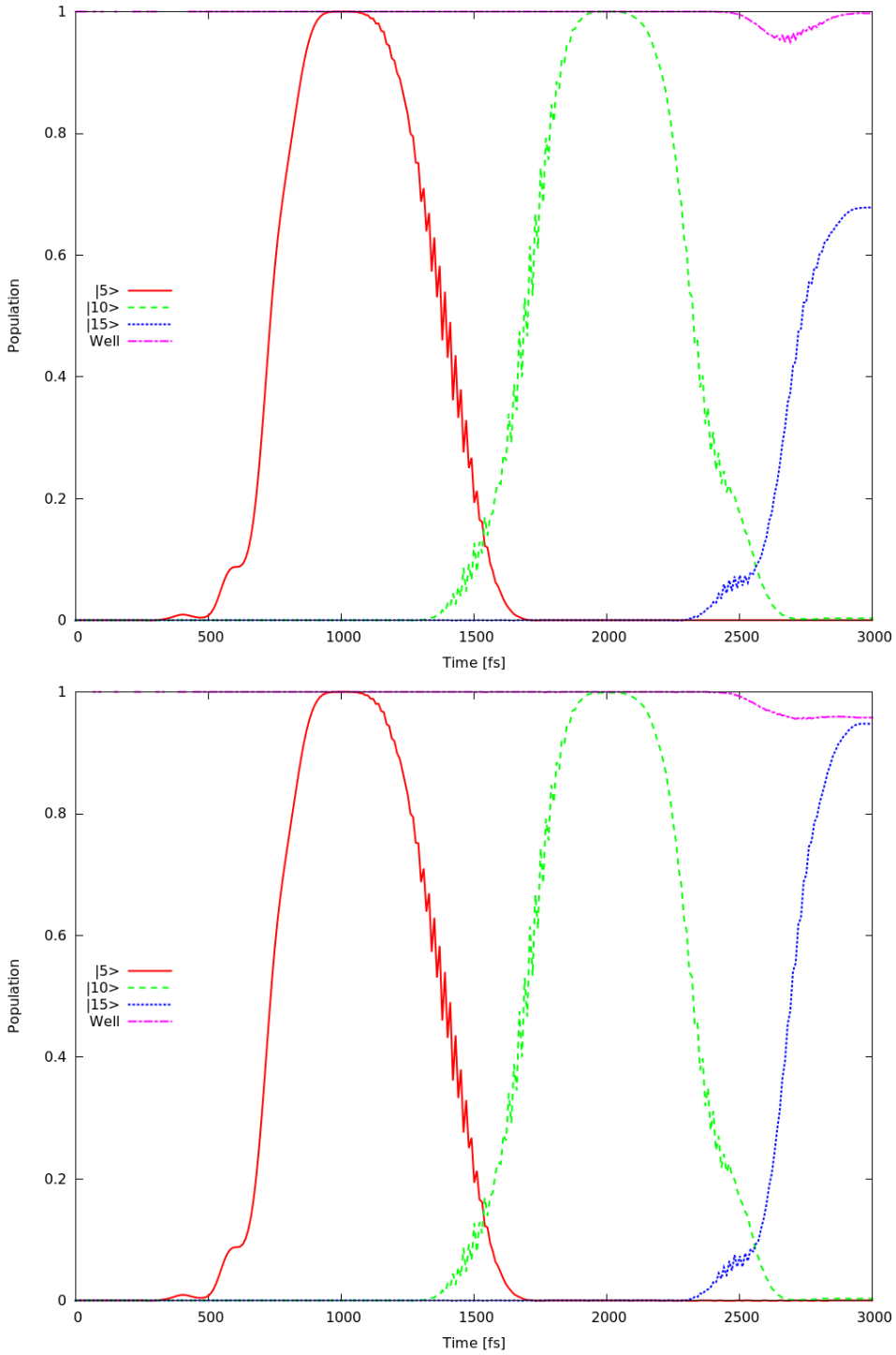

Figure 5.14: Excitation to the target state $|15\rangle$ with a sequence of three pulses (see figure 4.4). Both plots are the result of calculations with a sine DVR. Top: Basis size 64, $x = 0.7 \ldots 6.0$. Bottom: Basis size 96, $x = 0.7 \ldots 8.0$.

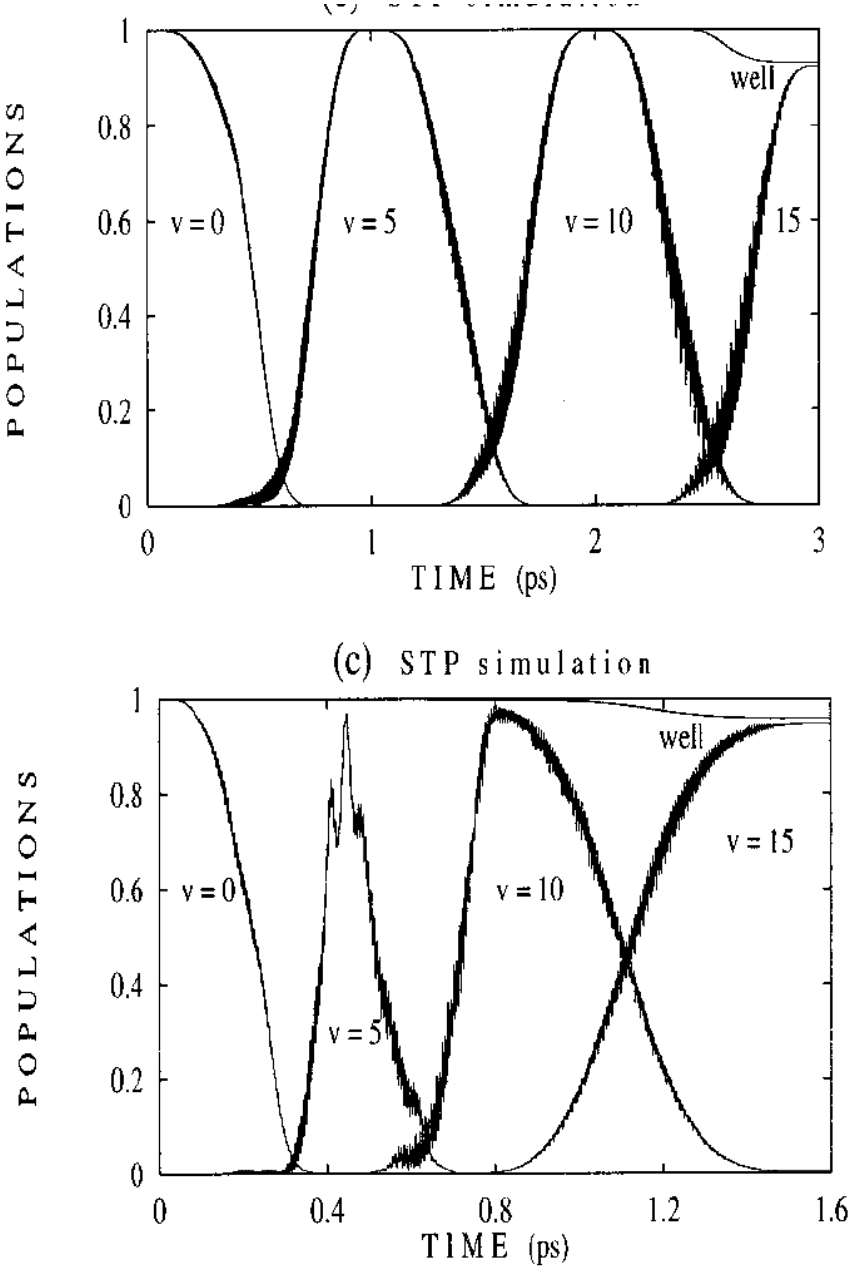

Figure 5.15: Population dynamics taken from [15]. Top: Population of $|15\rangle$ via multi-photon absorption as in figure 5.14 (bottom). Bottom: Shortened pulse train with an overtone transition to excite $|15\rangle$. Compare to figure 5.16 (bottom).

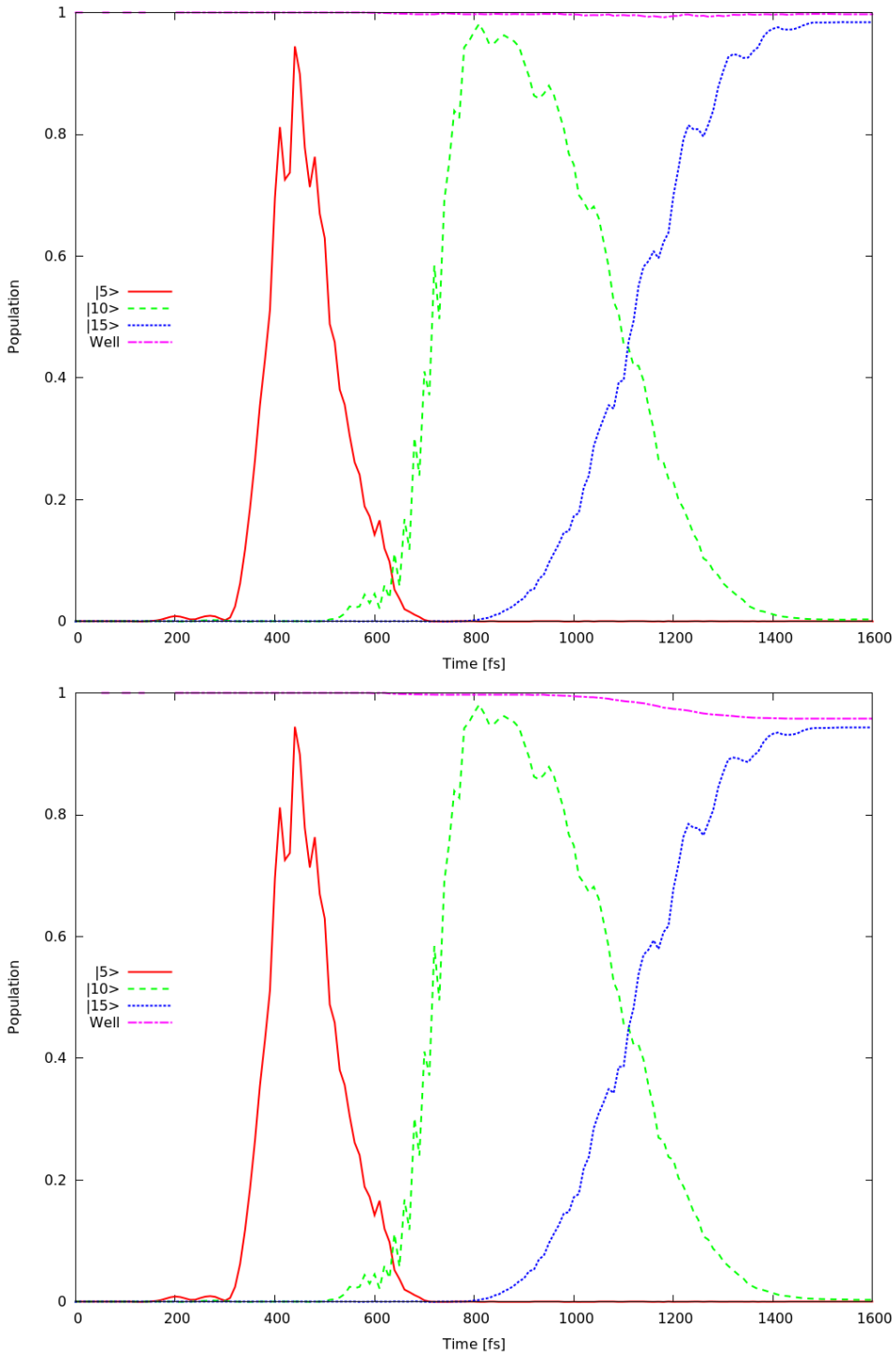

Figure 5.16: State populations with an overtone transition from $|10\rangle$ to $|15\rangle$ without (top) and with (bottom) CAP.

the CAP parameters described there, leading to the populations shown in figure 5.16 (bottom). The improvement is striking and also the numerical results are much more convincing with $D = 4.23\%$, $p_{15} = 94.36\%$ and $S = 98.53\%$. The final wavefunction had a norm of $\int |\Psi|^2 \mathrm{d}x = 0.9786$, so about 2.1% of the total population had absorbed away by the CAP. The norm remained larger than 0.999 until about $700\,\mathrm{fs}$, when a significant part of the wavefunction approached the grid edge.

The dissociation probability was thus determined to be slightly larger than expected. This might be due to the CAP damping some part of the wavefunction which was just below the dissociation threshold, but still in a high bound state. A possible remedy would be to use an even larger grid (e.g. ranging to $x = 12.0$) and shifting the CAP further to the right. This would make sure that only the truly dissociative parts of Ψ hit the CAP. However such refinements are left to future studies.

As a conclusion of this subsection, the importance of a suitable DVR and CAPs has been highlighted. As soon as higher excited states are involved, a sine DVR or a similar primitive basis is inevitable for reliable results. A HO DVR might still work accurately at medium quantum numbers (near $|5\rangle$), although the sine DVR is still much more efficient there. When setting the borders of the grid, care has to be taken such that all involved states (in the dissociative case, this usually includes all bound states) can be represented on the grid. Unless the grid is much larger than necessary, part of the wavepacket is still likely to hit its edge. Albeit unphysical, a CAP can significantly improve the results of the simulation in this case.

5.3 Optimal Control

With the DVR and the CAP set up as described, various optimal control calculations were performed. The optimized field would usually not perform as impressively as the examples above, but in many cases they could improve significantly over the initial guess pulse $E^{\mathrm{guess}}(t)$.

5.3.1 One- and two-parameter control

For a resonant pulse with $\omega_L = 0.01724 = 3784.2\,\mathrm{cm}^{-1}$ the optimal[3] amplitude was found to be $E_0^{\mathrm{opt}} = 0.0059 = 3.03\,\mathrm{MV/m}$, yielding a target population of $p_1 = 99.3\%$. Likewise the frequency was optimized while keeping the amplitude fixed, but the result $\omega_L^{\mathrm{opt}} = 0.01725$ deviated just very slightly from the resonant frequency. Figure 5.17 shows a full scan of the regions of interest in both cases. The multiple peaks in $p_1(E_0)$ can be explained by interpreting the population transfer as a Rabi oscillation with a Rabi frequency proportional to E_0. Full population of $|1\rangle$ occurs whenever $\int \Omega(t)\mathrm{d}t = \pi, 3\pi, 5\pi, \ldots$, and an increasing amplitude will periodically fulfil this condition at $E_0 = 0.018, 0.03 \ldots$.

[3] In the sense of maximizing target population, i.e. for a penalty factor $\alpha = 0$.

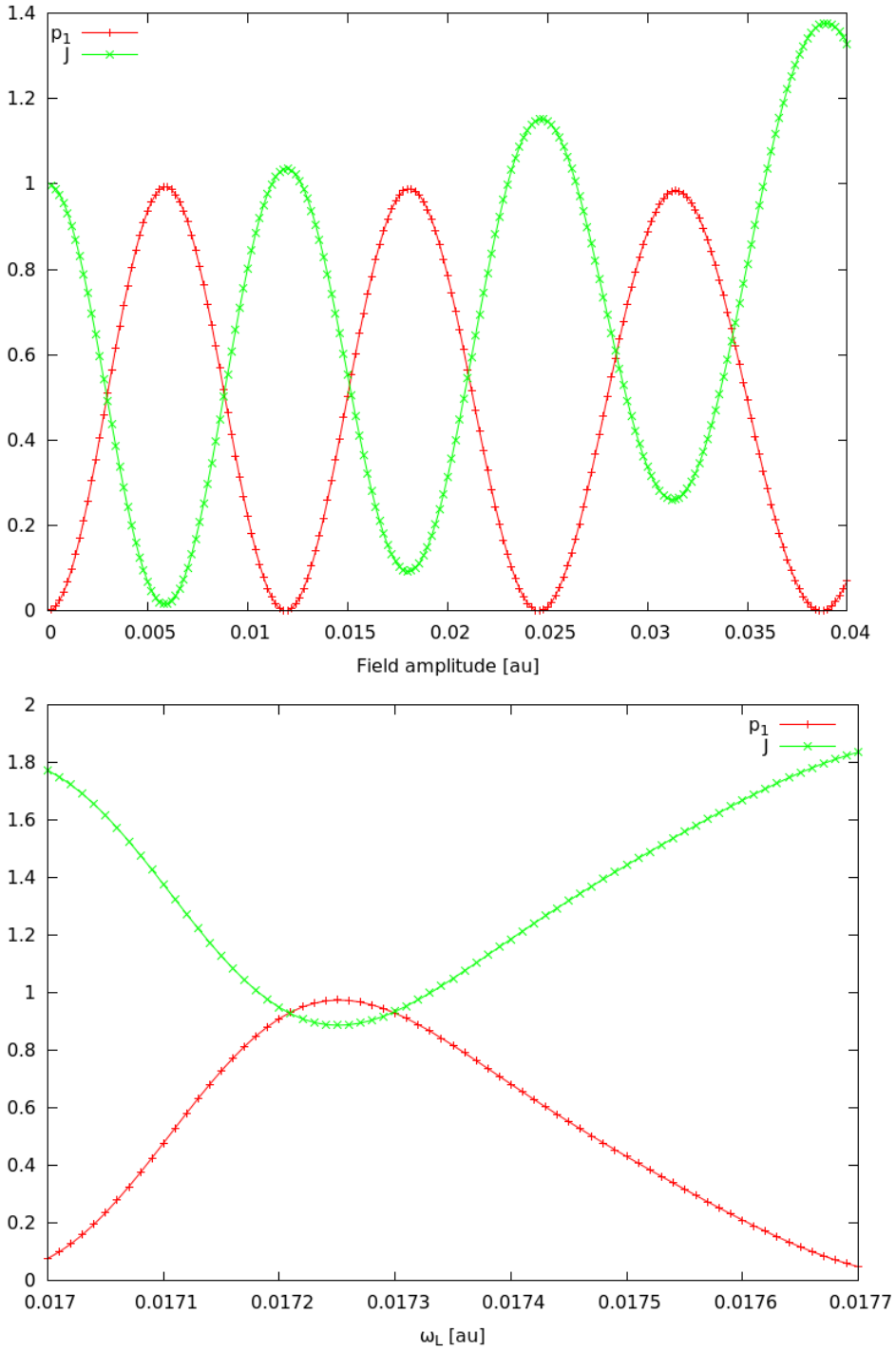

Figure 5.17: Target population p_1 and penalty function J as a function of the pulse amplitude (top) or frequency (bottom) while keeping the other quantity fixed at $\omega_L = 0.01724$ resp. $E_0 = 0.046$ (non-optimal on purpose to leave room for improvement). The penalty function was $J = 1 - p_1 + 250E_0^2$ in the first and $J = 1 - p_1 + 50\omega_L$ in the second case.

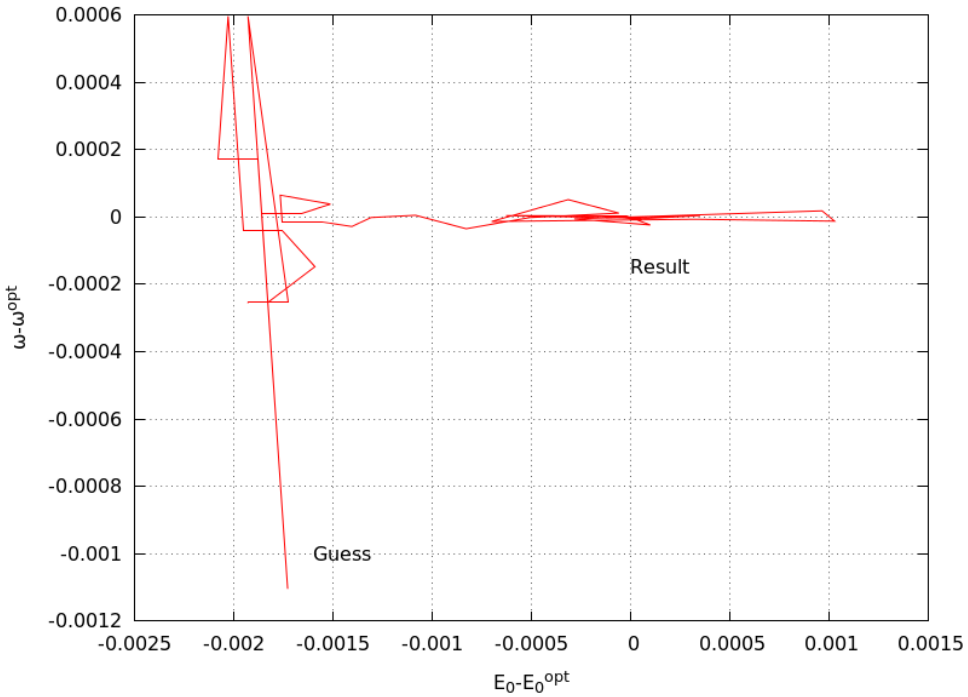

Figure 5.18: Convergence path in the E_0-ω_L-plane. Starting from a guess $E_0 = 0.004, \omega_L = 0.017$, the NMS algorithm found a minimum of the cost functional at $(E_0^{\text{opt}}, \omega^{\text{opt}}) = (0.00593, 0.0172)$ (all in au). The final population of $|1\rangle$ reached $p_1 = 99.98\%$.

Rather surprisingly, the gradient-based algorithms in `scipy.optimize` failed to minimize J in both cases. While the simplex algorithm (NMS) would find at least a local minimum for most starting values, all other algorithms consistently diverged to very large or even negative values of the variables within a few iterations. Apparently the numerical derivative of the cost functional is unreliable, which is somewhat surprising given the smooth appearance of the curves in figure 5.17. This behaviour could not be alleviated with a different penalty factor or preconditioning of the problem (i.e. variable transformations to avoid numerical instabilities).

It is also not a consequence of the pathological nature of the one-dimensional case. The two-dimensional optimization via amplitude and frequency was equally unsuccessful with all gradient methods, while NMS converged quite reliably, see e.g. figure 5.18. Even with NMS the guess for ω_L must not be too far off, as a strongly detuned pulse will effectively return $p_1 = 0$, so the algorithm has little to work with.

Therefore only direct search methods such as NMS were employed in the following calculations. This is in accordance with the original paper on CRAB [5], which also promotes this type of algorithms.

5.3.2 CRAB with ten parameters

The initial pulse guess and the resulting populations are depicted in figure 5.19.

Attempts to optimize this pulse with a modulation of the type (3.29) gave mixed results de-

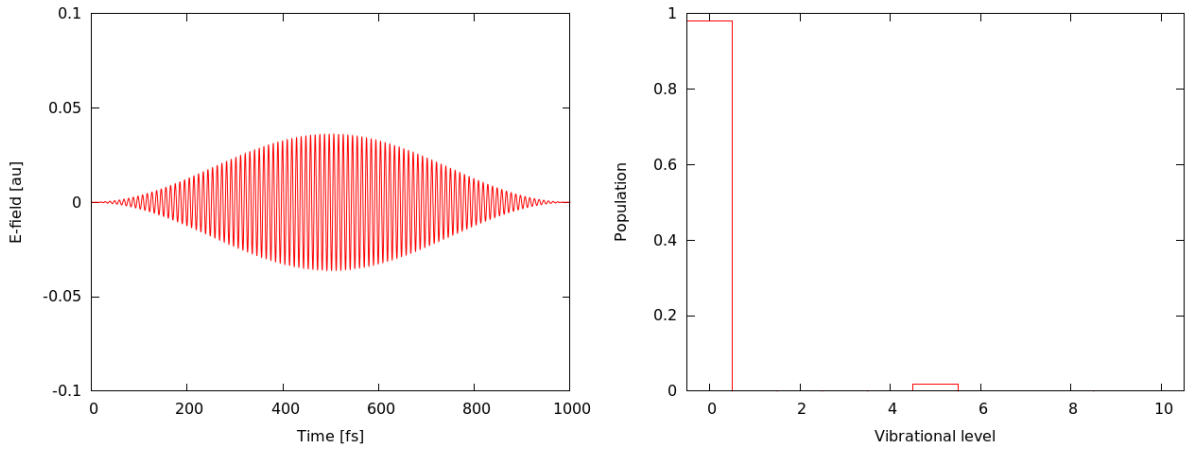

Figure 5.19: Left: Initial guess field with $E_0^{\text{guess}} = 0.0036, \omega^{\text{guess}} = 0.0156, T = 1000\,\text{fs}$. States populations after $t = T$. The target state $|5\rangle$ is populated with 1.98%.

pending on the quintuple of used frequencies and the optimization algorithm. These findings are discussed organized by the family of basis sets (resonant, harmonic or fully random frequencies), the application of CRAB (i.e. randomization of the basis) and the employed minimization algorithm (NMS from `scipy`, NMS from NLopt and Subplex from NLopt).

- On average the harmonic frequencies performed best with target populations consistently above 90%. The purely random frequencies turned out to be not very useful. One set of random frequencies failed completely in all optimization runs while the other converged to target population of barely over 50%. The resonant frequencies of the system gave overall satisfactory results, often reaching populations over 90%. Although the single best optimization run was made with one frequency set from this family (`eig-rn1`), others would occasionally fail and usually performed worse than the harmonic frequencies.

- Randomization in the spirit of CRAB showed little benefit here. Although one set of randomized resonant frequencies gave a superior result, all other randomized basis sets performed consistently worse than the exact frequencies. This applies both to the resonant and the harmonic families.

- An astonishing gap in performance was found between the `scipy.optimize` and the NLopt library. In all but one case, the NLopt algorithms converged much faster and to much better results than the `scipy` algorithm did. The reason is not entirely clear, as both NMS implementations employ the same strategy, i.e. use the same parameters for simplex evolution. Perhaps `scipy` chooses the initial simplex in an unfortunate manner. When comparing the two algorithms in the NLopt library, Subplex and NMS fared comparably well.

These results are summarized in table 5.2. Figures 5.20 to 5.22 illustrate the points made above.

The fields resulting from the resonant frequencies were very complex in shape with peak values near 0.2 au. The harmonic frequencies (exact or randomized) led to smoother pulses with

Table 5.2: Final target populations for all combinations of basis sets and algorithms after 200 function calls each. For details on the frequencies see table 4.1. A final value of 0.020 indicates no improvement over the initial guess.

Frequency set	scipy-NMS	NLopt-NMS	NLopt-Sbplx
`eig`	0.972	0.872	0.806
`eig-rn1`	0.992	0.994	0.999
`eig-rn2`	0.020	0.020	0.020
`eig-rn3`	0.472	0.669	0.572
`harm`	0.521	0.972	0.994
`harm-rn1`	0.819	0.961	0.976
`harm-rn2`	0.748	0.972	0.975
`harm-rn3`	0.646	0.991	0.940
`rand1`	0.020	0.587	0.553
`rand2`	0.020	0.020	0.020

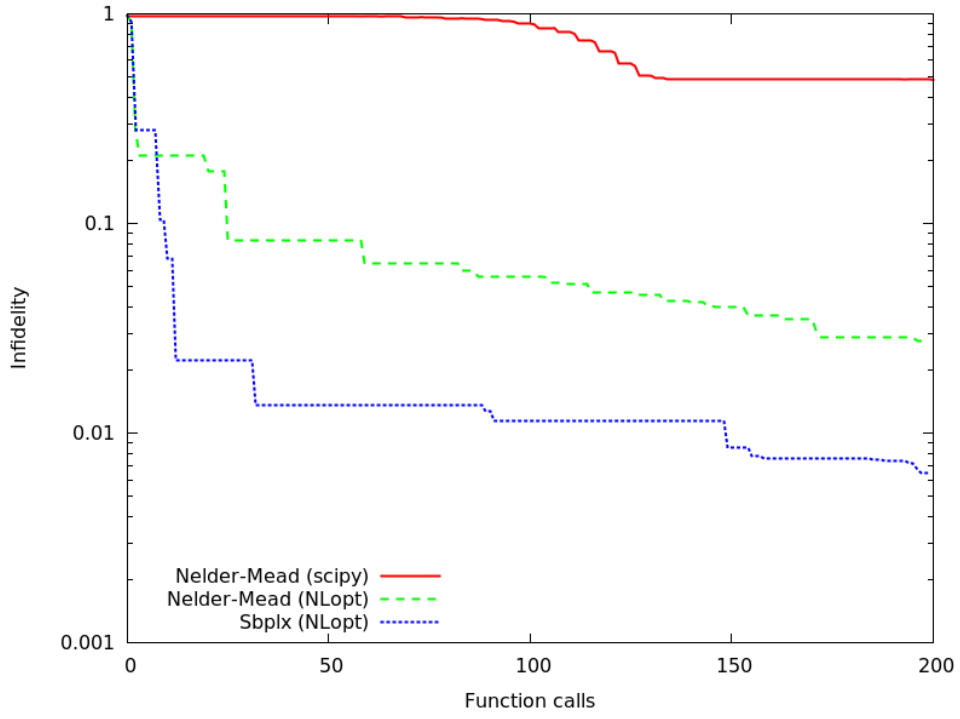

Figure 5.20: Performance of the different optimization algorithms with the exact harmonic frequency basis (`harm`). The plot shows the infidelity $1 - p_5$ versus the number of function evaluations. The Subplex method (Sbplx) worked best in this case with a final infidelity of just 0.006.

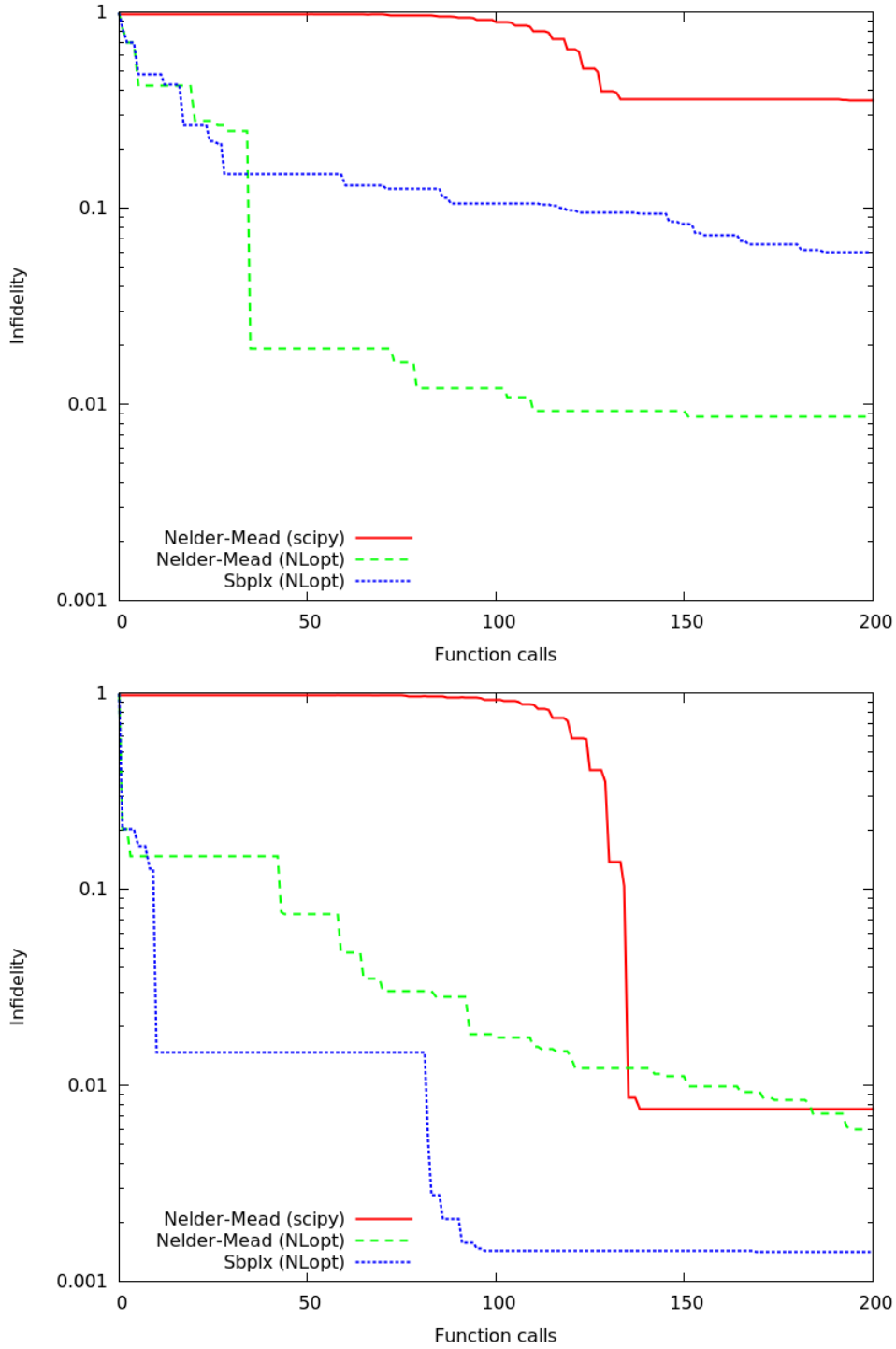

Figure 5.21: Same as figure 5.20, but with the randomized frequency sets `harm-rn3` (top) and `eig-rn1` (bottom). The respective lowest infidelities were 0.009 and 0.0014.

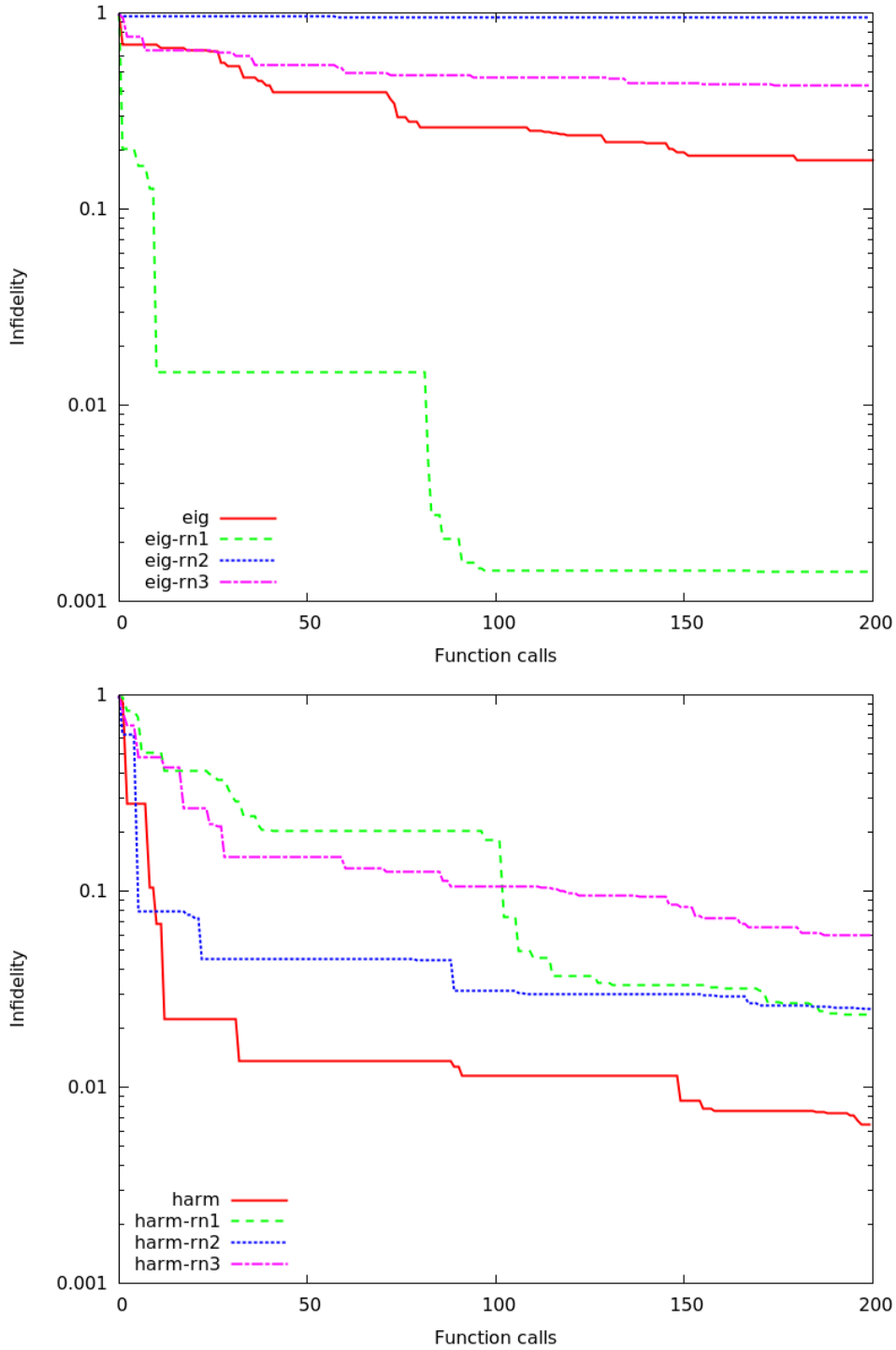

Figure 5.22: Comparison of different frequency basis sets. All calculations executed with Subplex. Top: The `eig` family with the resonant frequency set and its randomizations. Bottom: The harmonic frequency set `harm` and randomized copies. Except for `eig-rn1`, which yielded a large improvement over `eig`, the randomized frequencies performed not better than the exact ones. Contrasting the two diagrams also reveals that the optimization converges more reliably with harmonic frequencies.

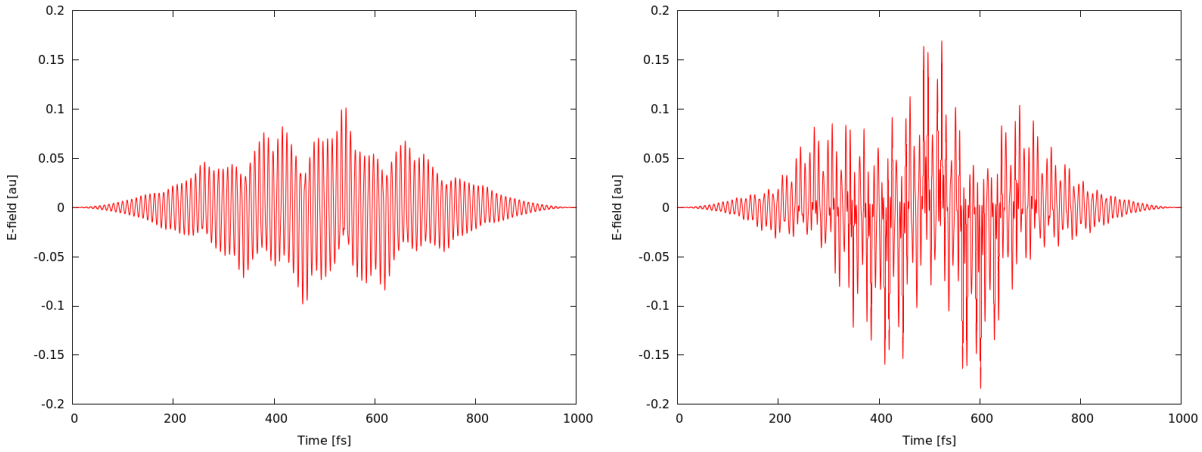

Figure 5.23: Two fields optimized with the `eig-rn1` basis by the NLopt NMS method (left) and Subplex (right).

Figure 5.24: Same as figure 5.23, but with the frequencies `harm`.

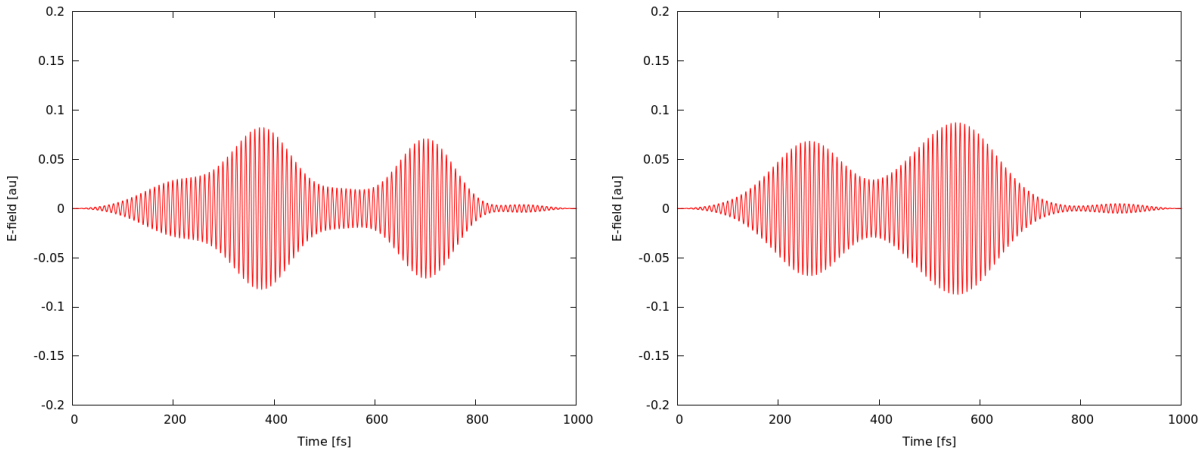

amplitudes below 0.1 au. This is due to the fact that the harmonic frequencies are smaller by one to two orders of magnitude, allowing only rather slow modulations of the pulse. Some typical examples are depicted in figure 5.23 and 5.24.

5.3.3 Frequency optimization

The optimization with variable frequencies yielded excellent results. Although the search space was smaller than in section 5.3.2 (nine- instead of ten-dimensional), the final infidelities were 0.0062 for Subplex and 0.0014 for NMS, well below those of most fixed frequency runs.

The infidelities are depicted in figure 5.25. The Subplex method showed its efficiency by converging much faster within the first iterations, but did not improve much after that. Apparently it ignored some important subspaces which were slowly, but steadily explored by NMS. This picture might change for other initial values or a different optimization target.

The final frequencies found by NMS were $\vec{\omega} = (0.90 \cdot 10^{-4}, 2.84 \cdot 10^{-4}, 4.52 \cdot 10^{-4})$, considerably different from the initial values of $(1.52 \cdot 10^{-4}, 3.04 \cdot 10^{-4}, 4.56 \cdot 10^{-4})$. Still, the final pulse (figure 5.26) bears a lot of similarity with the results of ten-parameter optimization with the `harm` basis, as it is relatively smooth and has a moderate amplitude.

This result highlights the importance of the frequencies used for optimization. Unless one is sure to have an ideal basis set, it is generally advisable to also optimize the frequencies for best performance. This goes against the spirit of CRAB, where a randomized, but fixed basis is used. However, randomized frequencies might still be a good initial guess for optimization.

5.3.4 LiCs diatomic

This system turned out to be very difficult to control. No way was found to populate exclusively $|1\rangle$ without simultaneously exciting other states.

Frequency optimization led to target populations of 42.5% with NMS and 43.8% with Subplex. CRAB, using the randomized harmonic basis, achieved comparable populations of 46.4% and 43.2%, respectively. In this case, the randomized basis performed better than the optimized one, if just slightly. Figure 5.27 shows the convergence behaviour, and the best field found by CRAB is shown in figure 5.28.

The reason for these disappointing results lies in the energy structure of LiCs. At low energies, the system has negligible anharmonicity and almost equidistant eigenvalues. This can also be seen in table 5.3, which lists the first 20 eigenenergies of LiCs found by diagonalization with MCTDH. As a result, small perturbations excite the system into an near-coherent state, which always has significant contributions from more than one eigenstate. Although more iterations of CRAB might have improved the target population a little, it cannot possibly get close to 100%.

As a remedy, one might suggest excitation into higher states such as $|10\rangle$ or even $|20\rangle$. Unfortunately, such calculations are impossible to perform accurately with the used primitive grid. Its lower border was as large as $x = 5.0$ – a point where the potential almost crosses zero. A

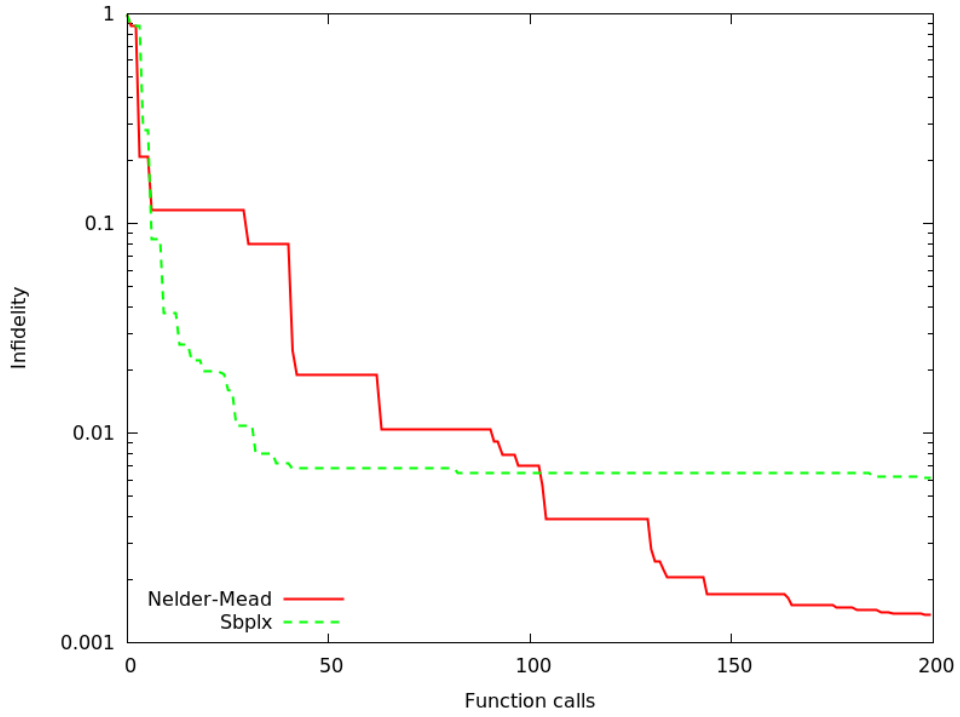

Figure 5.25: Optimization with variable frequencies. Infidelity $1 - p_5$ over the number of MCTDH runs.

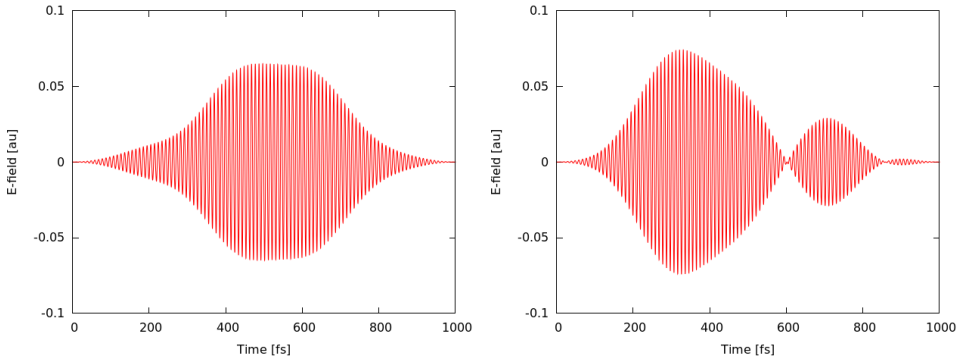

Figure 5.26: Fields optimized with a variable frequency basis, using NMS (left) and Subplex (right).

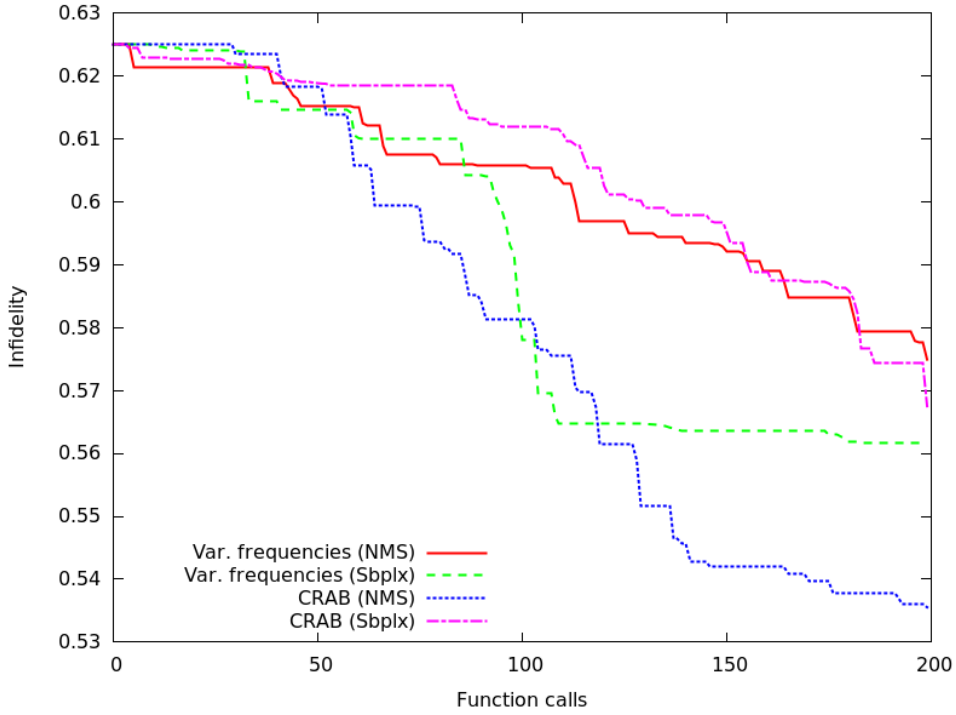

Figure 5.27: Optimization of the $|0\rangle$ to $|1\rangle$ transition in LiCs. CRAB with randomized harmonic frequencies was compared to the variable frequencies scheme described in section 4.3.3. CRAB with the NMS algorithm showed the best result with a final population of 46.4%. Note that the ordinate axis is *not* logarithmic.

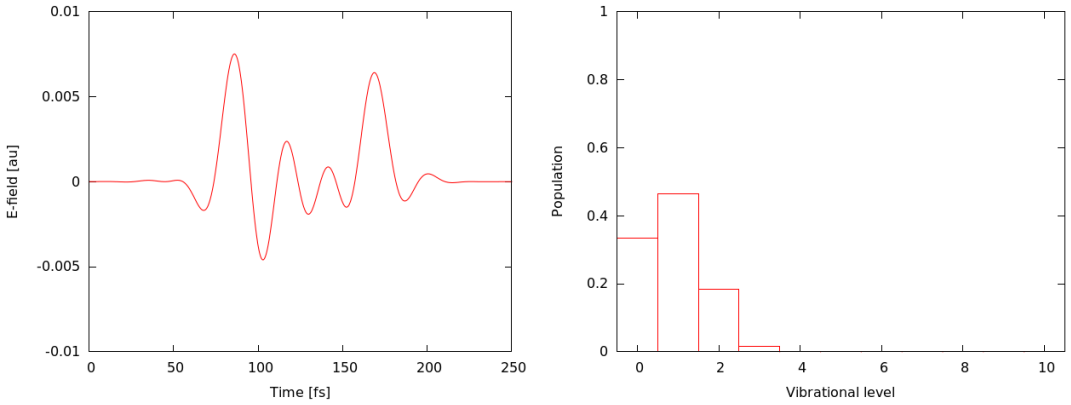

Figure 5.28: Optimized field for excitation of LiCs, found with CRAB and the NMS method. The pulse is depicted on the left, the final population on the right.

Table 5.3: Lowest eigenvalues of the LiCs molecule, determined with the diagonalization tool of MCTDH. Note that the molecule has at least 55 bound states, but the calculation of higher eigenenergies is rather inaccurate. After some experimentation with different DVRs and integrator settings, the error in E_{19} is presumed to be at most 1 meV and considerably smaller for the lower states.

n	E_n [meV]	n	E_n [meV]
0	-717	10	-502
1	-694	11	-482
2	-672	12	-462
3	-650	13	-443
4	-628	14	-423
5	-606	15	-404
6	-585	16	-386
7	-564	17	-368
8	-543	18	-348
9	-522	19	-332

larger grid would be very desirable, but no data for the electric dipole moment were available for $x < 5.0$. No sensible method for extrapolation was evident, therefore all attempts to selectively excite higher states were abandoned.

Given more time, a more detailed study of this system might have been rewarding. More effort should be placed on finding the optimal DVR in order to make the higher vibrational states accessible.

5.3.5 Krotov scheme

For the Morse oscillator, the field found by the Krotov algorithm in `optnctrl` (figure 5.29) was as irregular as the ones produced with the `eig` basis set. It yielded an infidelity of 0.009 after ten iterations, which took a total computation time of 25 minutes. This result could be improved to 0.005 by performing another five iterations, and further optimization with even longer calculations is probably possible. However, this approach was not followed due to this method's time consumption.

In the case of LiCs, the algorithm failed to converge altogether. Instead it broke off after eight iterations with increasingly un-physical (i.e. extremely large and discontinuous) fields. Although a better result might have been achieved with carefully chosen settings, this underlines the difficulty inherent to optimal control with LiCs.

5.4 Memory and CPU consumption

After all physical results have been presented, some final remarks concerning the computational effort should be made. Most calculations were performed on servers of the DESY PAL cluster,

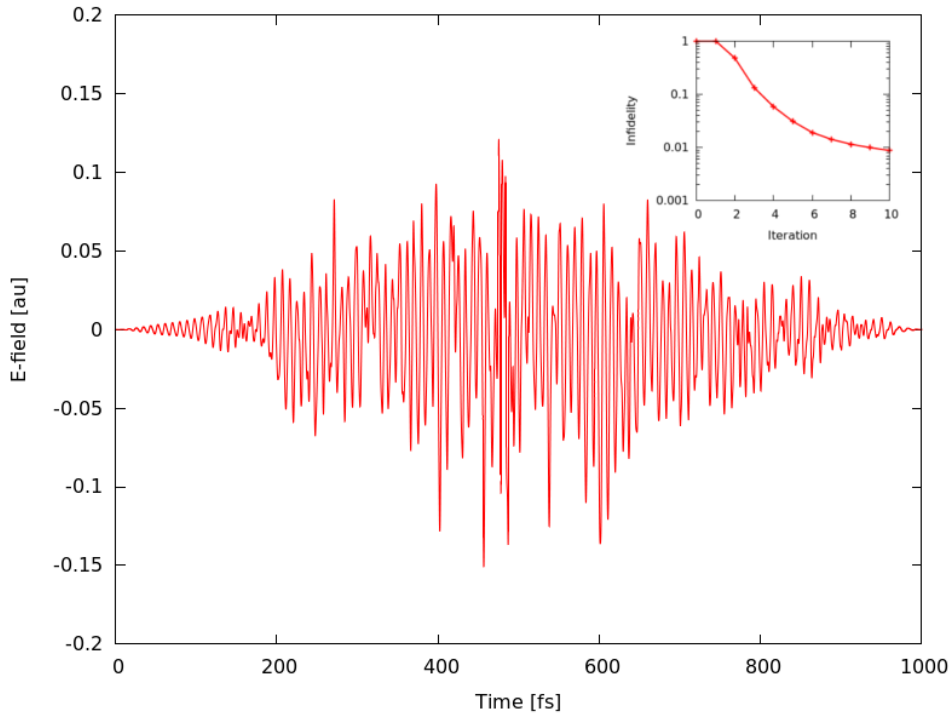

Figure 5.29: Krotov algorithm applied to the Morse oscillator. The large diagram shows the optimized field after ten iterations. Inset: The infidelity reached a value of 0.009.

most of which run at 3 GHz. Although MCTDH supports parallelization, only one processor core was used at a time.

When using the HO DVR, the propagation of the Morse system in section 4.2.3 took about ten minutes of CPU time and one MB of memory. With the sine DVR, memory consumption stayed roughly equal, but only about one minute of CPU time was required. This highlights how important the choice of the DVR is for the accuracy as well as the efficiency of a simulation. It should be mentioned that MCTDH still allocates much more memory at initiation. This amounted to about 250 MB in the cases considered here, but can become a serious issue when handling multi-dimensional systems. For example, the sample input file for benzene (modelled in ten dimensions) results in a memory allocation of more than 2 GB, which is already to much for a default job on DESY's BIRD cluster.

The more important question is how CRAB fares in comparison to the Krotov scheme. The latter usually gives excellent results even with a low number of iterations because it calculates the field $E(t)$ while propagating the wavefunction, using the value of $\Psi(t)$ for all times. In contrast, CRAB only considers the final target state population and discards all wavefunction information for intermediate times. In combination with the finite-dimensional search space, optimization is usually not quite as good as with the Krotov method. However, CRAB requires only very little resources, with virtually all computational effort lying in the repeated MCTDH calls. With a good DVR and for low excited states (as was the case with the Morse oscillator in this thesis), such a propagation can be faster than five seconds.

An optimization run with CRAB (with a fixed basis or with frequency optimization) usually took ten to fifteen minutes (wall time) for a limit of 200 function calls. MCTDH again occupied about one MB of memory. The disk space occupied by the output files depends on the parameter `tout` telling MCTDH how often to update the output files. Since CRAB only cares about the final state, the output files can be kept very small and less than 10 MB of storage are occupied for an optimization run. Most of this is due to the electric field, which is stored as plain text data. There is no significant difference between the ten-parameter control with fixed basis functions and the nine-parameter control which optimized the frequencies. The self-designed method for finding occupation numbers (see section 4.2.3) can be a bottleneck, as it converts part of the `psi` file into plain text. In the examples presented here, this file was usually smaller than 1 MB, but it can quickly become prohibitively large for higher dimensions or small values of `tout`. This fault cannot be attributed to CRAB, but to the deliberate creation of a quick-and-dirty tool. For future applications, a more efficient application for finding the target state occupation can (and will) be written.

Since the Krotov scheme uses information about $\Psi(t)$, the wavefunction must be written to the output in very small time steps, typically `tout` is 0.01 fs or less. Since `optcntrl` also requires the wavefunction to be calculated in double precision, very large `psi` files are generated. The optimization of the Morse pulse filled over 700 MB in about half an hour. The LiCs optimization had a shorter control time, so only 130 MB were written. The calculation time was comparable, probably due to the numerical difficulty of the LiCs system. Although `optcntrl` is slower and writes large files, its memory requirements are modest. Little more than 1 MB was used.

In summary, CRAB had a small advantage over the Krotov scheme in terms of speed (at least for the systems considered here) and was massively more efficient when it came to using disk space (which is very likely generally true).

6 Conclusion

This thesis has tested the applicability of the multi-configurational time-dependent Hartree method (MCTDH) to state selective control in diatomics, in particular in combination with the chopped random basis (CRAB) optimization scheme.

The motivation behind this work was to probe different tools for optimal control of molecular systems. Powerful computational methods for the theoretical treatment of molecules can assist the experimental path to laser selective chemistry.

MCTDH is a versatile scheme for propagating multi-dimensional wavepackets while including all important correlation effects [3]. The implementation used in this thesis was version 8.4.9 of the Heidelberg MCTDH package [25]. As all systems treated in this thesis are one-dimensional, the MCTDH algorithm was not actually applied. Instead, the MCTDH package was used to simply solve the one-dimensional Schrödinger equation. The decision to use this software was based on future applications to molecules with many degrees of freedom.

The MCTDH software was tested with a harmonic oscillator, which has the advantage of being analytically solvable. The wavefunction was propagated from different initial states, relaxed to find the ground state, and excited into a coherent state. In all these cases, MCTDH reproduced the expected results reliably.

The second step was selective excitation of a Morse oscillator which had been studied in the literature before [15]. Starting from the ground state, the vibrational state $|15\rangle$ was excited with train of monochromatic light pulses. Two slightly different pathways were used to reach the final state, which was finally achieved in agreement with the literature. However, the desired accuracy was only reached after changing the discrete variable representation (DVR) from a harmonic oscillator basis to sine basis functions and after including a complex absorbing potential (CAP). A sine DVR turned out to be more apt for representing high vibrational states, and the CAP prevents errors arising from the wavefunction hitting the edge of the grid.

Next, optimal control was attempted with CRAB. CRAB is a general purpose optimization algorithm which has been applied to various examples of quantum control. The electric field applied to the molecule is expanded in a truncated Fourier basis with randomized frequencies, converting the optimal control problem into a minimization of a multi-variate function.

An implementation of CRAB was written in Python, along with a script for state population analysis. The MCTDH package was used to propagate the system under the influence of the field. The analysis script returned the target state population to the CRAB program, which then computed the field parameters for the next iteration.

The systems under examination were the Morse oscillator above and the LiCs diatomic, which has a comparable potential energy function [24].

The algorithm was modified to use different frequency basis sets, including the resonant frequencies and the harmonic frequencies arising from the control time. These frequencies were used both with their exact values as well as after multiplication with a random factor. In another optimization run, the program was modified to also optimize the frequencies rather than keeping them fixed.

Since CRAB makes no statement about the minimization algorithm to use, three different external tools were tested. These are two implementations of the Nelder-Mead simplex (NMS) method from the `scipy.optimize` and the NLopt libraries [14, 13]. The latter library also contains the Subplex algorithm, a refinement of NMS. The success of any combination was measured in terms target state occupation.

Target populations higher than 99% could be achieved for the Morse oscillator with $|5\rangle$ a target state. It turned out that harmonic frequencies performed better and more reliably than the resonant frequencies in almost all cases. Randomization did not significantly improve the result for the Morse oscillator, although the randomized harmonic frequencies did not perform much worse, either. The best results were found with optimized frequencies, however no randomization took place here.

An surprising discrepancy was found between the two NMS variations, as the `scipy` implementation performed much worse than the NLopt version. The latter routinely gave good results, roughly on par with Subplex. Apparently the choice of the minimization algorithm is just as crucial for convergence as the correct frequency basis. On average Subplex did not perform much better than NMS, although is might prove superior in a higher-dimensional search space.

LiCs proved very difficult to control, as even the transition from ground to first excited state is not possible without populating higher states. This is due to the nearly equidistant spacing of the lowest eigenenergies. The calculations were further hindered by the fact that the dipole moment is not known for small inter-nuclear distances, so the grid had to be chosen a bit too short for accurate propagations. These difficulties limited the arget population to just over about 40% with the tested algorithms. CRAB, using randomized harmonic frequencies, showed a slight advantage over the frequency optimization method.

The very popular and well-probed Krotov method for optimal control was used for reference. The MCTDH package contains an implementation of this scheme, which can be considered state of the art for optimal control. For the Morse oscillator, it showed a performance comparable to the best basis-algorithm combinations with just a slightly (about 50%) larger time consumption. However, the resulting pulse showed a rather irregular shape with high field gradients, which might be undesirable for experimental reproductions. From this aspect, some fields optimized with CRAB were smoother and possibly easer to implement in practice. The Krotov method diverged when trying to optimize the LiCs pulse, which is attributed to the unpleasant properties of the system, not to the algorithm.

When contrasting CRAB with the Krotov scheme, the former fared surprisingly well despite its apparent simplicity. As few as nine to ten optimization parameters were enough to find a pulse which was at least as good as the result of the more sophisticated Krotov method. At the same time, CRAB was faster and required hardly any disk space while the Krotov scheme filled hundreds of megabytes. For the problems considered in this thesis, CRAB is by no means inferior to the Krotov scheme. For best results, it is usually advisable not to randomize the frequency basis, but to let the algorithm search for the optimal frequencies.

Further research should follow various directions. Firstly, the restriction to one dimension is a serious limitation for experimental applications. If one aims to implement optimal control in the laboratory, the extension to higher-dimensional systems will be necessary. This also applies to considering other potential energy surfaces, which are effectively treated as additional degrees of freedom by MCTDH. The algorithm has even been applied to conical intersections, so there is a vast field of realistic molecular dynamics at grasp.

While MCTDH is – by design – very suitable for treating high-dimensional systems, this is not yet entirely clear for CRAB. It has shown to work well in this case, but it still has to show whether the simple truncated-basis approach leads to satisfactory fields for controlling more complex molecules. The results of this thesis encourage such an analysis.

Given the fact that different optimization algorithms – and even implementations of the same algorithm – can exhibit huge differences in performance, a more systematic study of such algorithms and their applicability to typical optimal control problems seems reasonable.

The numerical treatment of the LiCs system was apparently inadequate. If a an accurate description of this molecule is desired, a thorough search for the best DVR is recommended, as well as a workaround for the dipole function at low distances.

As Dr. Peter Schmelcher pointed out, a molecule at finite temperature is not in its pure ground state, but rather in an incoherent superposition of eigenstates given by the Boltzmann distribution. For real life applications it is important to not just control pure states, but also to excite systems starting from such mixed states. For this purpose the wavefunction formalism is no longer applicable, but instead a density operator $\rho = \sum p_i |\Psi_i\rangle\langle\Psi_i|$ must be propagated. Implementing this was unfortunately beyond the scope of this thesis. Yet, such propagations have already been performed with the so-called ρMCTDH algorithm [**?**]. Hence, further studies in this direction seem rewarding, too.

Bibliography

[1] Ernest S. Abers. *Quantum Mechanics*. Addison-Wesley, 1 edition, 6 2003.

[2] Mireille Aymar and Olivier Dulieu. Calculation of accurate permanent dipole moments of the lowest $^{1,3}\Sigma^+$ states of heteronuclear alkali dimers using extended basis sets. *The Journal of chemical physics*, 122(20):204302, 2005.

[3] Michael H Beck, Andreas Jäckle, GA Worth, and H-D Meyer. The multiconfiguration time-dependent Hartree (MCTDH) method: A highly efficient algorithm for propagating wavepackets. *Physics reports*, 324(1):1–105, 2000.

[4] Constantin Brif, Raj Chakrabarti, and Herschel Rabitz. Control of quantum phenomena: past, present and future. *New Journal of Physics*, 12(7):075008, 2010.

[5] Tommaso Caneva, Tommaso Calarco, and Simone Montangero. Chopped random-basis quantum optimization. *Physical Review A*, 84(2):022326, 2011.

[6] Emanuel F de Lima and José E M Hornos. Matrix elements for the Morse potential under an external field. *Journal of Physics B: Atomic, Molecular and Optical Physics*, 38(7):815, 2005.

[7] Roger L. Dekock and Harry B. Gray. *Chemical Structure and Bonding*. University Science Books, 2 edition, 10 1989.

[8] Wolfgang Demtröder. *Molekülphysik: Theoretische Grundlagen und experimentelle Methoden*. Oldenbourg Wissenschaftsverlag, 9 2003.

[9] Thomas Dittrich, Peter Hänggi, Gert-Ludwig Ingold, Bernhard Kramer, Gerd Schön, and Wilhelm Zwerger. *Quantum transport and dissipation*, volume 3. Wiley-Vch Weinheim, 1998.

[10] RE Grisenti, W Schöllkopf, JP Toennies, GC Hegerfeldt, T Köhler, and M Stoll. Determination of the Bond Length and Binding Energy of the Helium Dimer by Diffraction from a Transmission Grating.

[11] Frank Grossmann. *Theoretical Femtosecond Physics: Atoms and Molecules in Strong Laser Fields*. Springer, 2nd edition, 2013.

[12] Frank Jensen. *Introduction to Computational Chemistry*. Wiley, 2007.

[13] Steven G. Johnson. The NLopt nonlinear-optimization package. http://ab-initio.mit.edu/nlopt. Accessed 2014-07-17.

[14] Eric Jones, Travis Oliphant, Pearu Peterson, et al. SciPy: Open source scientific tools for Python. http://www.scipy.org/. Accessed 2014-07-17.

[15] MV Korolkov, GK Paramonov, and B Schmidt. State-selective control for vibrational excitation and dissociation of diatomic molecules with shaped ultrashort infrared laser pulses. *The Journal of chemical physics*, 105(5):1862–1879, 1996.

[16] Ronnie Kosloff, Stuart A Rice, Pier Gaspard, Sam Tersigni, and DJ Tannor. Wavepacket dancing: Achieving chemical selectivity by shaping light pulses. *Chemical Physics*, 139(1):201–220, 1989.

[17] Vadim Krotov. *Global Methods in Optimal Control Theory*, volume 195. CRC Press, 1995.

[18] Ira N. Levine. *Molecular Spectroscopy*. Wiley, 4 1975.

[19] H-D Meyer, Uwe Manthe, and Lorenz S Cederbaum. The multi-configurational time-dependent hartree approach. *Chemical Physics Letters*, 165(1):73–78, 1990.

[20] Hans-Dieter Meyer. Introduction to MCTDH. *Lecture Notes*, 2011.

[21] Hans-Dieter Meyer and Graham A Worth. Quantum molecular dynamics: Propagating wavepackets and density operators using the multiconfiguration time-dependent hartree method. *Theoretical Chemistry Accounts*, 109(5):251–267, 2003.

[22] John A Nelder and Roger Mead. A simplex method for function minimization. *The computer journal*, 7(4):308–313, 1965.

[23] Thomas Harvey Rowan. *Functional Stability Analysis of Numerical Algorithms*. PhD thesis, 1990.

[24] Markus Schröder, Jose-Luis Carreon-Macedo, and Alex Brown. Implementation of an iterative algorithm for optimal control of molecular dynamics into MCTDH. *Phys. Chem. Chem. Phys.*, 10:850–856, 2008.

[25] Peter Staanum, Asen Pashov, Horst Knöckel, and Eberhard Tiemann. *Phys. Rev. A*, 75:042513, Apr 2007.

[26] G. A. Worth, M. H. Beck, A. Jäckle, and H.-D. Meyer. The MCTDH Package, Version 8.2, (2000). H.-D. Meyer, Version 8.3 (2002), Version 8.4 (2007). See http://mctdh.uni-hd.de.

[27] Graham A Worth and Lorenz S Cederbaum. Beyond Born-Oppenheimer: Molecular dynamics through a conical intersection. *Annu. Rev. Phys. Chem.*, 55:127–158, 2004.

Acknowledgements

I would never have written this thesis without many kind and helpful people whose efforts I want to acknowledge here.

First, I would like to thank my advisor Prof. Dr. R.J. Dwayne Miller (MPSD) for giving me the opportunity to work in his group and for offering me the possibilities to pursue my academic career. Next, I am very thankful to my co-advisor Prof. Dr. Peter Schmelcher (ILP) for a lot of support and helpful input over the past months. He suggested to use CRAB, supplied the LiCs data and organized the contact with other researchers who would help me in my work.

Thanks to Prof. Dr. Hans-Dieter Meyer from Heidelberg for supplying the MCTDH software. I thank his post-doc Dr. Markus Schröder, who developed the `optcntrl` component of MCTDH and helped me when I couldn't make it run. Thanks to Dr. Antonio Negretti (ILP), who gave me valuable advice on implementing CRAB. Thanks to Dr. Taisuke Hasegawa and Dr. Arend Dijkstra from the Miller group for looking after me and being generally helpful.

I thank my office mates Ara, Haider and Steffi for being a good company and creating an awesome and motivating environment to work in.

On a personal note, I have to thank my family, especially my parents for their amazing and ongoing support in all aspects. I can't possibly thank my girlfriend Sylvia enough, who supported and motivated me and generally took great care of me, in particular during the final weeks of this thesis. Thanks to all my dear friends, who made my life enjoyable over the past few years.

To all of you, I thank you very much.

Eigenständigkeitserklärung

Hiermit bestätige ich, dass die vorliegende Arbeit von mir selbständig verfasst wurde und ich keine anderen als die angegebenen Hilfsmittel – insbesondere keine im Quellenverzeichnis nicht benannten Internetquellen – benutzt habe und die Arbeit von mir vorher nicht einem anderen Prüfungsverfahren eingereicht wurde. Die eingereichte schriftliche Fassung entspricht der auf dem elektronischen Speichermedium. Ich bin damit einverstanden, dass die Masterarbeit veröffentlicht wird.[1]

Hamburg, den 30. Juli 2014, Christian Ziemann

[1] English translation: I hereby declare that I have written this thesis by myself without using any undocumented aids, in particular no internet sources other than the ones listed in the bibliography. I have not handed in this thesis for any other examination process. This printed document is identical to the attached electronic version. I agree to publication of this thesis.